Catalytic Solid Oxide Membrane Reactors: Development and Application in the Oxidative Coupling of Methane

by

Valentina Omoze Igenegbai

A dissertation submitted in partial fulfillment
of the requirements for the degree of
Doctor of Philosophy
(Chemical Engineering)
in the University of Michigan
2020

Doctoral Committee:

Professor Suljo Linic, Chair
Professor Erdogan Gulari
Professor Melanie Sanford
Assistant Professor Nirala Singh

Valentina Omoze Igenegbai

voigeneg@umich.edu

ORCID iD: 0000-0002-2677-005X

Dedication

This dissertation is dedicated to my family for their endless love and support.

Acknowledgements

I would like to take this opportunity to acknowledge all those who contributed to the successful completion of my PhD journey. First and foremost, I would like to thank my PhD advisor, Prof. Suljo Linic, for accepting me into his research group and for providing the resources to complete this dissertation work. I am very grateful to him for all the valuable feedback he offered during this work and for providing recommendations in support of my various applications. Thanks to his mentorship, I have grown significantly as a researcher and as an individual. I would also like to thank Prof. Erdogan Gulari, Prof. Melanie Sanford and Prof. Nirala Singh for taking time out of their busy schedules to serve on my dissertation committee and for their useful feedback on my written and oral exams.

I have had the pleasure of interacting with these brilliant past and present members of the Linic lab: Brittany Farrell, Paul Hernley, Tim Van Cleve, Matthew Morabito, Calvin Boerigter, Robert Campana, Umar Aslam, Vishal Govind Rao, Joe Quinn, Saman Moniri, Steven Chavez, Sean Dix, John Hemmerling, Rawan Almallahi, Rachel Elias, Jacques Esterhuizen, Ali Motagamwala, James Wortman, Shawn Lu and Aarti Mathur. I thank you all for your friendship, help around the lab, and useful feedback on my research and presentations. Special thanks to Brittany Farrell for helping me get started in the lab. Thanks to Umar Aslam for livening up the lab and bringing humor even in the most uncomfortable situations. Thanks to Rawan Almallahi, Ali Motagamwala and James Wortman, who I worked closely with in the final years of my PhD. I appreciate our intellectual conversations and your assistance with reviewing my writings. It was a great pleasure sharing an office with Rawan the past two years. I enjoyed all our conversations

about science and non-science topics. Thanks, Joe Quinn, for the helpful conversations on navigating the PhD program. Thanks, John Hemmerling, for helping with the glove box and for being part of the ChE symposium committee. Thanks to Rachel Elias and Steven Chavez for organizing several awesome lab outings and to Sean Dix for hosting delightful group dinners. I wish the very best for every one of you.

I would like to acknowledge and express gratitude to the Federal Government of Nigeria for supporting part of my PhD studies through the Presidential Special Scholarship Scheme for Innovation and Development. I thank the Rackham Graduate School at the University of Michigan for supporting part of my studies with the Rackham Predoctoral Fellowship Award. I would also like to acknowledge and thank ExxonMobil Research and Engineering for funding and collaboration on this dissertation work.

I would like to thank my awesome Ann Arbor friends, outside of my lab, who supported me through this PhD journey. Special thanks to Hanieh Safari, Naomi Ramesar, and Maria Ma for being great friends and study partners particularly in the early years of my PhD. There are many other people I would like to acknowledge individually but I am afraid the list would be too long. I am excited for what the future holds for us and look forward to many more years of friendship.

I would like to express my utmost gratitude to my family for believing in me and supporting me during this PhD process. I thank my siblings for the regular phone calls, messages and group chats that made me feel close to home even when miles away. I thank my parents for all the sacrifices they have made for me and for being my greatest source of inspiration and support. Words alone cannot express how grateful I am to them.

Table of Contents

List of Figures

List of Tables

Abstract

Developing direct routes for upgrading methane (the principal component of natural gas) into value-added chemicals is crucial for integrating natural gas into the chemical industry in a more environmentally sustainable way. Unlike commercial multi-step methane conversion routes that rely on economies of scale, the direct routes can be potentially applied in upgrading natural gas from small-scale sources, thereby mitigating their underutilization and flaring to deleterious greenhouse gases. The oxidative coupling of methane (OCM) is a promising direct route for converting methane to valuable C_2 hydrocarbons (ethylene and ethane). This reaction occurs at high temperatures in the presence of oxygen and an active catalyst. The main challenge with OCM is the formation of undesired byproducts (CO and CO_2) from over-oxidation reactions, which limits the C_2 selectivity. This selectivity problem is particularly significant in conventional co-fed reactors (where oxygen is fed together with methane) because the high gas-phase oxygen concentrations at the reactor inlet accelerates the undesired over-oxidation reactions. In this dissertation, the thermodynamic and kinetic constraints on the C_2 selectivity and yield in OCM are elucidated. With the aid of reactor models, we demonstrated that an oxygen-ion (O^{2-}) conducting catalytic solid oxide membrane reactor, with distributed oxygen feed along the reactor length, can achieve significantly higher C_2 selectivity and yield compared to a conventional co-fed reactor. From systematic experimental studies, $BaCe_{0.8}Gd_{0.2}O_{3-\delta}$ (BCG) was identified as an O^{2-} conducting material that is catalytically active for OCM and shows high resistance to deactivation via solid carbon deposition. These properties make BCG a promising membrane-catalyst material for OCM membrane reactors. Further work included fabricating tubular BCG membranes via a

combined slip-casting and solid-state reactive sintering technique using Cu as a sintering additive. OCM results from the Cu-modified BCG tubular membrane reactors (with distributed oxygen feed) showed greater C_{2+} selectivity compared to co-fed reactor operation, at similar methane conversions. This conclusive experimental result supports the main hypothesis of this study; that catalytic solid oxide membrane reactors can improve OCM performance compared to conventional co-fed reactors.

Chapter 1

Introduction and Background

1.1 Summary

This chapter begins with a discussion on natural gas with a focus on the opportunities and challenges associated with the increase in supply of natural gas from shale sources. The various routes for converting the principal component of natural gas (methane) to valuable chemicals is discussed, highlighting the advantages of direct routes over traditional multi-step industrial routes for methane conversion. The discussion then focuses on the oxidative coupling of methane (OCM) as a promising route for direct methane conversion. The challenges with OCM are highlighted and the potential to overcome some of these challenges using solid oxide membrane reactors is discussed. Reactor models that illustrate improved OCM performance of a catalytic solid oxide membrane reactor over a conventional packed-bed reactor are presented and analyzed. This is followed by a discussion of the benefit of integrating selective OCM catalysts in solid oxide membrane reactors along with criteria that will enable optimum performance and long-term stability of the integrated membrane-catalyst systems. The chapter concludes with a statement on the scope of the dissertation and a brief summary of each chapter in the dissertation.

1.2 Opportunities and Challenges with Natural Gas

The US production of the natural gas (over 500 trillion ft^3 of proved reserves) has increased significantly since the year 2005 and is projected to continue to increase over the next two decades.[1,2] The increase in production is driven mainly by advances in the recovery of natural gas from shale gas and tight oil reserves by hydraulic fracturing as shown in Figure 1.1.[3] The boom in shale gas production has contributed to the decoupling of US crude oil and gas prices, with the price of natural gas becoming relatively lower than crude oil.[2,4] Given the abundance and relatively low cost of methane, it an attractive alternative to crude oil as a source of fuel and chemicals. More than 90% of natural gas is used as fuel for heating, cooking, power generation and transportation.[5] It is considered a cleaner fossil fuel compared to crude oil and coal as it has a lower carbon footprint and produces less amounts of nitrogen and sulfur oxide emissions.[2,6]

A significant portion of natural gas is underutilized because it is found in remote locations and is considered "stranded". This includes natural gas produced as a by-product during oil recovery (associated gas).[7] Transporting the stranded gas from remote locations to commercial upgrading facilities and eventually to market is not cost effective because it requires energy-intensive pressurization in pipelines or condensation to liquified natural gas (LNG).[2,8] Due to the unavailability of economically viable means of utilization, stranded gas is often flared or vented. This practice does not only result in the waste of a valuable feedstock, but also results in the emission of deleterious green-house gases (CO_2 and CH_4).[8] Gas flaring operations occur not just within the US, but also in oil rich countries in the Middle east, Asia and Africa.[5] The World Bank estimates that over 5 trillion ft^3 of natural gas is flared yearly worldwide, which is roughly one-fifth of the US total annual natural gas consumption. This flaring causes the release of more than 350 million tons of greenhouse gas CO_2 annually.[7] To overcome this global challenge, it is

imperative to develop methods for valorizing natural gas at remote locations. Since natural gas is composed primarily of methane (70 – 90% of the carbon),[5,9] the conversion of methane into more valuable chemicals is undeniably a crucial pathway for utilizing stranded gas.

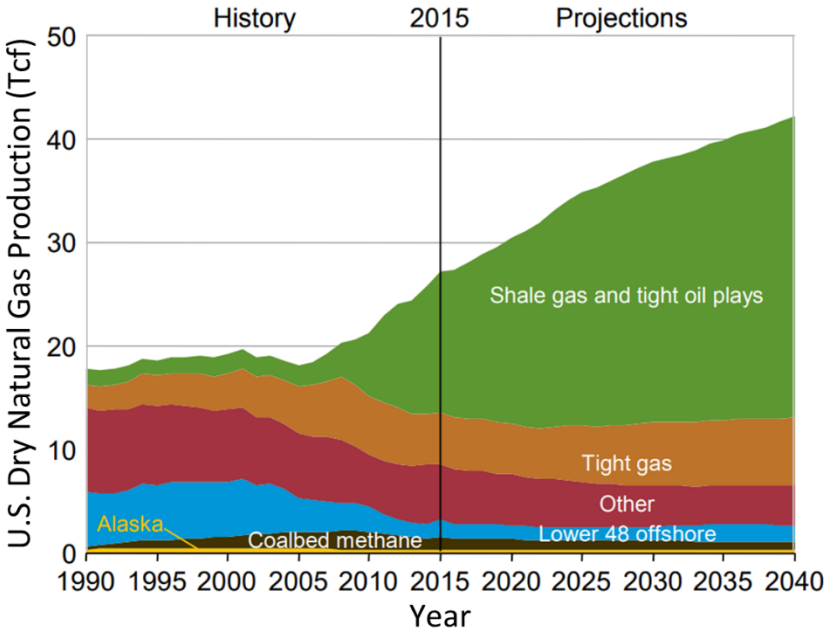

Figure 1.1. U.S. dry natural gas production by source from EIA Annual Energy Outlook 2016.[3]

1.3 Methane to Chemical Conversion

Methane is a symmetric molecule that is very difficult to activate under mild temperatures and pressures due to its strong and stable C-H bonds (bond strength ~ 434 kJ/mol) and low polarizability.[5,10] Industrially, the conversion of methane to valuable chemicals is achieved through indirect processes that involve an intermediate synthesis gas (a mixture of mainly CO and H_2) production step. Synthesis gas (or syngas) is used for methanol production and Fisher-Tropsch synthesis. The hydrogen in syngas is also used as a feedstock for ammonia production via the Haber-Bosch process.[5,11] However, syngas production (e.g., through steam reforming of methane)

is very expensive and carbon-intensive requiring high operating temperatures (700 – 1000°C) and pressures (15 – 40 atm).[9] The high capital investment required for syngas production means that it benefits from the economies of scale and is not profitable for use in upgrading methane from stranded small-scale sources. This issue contributes to the flaring of stranded natural gas and is a major motivation for the development of direct routes for methane conversion that would lend themselves to small scale operations.[11]

There are several direct routes under investigation for methane upgrading which include oxidative coupling of methane to higher hydrocarbons, non-oxidative coupling of methane to higher hydrocarbons including aromatics, and direct partial oxidation of methane to methanol and formaldehyde.[8,11] However, these direct processes are still in the research stage as their commercialization is hampered by low product selectivity and yield. The work in this dissertation is focused on the oxidative coupling of methane which is discussed further in the following section.

1.4 Oxidative Coupling of Methane (OCM)

Oxidative coupling of methane (OCM) is a process where methane is converted directly to C_2 hydrocarbons (ethylene and ethane) in the presence of an oxidant (typically oxygen). It is traditionally performed at high temperatures using heterogenous catalysts, although some low temperature homogenous activation of methane have been reported with relatively low yields.[12] Keller and Bhasin[13] published the first studies on OCM in the early 1980s, which has since then been followed up by many researchers. The ethylene product from OCM is particularly desired because it is one of the largest volume industrial precursors used in the production of polyethylene plastics and other valuable chemicals.[14] Ethylene is currently being produced through energy-intensive processes such as the steam cracking of ethane or naphtha.[15,16] Therefore, the possibility of converting methane into ethylene in a direct one-step process makes OCM highly desirable. The

proposed mechanism for OCM that is widely reported in the literature involves the abstraction of a hydrogen atom from methane by surface oxygen species to form methyl radicals (CH_3•).[17,18] The methyl radicals are released into the gas-phase where they dimerize to form ethane, which is subsequently dehydrogenated to ethylene in the gas phase or on the catalyst surface.[8,19,20]

Previous OCM studies have been mainly focused on testing different mixed metal oxide catalysts in flow reactors at atmospheric pressure and temperatures of 600 - 1000°C.[21] The goal of these studies was mainly to identify catalytic systems that maximize the yield of the C_2 products. Figure 1.2 is a plot of C_2 selectivity versus CH_4 conversion for a representative number of OCM catalysts tested in conventional packed bed reactors.[21,22] The data in the figure reveals that, in general, high methane conversion leads to lower C_2 selectivity and vice versa. Consequently, the C_2 yield which is calculated from the product of methane conversion and C_2 selectivity is always limited. The dashed line on the left and right side of the figure represents C_2 yield of 20 and 30%, respectively. The blue shaded region represents the widely cited commercial viability targets of a minimum single-pass C_2 yield of $\sim$ 30% at a C_2 selectivity $\geq$ 90%, using undiluted feed streams.[23,24] It can be observed that the reported single-pass C_2 yield and selectivity from various catalysts have remained below this target.

The conversion-selectivity interplay shown in Figure 1.2 is typically associated with reactions where the desired product is an intermediate that can be sequentially converted at relatively high rates to more thermodynamically favored products. To promote the selectivity of an intermediate in a series reaction, it is desired to employ reactor designs that allow low mixing of chemical species, which can be achieved using a plug flow reactor design.[25] Accordingly, most of the studies in OCM have been performed using plug flow reactor designs such as packed bed reactors (PBRs) illustrated in Figure 1.3.[21]

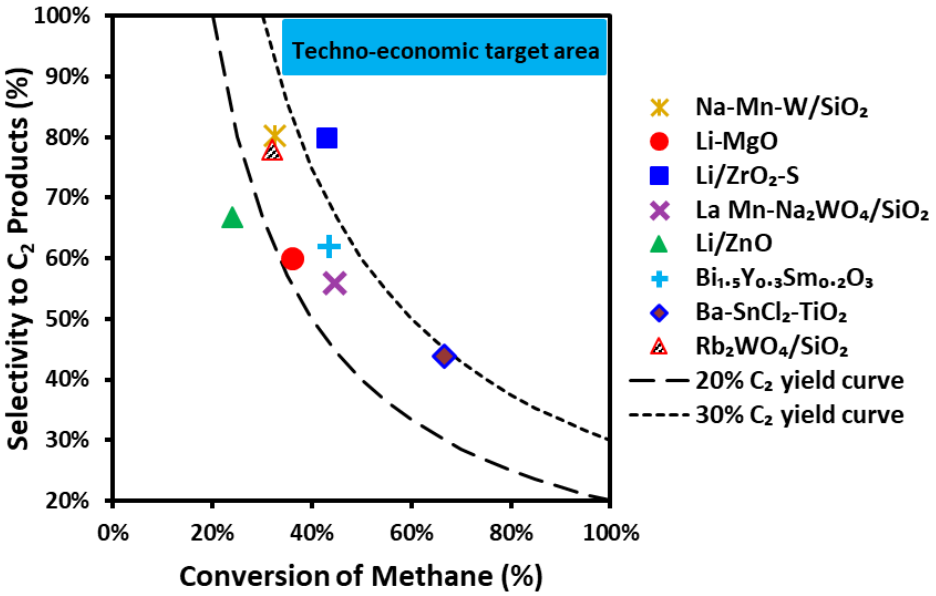

Figure 1.2. Plot of C_2 selectivity versus CH_4 conversion for a representative number of mixed oxide catalysts in packed bed reactors.[26–33]

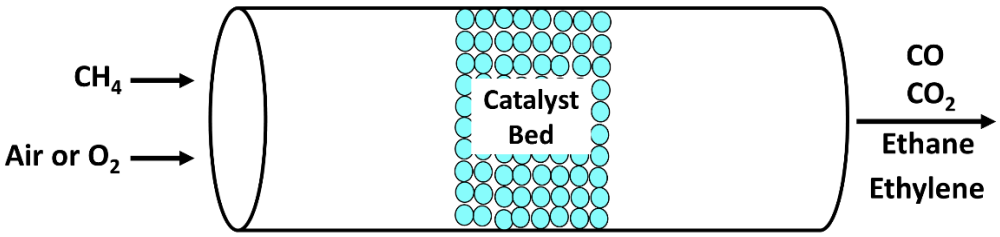

Figure 1.3. Schematic representation of a packed bed reactor operation in OCM

1.5 Challenges with OCM

A fundamental reason for the low C_2 yield observed in previous OCM studies is the process thermodynamics.[22] Data in Figure 1.4a shows the change in Gibbs free energy for various reactions that can occur between methane and oxygen at 1073K and 1atm. It can be observed that the thermodynamics favor not only the formation of C_2 products, but also the formation of solid carbon (C_s) and to a greater extent, the formation of CO_x (CO and CO_2). The data in Figure 1.4b shows the dependence of the thermodynamic equilibrium carbon product selectivity on the O_2/CH_4 feed ratio at 1073K and 1atm calculated by minimizing the Gibbs free energy of the system. High O_2/CH_4 ratios favor the formation of CO_x while low O_2/CH_4 ratios (closer to the stoichiometric ratio for C_2 formation) favor the formation of carbon deposits, which has been modelled as graphite. Under no condition is the formation of C_2 products favored at thermodynamic equilibrium.

To determine other reaction conditions that may favor the formation of C_2 products, it is important to understand the process kinetics. These kinetic studies are vital to identify the key reaction steps that occur in OCM, to develop rate expressions that can be used to quantify reaction rates and for use in simulating the performance of catalytic flow reactors. However, in comparison to screening of various catalysts for OCM, there are much fewer detailed kinetic studies that have been reported.[20,34,35] Reasons for the limited number of rigorous kinetic studies include (1) the occurrence of rapid, free radical, gas phase reactions which promotes the deep oxidation pathways irrespective of the type of catalyst, (2) the difficulty in preventing large increases in local catalyst temperature (hot spots) due to the occurrence of highly exothermic deep oxidation reactions, and (3) thermally and chemically induced phase changes of the catalysts during the reaction as well as the formation of carbon deposits.[22,36] Recent studies on the gas-phase reaction network in OCM

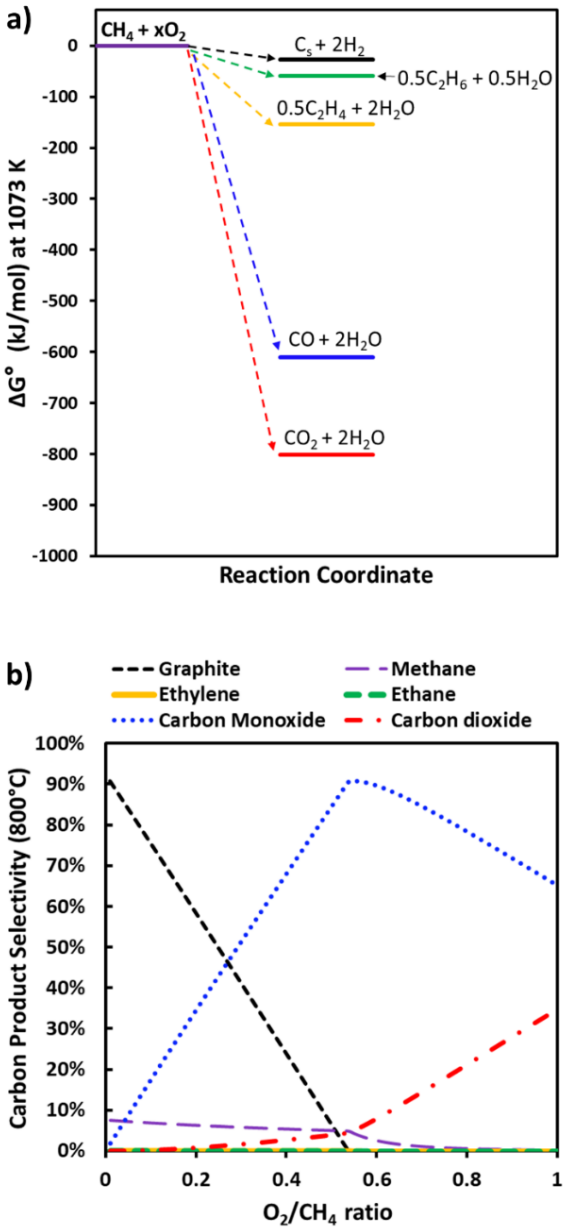

Figure 1.4. (a) Change in Gibbs free energy for various reactions that can occur from methane and oxygen at 1073K and 1atm. (b) Plot of thermodynamic carbon product selectivity (obtained by minimizing Gibbs free energy) as a function of the O_2/CH_4 feed ratio for a reactor at 1073K and 1atm.

reveal that the deep-oxidation reactions that occur in the gas-phase are mainly initiated by the reaction of gas-phase O_2 with hydrocarbon radicals as shown in the OCM reaction network in Figure 1.5.[37] As mentioned above, these unselective gas-phase reactions occur regardless of the nature of the catalyst and contribute significantly to the low selectivity observed in OCM.

Despite the challenges discussed above**,** Stansch et al[20] performed a detailed kinetic study of OCM on a La_2O_3/CaO catalyst. From their experimental data, they proposed a simplified 10-step reaction network shown in Figure 1.6 which consists of parallel and sequential reactions of methane to C_2 and CO_x products as well as water-gas shift reactions. The authors also proposed various rate expressions for the different reaction steps in the network and estimated the kinetic parameters (e.g. apparent frequency factors and activation barriers) from their experimental data. This kinetic model has been found to adequately predict the experimental data from La_2O_3/CaO[20] and other oxide catalysts.[38,39] The rate expressions proposed in the kinetic model by Stansch et al[20] show that the reactions that lead to the formation of CO_x products have an $\sim 1^{st}$ order dependence on O_2 partial pressure, while those leading to C_2 formation have an $\sim$ ½ order dependence. A similar dependence of reaction rates on O_2 partial pressure has been reported by Tiermersma et al[40] on a $Mn/Na_2WO_4/SiO_2$ catalyst, one of the best performing OCM catalyst reported in literature.[41] This kinetic behavior also indicates that operating at high partial pressures of gas-phase O_2 limits the C_2 product selectivity.

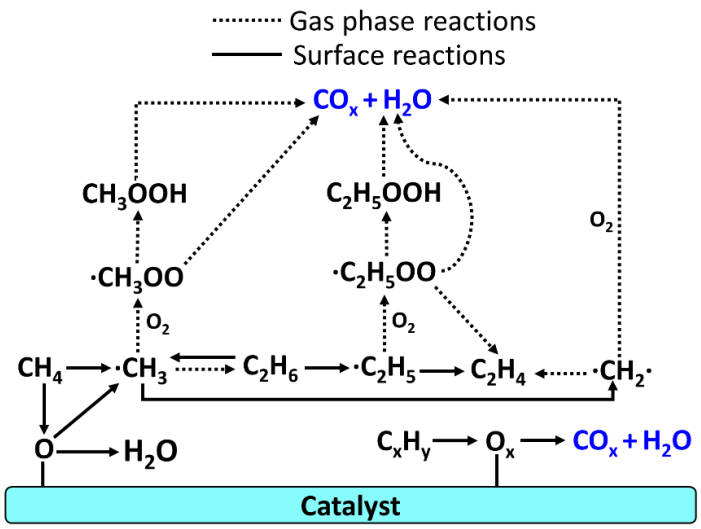

Figure 1.5. A detailed OCM reaction network on an oxide catalyst

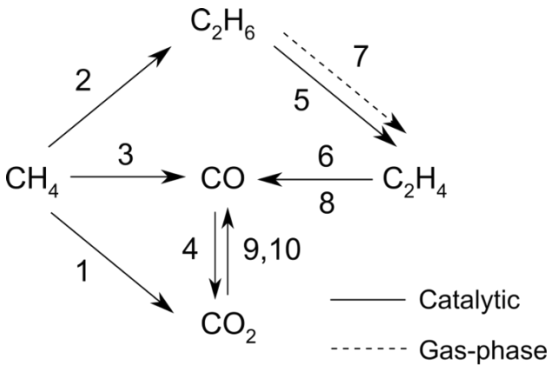

Reaction 1: $CH_4 + 2O_2 \rightarrow CO_2 + 2H_2O$
Reaction 2: $2CH_4 + 0.5O_2 \rightarrow C_2H_6 + H_2O$
Reaction 3: $CH_4 + O_2 \rightarrow CO + H_2O + H_2$
Reaction 4: $CO + 0.5O_2 \rightarrow CO_2$
Reaction 5: $C_2H_6 + 0.5O_2 \rightarrow C_2H_4 + H_2O$
Reaction 6: $C_2H_4 + 2O_2 \rightarrow 2CO + 2H_2O$
Reaction 7: $C_2H_6 \rightarrow C_2H_4 + H_2$
Reaction 8: $C_2H_4 + 2H_2O \rightarrow 2CO + 4H_2$
Reaction 9: $CO + H_2O \rightarrow CO_2 + H_2$
Reaction 10: $CO_2 + H_2 \rightarrow CO + H_2O$

Figure 1.6. Simplified 10-step OCM reaction network used in kinetic study on a La_2O_3/CaO catalyst. Figure was reproduced from Stansch et al.[20]

1.6 Solid Oxide Membrane Reactors

In conventional PBRs where methane and oxygen are fed together at one end of the reactor, high oxygen partial pressures are required at the inlet to achieve high methane conversions, which in turn leads to lower selectivity as discussed above. In other words, operating these systems at low oxygen partial pressures can improve selectivity but at the expense of methane conversion. Alternative reactor designs which allow the distribution of oxygen across the length of a flow reactor can be used to achieve low local oxygen partial pressures. One such design is a membrane reactor in which methane and an oxygen-containing stream is separated by a membrane that allows the permeation of oxygen to the methane side but prevents the opposite transfer of methane.[42] In OCM, dense (non-porous) membranes made from solid oxide materials are commonly used due to their relatively high stability at elevated temperatures and their ability to transfer O^{2-} ions (referred to as ionic conductivity). These membranes give the added benefit of providing the reaction with pure oxygen from air eliminating the need for expensive separation due to their ability to screen out other air components.[42]

Figure 1.7 illustrates the operation of a dense solid oxide membrane plug flow reactor. As shown in the figure, an optimal membrane reactor design will include an integrated OCM catalyst. The oxygen transfer across the membrane is driven by the difference in the oxygen partial pressure between the methane side and the oxygen side. To fulfill overall charge neutrality in the membrane, there is a need for countercurrent flow of electrons. This can be achieved by using a mixed ionic and electronic conducting (MIEC) membrane which allows the countercurrent flow of electrons i.e., in the opposite direction to O^{2-}.[42–44] There are multiple steps involved in the transfer of oxygen across MIEC membranes. 1) Oxygen molecule adsorbs unto the membrane, combines with electrons and dissociates into O^{2-} on the air side. 2) O^{2-} diffuses through the membrane towards

the methane side as driven by the oxygen partial pressure difference. 3) O^{2-} is transferred from the membrane to the methane-side catalyst where it either reacts with methane or evolves producing electrons. 4) Electrons flow in the opposite direction, returning to the air side to complete the cycle.[45]

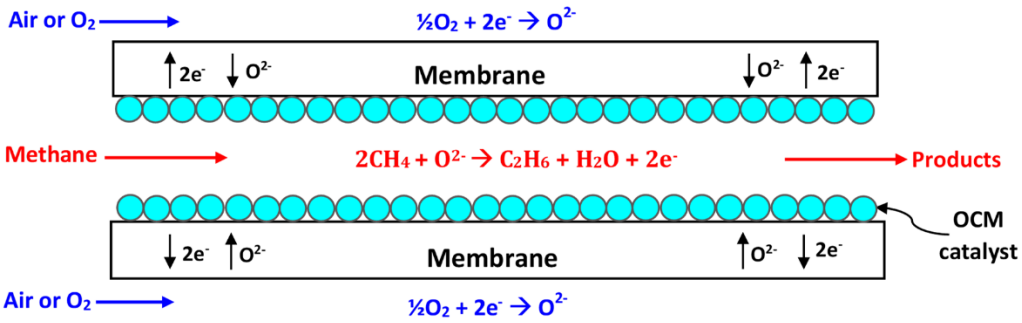

Figure 1.7. Schematic representation of a dense solid oxide membrane plug flow reactor with integrated OCM catalyst

MIEC materials with the best oxygen-ion transport rates are typically oxides with perovskite-type structure.[46,47] Perovskite oxides have an ABO_3 compositional formula (e.g., $BaCeO_3$, $LaGaO_3$) with the A-site cation being larger than the B-site cation in most structures as shown in Figure 1.8.[46,47] O^{2-} conductivity in these materials is made possible due to hopping of oxygen between oxygen vacancies present in the perovskite structure. These oxygen vacancies are formed by acceptor doping of the B site with a lower valent cation. For example, doping the Ce^{4+} sites in $BaCeO_3$ with Gd^{3+}, creates a charge imbalance in the perovskite structure. To preserve charge neutrality the structure releases some of its oxygen, which creates empty oxygen sites known as oxygen vacancies.[47,48] Therefore, when the material is subject to an oxygen partial pressure gradient at high temperatures, oxygen can move across the lattice by "hopping" from one

vacancy to another, which is referred to as O^{2-} conduction.[46,48] The presence of oxygen vacancies in a perovskite oxide is indicated by the oxygen non-stoichiometry (3 – δ), where δ is the extent of oxygen vacancy, defined as the oxygen deficiency per unit volume of ABO_3.[49] The formation of oxygen vacancies is accompanied by the formation of electrons which enable electronic conductivity.[46] The presence or introduction of a multivalent metal cation to the B-site of the structure can contribute to the electronic conductivity by enabling the hopping of electrons between cations with different oxidation states in the lattice.[46–48]

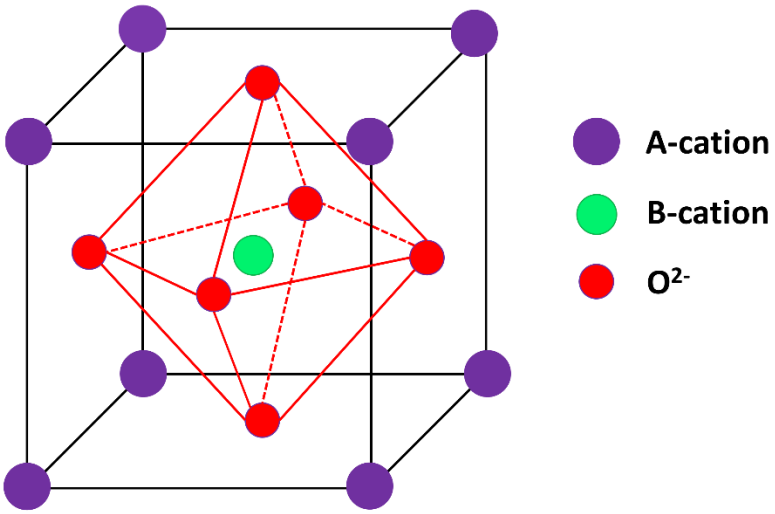

Figure 1.8. Ideal perovskite oxide (ABO_3) structure. A and B represent metal cations (e.g., Ba^{2+} and Ce^{4+} in $BaCeO_3$).

Several operating variables can be modified to tune the oxygen flux across MIEC membranes. These variables include temperature, oxygen partial pressure gradient across the membrane, and membrane thickness. The oxygen flux through the membrane can be increased by increasing the temperature since the oxygen transport is thermally activated and the resistance to this transport (both bulk diffusion and surface kinetics) decreases with increasing temperature.

Increasing the oxygen partial pressure gradient across the membrane increases the driving force for oxygen transfer hence the oxygen flux.[46,50] Another variable that can be controlled to increase the oxygen flux is the membrane thickness. It is generally accepted that decreasing the membrane thickness leads to lower bulk diffusion limitations and improves the oxygen flux until a characteristic thickness where the resistance to oxygen flux switches from predominantly bulk diffusion to surface kinetics controlled.[46,51] In the case where the characteristic thickness has been reached, further improvement in the oxygen flux could be achieved by adding a catalyst on either side of the membrane to accelerate the surface reactions.[52] Therefore, knowing the characteristic thickness of a membrane is useful for optimum system design and some researchers have attempted to estimate this quantity. For example, by tuning the thickness of a $La_{0.3}Sr_{0.7}CoO_{3-\delta}$ membrane, Chen et al[51] estimated the characteristic thickness of the membrane to 80 μm. However, this characteristic thickness is not universally applicable due to differences in membrane compositions and other related properties. Mathematically, the oxygen flux through MIEC membranes controlled by bulk diffusion can be described by the Wagner equation.[52] A simplified Wagner equation for membranes with a good correlation between the oxygen ion conductivity and the oxygen partial pressure is given in Equation 1.1, where J_{O2} represents the oxygen flux, R is the ideal gas constant, F is the Faraday's constant, T is the absolute temperature, L is the thickness of the membrane; σ_i^o is the ionic conductivity at 1 atm, n is an experimentally determined index and p'_{O_2} and p''_{O_2} are the oxygen partial pressures on the oxygen-side and opposite side of membrane, respectively.[52]

$$J_{O_2} = \frac{RT\sigma_i^o}{4F^2L}\left(p'^n_{O_2} - p''^n_{O_2}\right) \tag{1.1}$$

1.7 OCM Reactor Models

1.7.1 Packed bed reactor model

We have used the reaction steps and rate expressions proposed by Stansch et al (Figure 1.6) to develop a reactor model that illustrates the outcome of using a conventional packed bed plug flow reactor for OCM.[22] The conditions applied in the model are a O_2/CH_4 molar feed ratio of 0.25 (stoichiometric ratio for ethane formation from methane and oxygen), temperature of 1073K and a total pressure of 1.1 atm. The net rate expressions were combined with component mole balances to form a series of differential equations that were solved in Matlab.[53] Figure 1.9a shows a plot of the mole fraction of different species in the reactor as a function of space time. The space time is defined as the ratio of catalyst weight to the inlet mass flow rate of methane, which gives a measure of the residence time of methane in the reactor. The data in Figure 1.9a show that oxygen is consumed rapidly near the reactor inlet and that the methane mole fraction attains a near steady value when all oxygen has been consumed. The concentration of ethane produced decreases with increasing space time while that of ethylene increases which is consistent with the proposed mechanism that ethylene is formed sequentially from ethane. The other products formed (CO, CO_2, H_2O and H_2) do not change significantly after all oxygen has been consumed. Although not included in the plot, it should be noted that at much higher space times the products will equilibrate into a mixture of CO, CO_2, H_2O and H_2 due to continuous steam reforming of ethylene (Reaction 8) and the water gas shift reactions (Reaction 9 & 10). Data in Figure 1.9b show that the calculated C_2 selectivity, C_2 yield and CH_4 conversions become nearly constant when oxygen has been completely consumed. In addition, the maximum C_2 yield from the PBR is 16% at a CH_4 conversion and C_2 selectivity of approximately 29% and 57%, respectively. This calculated value of C_2 yield is consistent with the reported experimental value for a La_2O_3/CaO catalyst.[54]

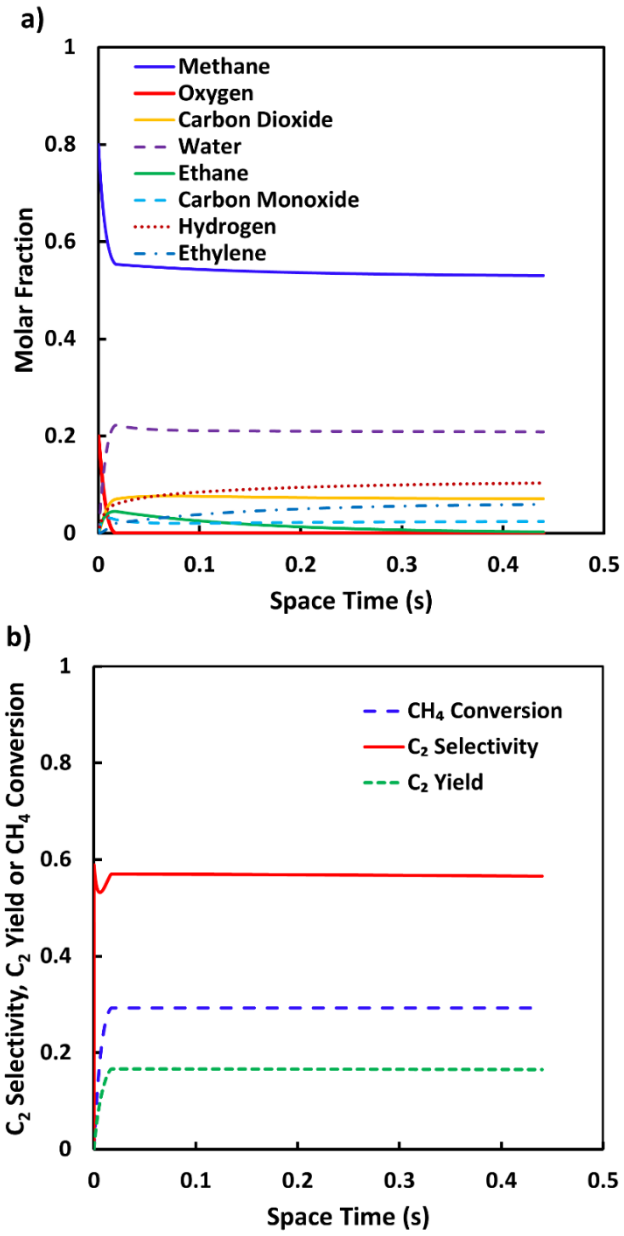

Figure 1.9. Packed bed plug flow reactor model results (a) Plot of mole fraction of species as a function of space time. (b) Plot of C_2 selectivity, C_2 yield and CH_4 conversion as a function of space time. Figure was reproduced from Farrell et al.[22]

To determine the reaction steps with the most influence on C_2 yield and selectivity, a sensitivity analysis was performed on the reaction network. A sensitivity coefficient was calculated for each reaction step using Equation 1.2.[22] The sensitivity coefficient (S_i) is a normalized measure of the impact of a slight pertubation in the rate constant (k_i) of the i^{th} step on the overall C_2 yield or selectivity (Z_{C2}). The rate constant for each reaction step is perturbed by 0.1%, while the rate constants for the remaining steps (k_j) are kept at the published values. δk_i is the change in k_i and δZ_{C2} is the resulting change in the value of Z_{C2} due to perturbation of k_i. If S_i is zero, it implies that C_2 yield or selectivity is not affected by a small change in k_i. A positive S_i indicates that the C_2 yield or selectivity increases as k_i increases. On the other hand, a negative sensitivity coefficient (S_i) means that Z_{C2} decreases as k_i increases. Furthermore, the higher the absolute value of S_i, the higher the rate at which Z_{C2} changes for a given change in k_i

$$S_i = \left(\frac{\partial Z_{C2}}{\partial k_i}\right)_{k_j} \left(\frac{k_i}{Z_{C_2}}\right) \approx \left(\frac{\delta Z_{C2}}{\delta k_i}\right)_{k_j} \left(\frac{k_i}{Z_{C_2}}\right) \tag{1.2}$$

Data in Figure 1.10 show the calculated sensitivity coefficient for the various steps in the reaction network using the packed bed reactor model. As shown in the figure, the C_2 yield and selectivity are mostly affected positively by an increase in the rate of formation of ethane from methane and oxygen (reaction 2). Furthermore, increasing the rate of partial oxidation of ethane to ethylene (reaction 5) has the most significant negative effect on C_2 yield and selectivity. It is somewhat counterintuitive that an increase in the rate of reaction 5 decreases C_2 yield and selectivity since ethylene is also a preferred product. However, this behavior is because the ethylene produced is consumed much more quickly in sequential reactions leading to an overall decrease in C_2 yield. These results imply that a good OCM catalyst should be able to readily activate the C-H bonds in methane and promote its conversion to ethane at high rates. In addition,

an optimal OCM catalyst should also be able to minimize the rates of further oxidation of ethane and ethylene i.e., it should not readily activate the C-H bonds in C_2 products. However, known OCM catalysts that can activate the C-H bonds in methane can typically also activate the C-H bonds in ethane and ethylene at even higher rates.[55] In fact, Stansch et al[20] calculated the ratio of the rate of reaction 5 (partial oxidation of ethane to ethylene) to reaction 2 (formation of ethane from methane) at a selected condition and found that reaction 5 occured about five times as fast as reaction 2. Similarly, the rate of reaction 6 (ethylene oxidation) was calculated to be about 42 times that of reaction 2. Using analogous kinetic arguments, a C_2 yield of 28 – 30% has been estimated as the maximum achievable from OCM.[56,57] Therefore, we infer that simply focusing on catalyst screening in conventional PBRs is unlikely to significantly advance the field of OCM.

1.7.2 Membrane reactor model

To elucidate the potential benefits of using a dense solid oxide membrane reactor over a PBR, we have modeled a membrane plug flow reactor using the same kinetic parameters and reaction conditions applied in the PBR model. In the membrane reactor model, oxygen was not added at the inlet alongside methane as in a PBR model, instead it enters through the sides of the reactor at the reported diffusion rate of oxygen through a state-of-the-art membrane material i.e. $La_{0.6}Sr_{0.4}Co_{0.2}Fe_{0.8}O_{3-\delta}$ (LSCF).[58] Figure 1.11a and 1.11b show the plots of mole fraction of different species, CH_4 conversion, C_2 selectivity and C_2 yield as a function of space time for the membrane plug flow reactor model. Due to distributed oxygen feeding in the membrane reactor model, these results can only be reasonably compared with that of the PBR model at the highest space time plotted (corresponding to the reactor outlet) where the total amount of oxygen, O_2/CH_4 ratio and catalyst mass in both models become equal. At the highest space time, Figure 1.11b

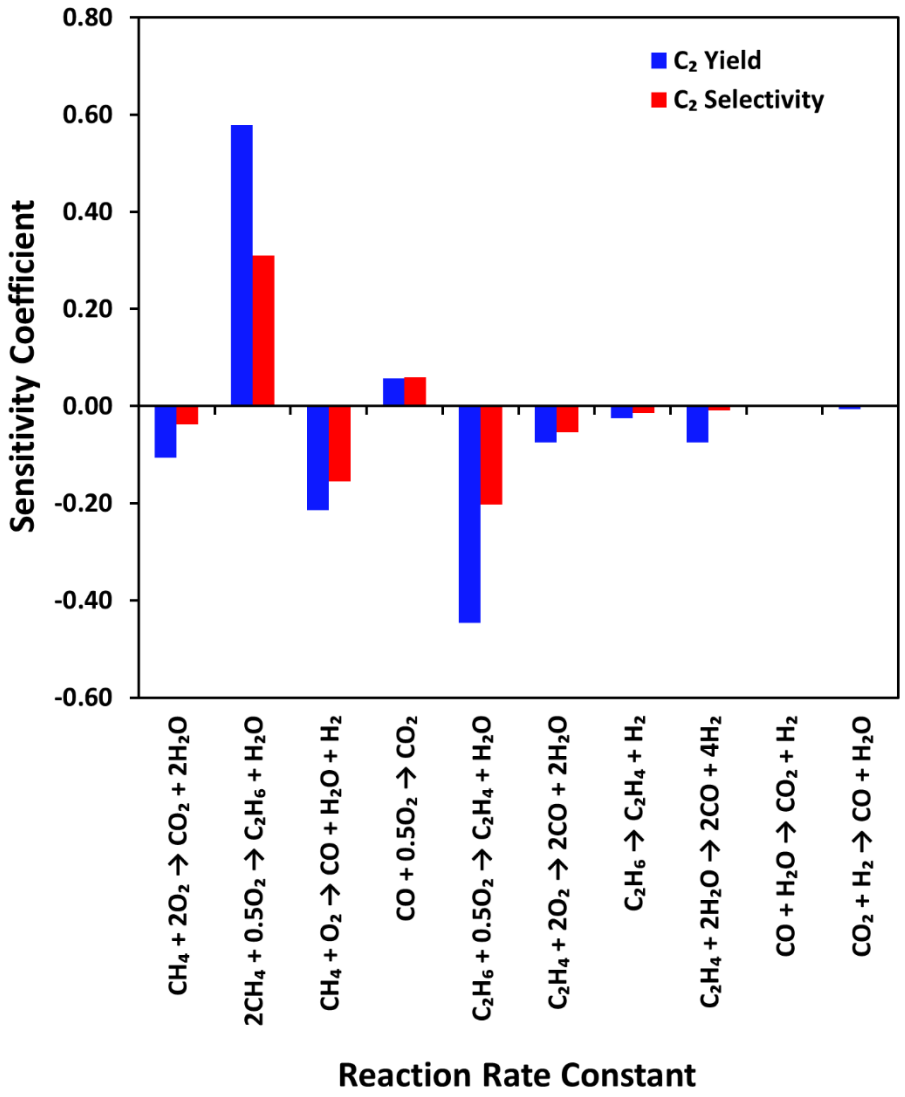

Figure 1.10. Plot of sensitivity co-efficient for C_2 selectivity and C_2 yield for different steps in the reaction network using packed bed reactor model. Figure was reproduced from Farrell et al.[22]

shows that the CH_4 conversion, C_2 selectivity and C_2 yield from the membrane reactions model are 45%, 85% and 38%, respectively. These values are significantly higher than that obtained from the PBR model. The higher C_2 selectivity observed is mainly because the rates of C_2 formation are more favored over CO_x formation at the lower oxygen partial pressures that occur in the membrane reactor model. This observation is consistent with the process kinetics which show a lower order dependence (~ ½ order) of C_2 product formation on the oxygen partial pressure compared to CO_x product formation (~1^{st} order) as mentioned earlier. Interestingly, a higher overall methane conversion was achieved in the membrane reactor model even though the total amount of oxygen was the same as the PBR model. This is attributed to the fact that the reactions leading to C_2 products require less oxygen than the deeper oxidation reactions.

We have also performed a sensitivity analysis on the membrane reactor model. The sensitivity coefficients for the membrane reactor model plotted in Figure 1.12 show that aside from the rate of ethane formation (reaction 2) and rate of ethylene oxidation (reaction 6), the oxygen flux through the membrane also has an even larger impact on the C_2 yield. This result suggests that increasing oxygen flux through the membrane can improve the C_2 yields. It should be noted that due to the relatively low oxygen fluxes through the LSCF membrane (used in our model) and other state-of-the-art membrane materials, the volume of the membrane reactor that would be required to achieve the same total amount of oxygen as the PBR, would be significantly larger than the PBR. This would have an impact on the reactor cost and could also promote sequential reactions of the C_2 products to CO_x downstream. Therefore, one way to improve the performance of the membrane reactors in OCM is to develop membrane materials and utilize membrane designs that enable higher oxygen fluxes compared to the current state-of-the-art membranes.

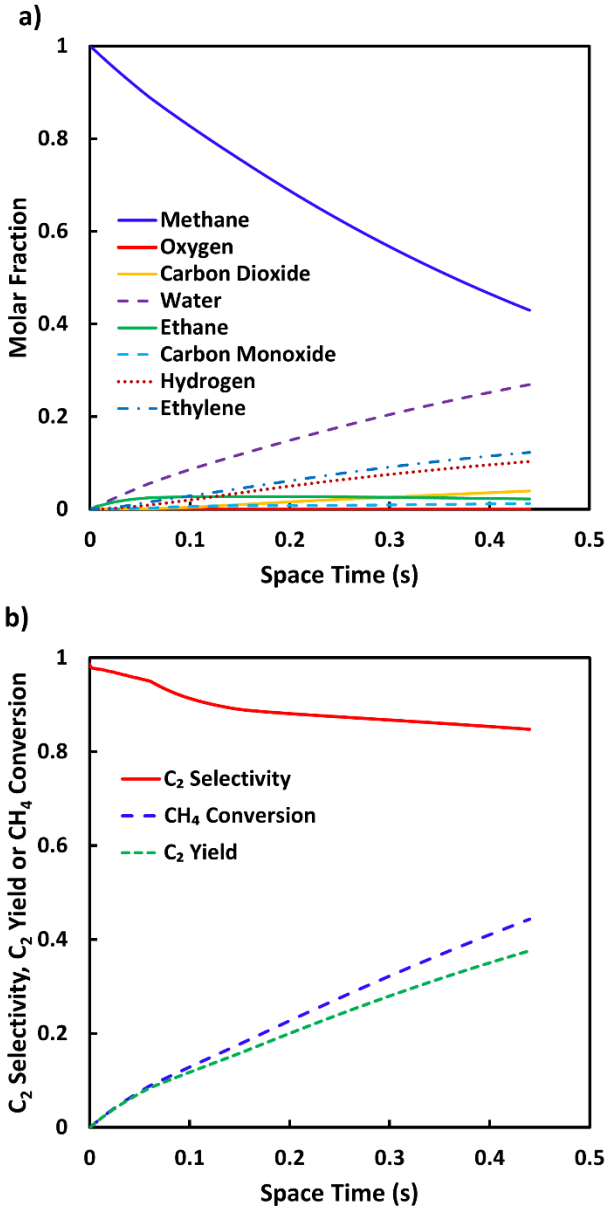

Figure 1.11. Membrane plug flow reactor model results (a) Plot of mole fraction of species and (b) Plot of C_2 selectivity, C_2 yield and CH_4 conversion as a function of space time. Figure was reproduced from Farrell et al.[22]

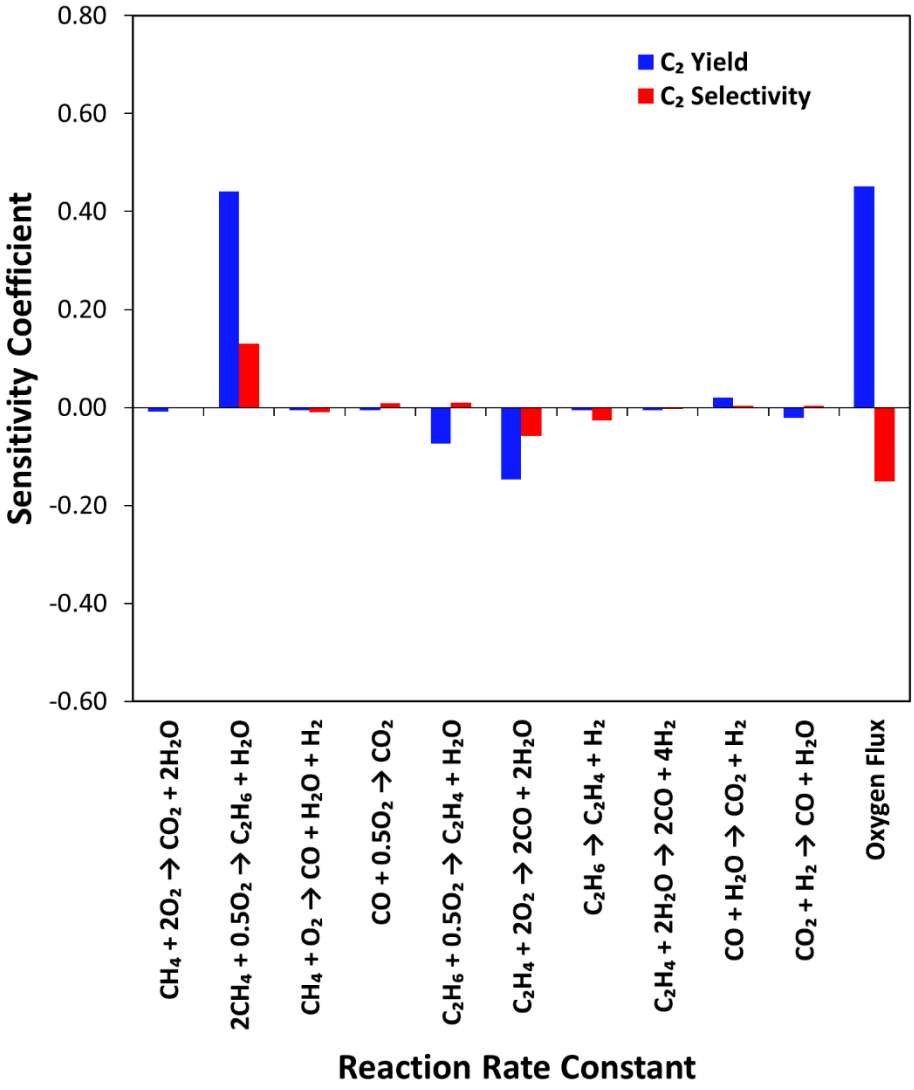

Figure 1.12. Plot of sensitivity co-efficient for C_2 selectivity and C_2 yield for different steps in the reaction network. Figure was reproduced from Farrell et al.[22]

1.8 Catalyst Integration in Solid Oxide Membrane Reactors for OCM

The reactor models presented above show that membrane reactors should, in principle, perform better than PBRs in OCM. However, there have been comparatively much fewer OCM experimental studies in membrane reactors compared to PBRs, and the performance of the membrane reactors have not met the techno-economic target.[22] An important research direction in the development of solid oxide membrane reactors for OCM is to identify and integrate selective OCM catalysts with the membranes. Not all membrane reactors previously tested in OCM included an OCM catalyst on the methane-side of the membrane. In other words, the membranes in these studies, which are typically unselective for OCM, performed a dual role of activating methane as well as conducting O^{2-} ions. However, it has been reported that the inclusion of a selective OCM catalyst on the methane-side of the membrane can lead to significantly higher C_2 selectivities and yields.[59,60] For example, Tan et al[59] demonstrated that by including an additional $SrTi_{0.9}Li_{0.1}O_3$ catalyst in a LSCF membrane reactor, the C_2 yield could be improved from 14% to 21% at 1248 K. Therefore, it is important that future membrane reactor designs incorporate OCM catalysts for improved performance.

Aside from having a high selectivity for OCM, it is important to ensure that the integrated catalysts have good O^{2-} conductivity and are compatible with the membrane material. The ionic conductivity of the catalyst is desired to allow the facile transfer of O^{2-} ions from the membrane to the catalyst layer while preventing recombination of the ions to undesired gas-phase O_2.[60,61] To enable sufficient contact area between catalyst and membrane for facile O^{2-} transport between layers, the catalysts are typically adhered to the membrane by firing at elevated temperatures prior to reactor tests.[60,61] Furthermore, the catalyst layers have to remain in close contact to the membrane under the high temperature conditions ($\geq$ 973K) used in reactor tests. At such high

temperatures, solid-state reactions can occur between the membrane and catalyst which can lead to undesired changes in the properties (e.g., conductivity, activity or selectivity) of the materials.[62] In addition, if the membrane and catalyst expand at different rates with temperature, it can lead to cracking of the membrane or separation of both layers at high temperatures. Therefore, the membrane and catalyst material should have similar thermal expansion co-efficients.[63] One way to fulfil all of these criteria is to employ a membrane and catalyst of the same or similar composition

Furthermore, to ensure long-term stability, the integrated catalyst should not only be compatible with the membrane material, but also resistant to solid carbon-induced catalyst deactivation. OCM membrane reactors are highly susceptible to carbon deposition issues (also known as coking) due to the presence of low O_2/CH_4 ratios and high ethylene concentrations at high operating temperatures. As shown in Figure 1.4b, the thermodynamically favored product in the limit of low O_2/CH_4 ratios is solid carbon. This carbon deposition can poison the active sites on the catalyst leading to a decline in its performance over time. Although, the coked membrane/catalyst can be intermittently regenerated by high temperature oxidation, developing systems that are resistant to carbon deposition is important as this will minimize the number of costly regeneration cycles in long-term (e.g., commercial) operations.

1.9 Scope of the Dissertation

The overall objective of this dissertation is to identify and integrate selective OCM catalysts and membranes in solid oxide membranes reactors, improve the understanding of these reactors and demonstrate that they can provide improved C_2 selectivity and yield compared to conventional co-fed reactors applied in OCM. In our membrane reactor design, we focus on

utilizing membrane materials of similar composition as the integrated OCM catalysts in order to minimize incompatibility issues and promote long-term stability.

In Chapter 2, a description of the experimental techniques used to obtain the data in this dissertation is presented. It begins with a description of the synthesis techniques and experimental set-up followed by a detailed description of the various characterization techniques used in this work. The information in the chapter would serve as an important guide for researchers who wish to reproduce the experimental work in this dissertation.

The work in Chapter 3 is focused on identifying O^{2-} conducting membrane – catalyst materials for application in OCM. We chose to study a gadolinium-doped barium cerate ($BaCe_{0.8}Gd_{0.2}O_{3-\delta}$ or BCG) perovskite because it is an O^{2-} conducting material composed of elements that have been shown to be selective in OCM. This work was conducted using a conventional co-fed PBR. We present conversion-selectivity and conversion-yield curves that illustrate the OCM performance of BCG. While this material was found to be active and selective for OCM, we found that its perovskite phase, which is required for its conductive (membrane) properties, decomposes into carbonate and oxide phases due to reactions with CO_2. We demonstrate that doping BCG with Zr was effective at suppressing the phase instability in OCM without significantly affecting the C_{2+} yields in a PBR.

In Chapter 4, selected membrane-catalyst materials were studied in small button-shaped membrane reactors. The materials investigated were all perovskite oxides and include BCG, Zr-doped BCG ($BaCe_{0.4}Zr_{0.4}Gd_{0.2}O_{3-\delta}$) and $La_{0.8}Sr_{0.2}Ga_{0.8}Mg_{0.2}O_{3-\delta}$. This preliminary study was done to identify the most promising membrane-catalyst material for further studies in a tubular membrane reactor. We were particularly interested in determining the stability of the materials against carbon-induced deactivation at low O_2/CH_4 ratios that occur in practical OCM membrane

reactors. The results obtained show that BCG gives excellent resistance to carbon-induced deactivation and the best oxygen permeation rates among the tested materials.

In Chapter 5, BCG tubular membranes were fabricated using Cu as a sintering additive and studied in OCM. The Cu modified BCG (Cu-BCG) membranes were tested as a membrane reactor (with distributed oxygen feed) and as a co-fed reactor (where methane was fed together with oxygen from one inlet). The data show that the Cu-BCG membrane reactor achieves significantly higher C_2 selectivity compared to a co-fed reactor at similar methane conversions. These results provide conclusive experimental evidence in support of our overall hypothesis of the improved OCM performance of a catalytic membrane reactor over a conventional co-fed reactor. Data on the stability of the Cu-BCG membrane reactor over time is also presented and discussed.

Chapter 6 is the final chapter of this dissertation and presents the main conclusions from this study as well as recommendations for future work.

1.10 References

(1) U.S. Crude Oil, Natural Gas, and Natural Gas Proved Reserves, Year-end 2018 https://www.eia.gov/naturalgas/crudeoilreserves/ (accessed Dec 17, 2019).

(2) Liang, F.-Y.; Ryvak, M.; Sayeed, S.; Zhao, N. The Role of Natural Gas as a Primary Fuel in the near Future, Including Comparisons of Acquisition, Transmission and Waste Handling Costs of as with Competitive Alternatives. *Chem. Cent. J.* **2012**, *6* (1), S4.

(3) EIA - Annual Energy Outlook 2016 https://www.eia.gov/outlooks/archive/aeo16/ (accessed Dec 17, 2019)

(4) Wang, Q.; Chen, X.; Jha, A. N.; Rogers, H. Natural Gas from Shale Formation–the Evolution, Evidences and Challenges of Shale Gas Revolution in United States. *Renew. Sustain. Energy Rev.* **2014**, *30*, 1–28.

(5) Horn, R.; Schlögl, R. Methane Activation by Heterogeneous Catalysis. *Catal. Lett.* **2015**, *145* (1), 23–39.

(6) Gür, T. M. Comprehensive Review of Methane Conversion in Solid Oxide Fuel Cells: Prospects for Efficient Electricity Generation from Natural Gas. *Prog. Energy Combust. Sci.* **2016**, *54*, 1–64.

(7) Increased Shale Oil Production and Political Conflict Contribute to Increase in Global Gas Flaring https://www.worldbank.org/en/news/press-release/2019/06/12/increased-shale-oil-

production-and-political-conflict-contribute-to-increase-in-global-gas-flaring (accessed Dec 17, 2019).

(8) Lunsford, J. H. Catalytic Conversion of Methane to More Useful Chemicals and Fuels: A Challenge for the 21st Century. *Catal. Today* **2000**, *63* (2), 165–174.

(9) McFarland, E. Unconventional Chemistry for Unconventional Natural Gas. *Science* **2012**, *338* (6105), 340–342.

(10) Guo, X.; Fang, G.; Li, G.; Ma, H.; Fan, H.; Yu, L.; Ma, C.; Wu, X.; Deng, D.; Wei, M.; et al. Direct, Nonoxidative Conversion of Methane to Ethylene, Aromatics, and Hydrogen. *Science* **2014**, *344* (6184), 616–619.

(11) Olivos-Suarez, A. I.; Szécsényi, À.; Hensen, E. J.; Ruiz-Martinez, J.; Pidko, E. A.; Gascon, J. Strategies for the Direct Catalytic Valorization of Methane Using Heterogeneous Catalysis: Challenges and Opportunities. *ACS Catal.* **2016**, *6* (5), 2965–2981.

(12) Lotz, M. D.; Remy, M. S.; Lao, D. B.; Ariafard, A.; Yates, B. F.; Canty, A. J.; Mayer, J. M.; Sanford, M. S. Formation of Ethane from Mono-Methyl Palladium (II) Complexes. *J. Am. Chem. Soc.* **2014**, *136* (23), 8237–8242.

(13) Keller, G. E.; Bhasin, M. M. Synthesis of Ethylene via Oxidative Coupling of Methane: I. Determination of Active Catalysts. *J. Catal.* **1982**, *73* (1), 9–19.

(14) Ghose, R.; Hwang, H. T.; Varma, A. Oxidative Coupling of Methane Using Catalysts Synthesized by Solution Combustion Method. *Appl. Catal. Gen.* **2013**, *452*, 147–154.

(15) Galadima, A.; Muraza, O. Revisiting the Oxidative Coupling of Methane to Ethylene in the Golden Period of Shale Gas: A Review. *J. Ind. Eng. Chem.* **2016**, *37*, 1–13.

(16) Cruellas, A.; Bakker, J. J.; van Sint Annaland, M.; Medrano, J. A.; Gallucci, F. Techno-Economic Analysis of Oxidative Coupling of Methane: Current State of the Art and Future Perspectives. *Energy Convers. Manag.* **2019**, *198*, 111789.

(17) Driscoll, D. J.; Martir, W.; Wang, J. X.; Lunsford, J. H. Formation of Gas-Phase Methyl Radicals over Magnesium Oxide. *J. Am. Chem. Soc.* **1985**, *107* (1), 58–63.

(18) Luo, L.; Tang, X.; Wang, W.; Wang, Y.; Sun, S.; Qi, F.; Huang, W. Methyl Radicals in Oxidative Coupling of Methane Directly Confirmed by Synchrotron VUV Photoionization Mass Spectroscopy. *Sci. Rep.* **2013**, *3*.

(19) V. Kondratenko, E.; Peppel, T.; Seeburg, D.; A. Kondratenko, V.; Kalevaru, N.; Martin, A.; Wohlrab, S. Methane Conversion into Different Hydrocarbons or Oxygenates: Current Status and Future Perspectives in Catalyst Development and Reactor Operation. *Catal. Sci. Technol.* **2017**, *7* (2), 366–381.

(20) Stansch, Z.; Mleczko, L.; Baerns, M. Comprehensive Kinetics of Oxidative Coupling of Methane over the La_2O_3/CaO Catalyst. *Ind. Eng. Chem. Res.* **1997**, *36* (7), 2568–2579.

(21) Zavyalova, U.; Holena, M.; Schlögl, R.; Baerns, M. Statistical Analysis of Past Catalytic Data on Oxidative Methane Coupling for New Insights into the Composition of High-Performance Catalysts. *ChemCatChem* **2011**, *3* (12), 1935–1947.

(22) Farrell, B. L.; Igenegbai, V. O.; Linic, S. A Viewpoint on Direct Methane Conversion to Ethane and Ethylene Using Oxidative Coupling on Solid Catalysts. *ACS Catal.* **2016**, *6* (7), 4340–4346.

(23) Kuo, J. C. W.; Kresge, C. T.; Palermo, R. E. Evaluation of Direct Methane Conversion to Higher Hydrocarbons and Oxygenates. *Catal. Today* **1989**, *4* (3–4), 463–470.

(24) Lu, Y.; Dixon, A. G.; Moser, W. R.; Ma, Y. H.; Balachandran, U. Oxygen-Permeable Dense Membrane Reactor for the Oxidative Coupling of Methane. *J. Membr. Sci.* **2000**, *170* (1), 27–34.

(25) Levenspiel, O. *Chemical Reaction Engineering*; John Wiley & Sons: New York, 1999.

(26) Palermo, A.; Holgado Vazquez, J. P.; Lambert, R. M. New Efficient Catalysts for the Oxidative Coupling of Methane. *Catal. Lett.* **2000**, *68* (3), 191–196.

(27) Wu, J.; Zhang, H.; Qin, S.; Hu, C. La-Promoted $Na_2WO_4/Mn/SiO_2$ Catalysts for the Oxidative Conversion of Methane Simultaneously to Ethylene and Carbon Monoxide. *Appl. Catal. Gen.* **2007**, *323*, 126–134.

(28) Zarrinpashne, S.; Ahmadi, R.; Zekordi, S. Catalyst Direct Conversion of Methane to Ethane and Ethylene. US20060155157A1, July 13, 2006.

(29) Choudhary, V. R.; Mulla, S. a. R.; Pandit, M. Y.; Chaudhari, S. T.; Rane, V. H. Influence of Precursors of Li_2O and MgO on Surface and Catalytic Properties of Li-Promoted MgO in Oxidative Coupling of Methane. *J. Chem. Technol. Biotechnol.* **2000**, *75* (9), 828–834.

(30) Murata, K.; Hayakawa, T.; Fujita, K. Excellent Effect of Lithium-Doped Sulfated Zirconia Catalysts Foroxidative Coupling of Methane to Give Ethene and Ethane. *Chem. Commun.* **1997**, No. 2, 221–222.

(31) Matsuura, I.; Utsumi, Y.; Nakai, M.; Doi, T. Oxidative Coupling of Methane over Lithium-Promoted Zinc Oxide Catalyst. *Chem. Lett.* **1986**, *15* (11), 1981–1984.

(32) Zeng, Y.; Akin, F. T.; Lin, Y. S. Oxidative Coupling of Methane on Fluorite-Structured Samarium–yttrium–bismuth Oxide. *Appl. Catal. Gen.* **2001**, *213* (1), 33–45.

(33) Bagherzadeh, E.; Hassan, A.; Hassan, A. Preparation of Catalyst and Use for High Yield Conversion of Methane to Ethylene. US20040220053A1, November 4, 2004.

(34) Sun, J.; Thybaut, J. W.; Marin, G. B. Microkinetics of Methane Oxidative Coupling. *Catal. Today* **2008**, *137* (1), 90–102.

(35) Takanabe, K.; Iglesia, E. Mechanistic Aspects and Reaction Pathways for Oxidative Coupling of Methane on $Mn/Na_2WO_4/SiO_2$ Catalysts. *J. Phys. Chem. C* **2009**, *113* (23), 10131–10145.

(36) Wolf, E. E. Methane to Light Hydrocarbons via Oxidative Methane Coupling: Lessons from the Past to Search for a Selective Heterogeneous Catalyst. *J. Phys. Chem. Lett.* **2014**, *5* (6), 986–988.

(37) Luo, L.; You, R.; Liu, Y.; Yang, J.; Zhu, Y.; Wen, W.; Pan, Y.; Qi, F.; Huang, W. Gas-Phase Reaction Network of Li/MgO-Catalyzed Oxidative Coupling of Methane and Oxidative Dehydrogenation of Ethane. *ACS Catal.* **2019**, *9* (3), 2514–2520.

(38) Daneshpayeh, M.; Khodadadi, A.; Mostoufi, N.; Mortazavi, Y.; Sotudeh-Gharebagh, R.; Talebizadeh, A. Kinetic Modeling of Oxidative Coupling of Methane over $Mn/Na_2WO_4/SiO_2$ Catalyst. *Fuel Process. Technol.* **2009**, *90* (3), 403–410.

(39) Ghiasi, M.; Malekzadeh, A.; Hoseini, S.; Mortazavi, Y.; Khodadadi, A.; Talebizadeh, A. Kinetic Study of Oxidative Coupling of Methane over Mn and/or W Promoted Na_2SO_4/SiO_2 Catalysts. *J. Nat. Gas Chem.* **2011**, *20* (4), 428–434.

(40) Tiemersma, T. P.; Tuinier, M. J.; Gallucci, F.; Kuipers, J. A. M.; van Sint Annaland, M. A Kinetics Study for the Oxidative Coupling of Methane on a $Mn/Na_2WO_4/SiO_2$ Catalyst. *Appl. Catal. Gen.* **2012**, *433*, 96–108.

(41) Arndt, S.; Otremba, T.; Simon, U.; Yildiz, M.; Schubert, H.; Schomäcker, R. Mn–Na_2WO_4/SiO_2 as Catalyst for the Oxidative Coupling of Methane. What Is Really Known? *Appl. Catal. Gen.* **2012**, *425*, 53–61.

(42) Eng, D.; Stoukides, M. Catalytic and Electrocatalytic Methane Oxidation with Solid Oxide Membranes. *Catal. Rev.* **1991**, *33* (3–4), 375–412.

(43) Sunarso, J.; Baumann, S.; Serra, J. M.; Meulenberg, W. A.; Liu, S.; Lin, Y. S.; Da Costa, J. D. Mixed Ionic–electronic Conducting (MIEC) Ceramic-Based Membranes for Oxygen Separation. *J. Membr. Sci.* **2008**, *320* (1), 13–41.

(44) Bouwmeester, H. J.; Burggraaf, A. J. Dense Ceramic Membranes for Oxygen Separation. In *Membrane Science and Technology*; Elsevier, 1996; Vol. 4, pp 435–528.

(45) Arratibel Plazaola, A.; Cruellas Labella, A.; Liu, Y.; Badiola Porras, N.; Pacheco Tanaka, D. A.; Annaland, S.; Van, M.; Gallucci, F. Mixed Ionic-Electronic Conducting Membranes (MIEC) for Their Application in Membrane Reactors: A Review. *Processes* **2019**, *7* (3), 128.

(46) Sunarso, J.; Baumann, S.; Serra, J. M.; Meulenberg, W. A.; Liu, S.; Lin, Y. S.; Da Costa, J. D. Mixed Ionic–electronic Conducting (MIEC) Ceramic-Based Membranes for Oxygen Separation. *J. Membr. Sci.* **2008**, *320* (1), 13–41.

(47) Ellett, A. J. *Oxygen Permeation and Thermo-Chemical Stability of Oxygen Separation Membrane Materials for the Oxyfuel Process*; Forschungszentrum Jülich, 2010; Vol. 43.

(48) ten Elshof, J. E.; Bouwmeester, H. J. M.; Verweij, H. Oxidative Coupling of Methane in a Mixed-Conducting Perovskite Membrane Reactor. *Appl. Catal. Gen.* **1995**, *130* (2), 195–212.

(49) Maiti, D.; Daza, Y. A.; Yung, M. M.; Kuhn, J. N.; Bhethanabotla, V. R. Oxygen Vacancy Formation Characteristics in the Bulk and across Different Surface Terminations of $La_{(1-x)}Sr_xFe_{(1-y)}Co_yO_{(3-\delta)}$ Perovskite Oxides for CO2 Conversion. *J. Mater. Chem. A* **2016**, *4* (14), 5137–5148.

(50) Zeng, Y.; Lin, Y. S.; Swartz, S. L. Perovskite-Type Ceramic Membrane: Synthesis, Oxygen Permeation and Membrane Reactor Performance for Oxidative Coupling of Methane. *J. Membr. Sci.* **1998**, *150* (1), 87–98.

(51) Chen, C. H.; Bouwmeester, H. J. M.; van Doorn, R. H. E.; Kruidhof, H.; Burggraaf, A. J. Oxygen Permeation of $La_{0.3}Sr_{0.7}CoO_{3-\delta}$. *Solid State Ion.* **1997**, *98* (1), 7–13.

(52) Smart, S.; Diniz Da Costa, J. C.; Baumann, S.; Meulenberg, W. A. 9 - Oxygen Transport Membranes: Dense Ceramic Membranes for Power Plant Applications. In *Advanced Membrane Science and Technology for Sustainable Energy and Environmental Applications*; Basile, A., Nunes, S. P., Eds.; Woodhead Publishing Series in Energy; Woodhead Publishing, 2011; pp 255–292.

(53) Fogler, H. S. *Elements of Reaction Engineering.*, 4th Ed.; Prentice-Hall: Upper Saddle River, NJ, 2006.

(54) Mleczko, L.; Pannek, U.; Rothaemel, M.; Baerns, M. Oxidative Coupling of Methane over a La_2O_3/CaO Catalyst. Optimization of Reaction Conditions in a Bubbling Fluidized-Bed Reactor. *Can. J. Chem. Eng.* **1996**, *74* (2), 279–287.

(55) Labinger, J. A.; Ott, K. C. Mechanistic Studies on the Oxidative Coupling of Methane. *J. Phys. Chem.* **1987**, *91* (11), 2682–2684.

(56) Labinger, J. A. Oxidative Coupling of Methane: An Inherent Limit to Selectivity? *Catal. Lett.* **1988**, *1* (11), 371–375.

(57) San Su, Y.; Ying, J. Y.; Green Jr, W. H. Upper Bound on the Yield for Oxidative Coupling of Methane. *J. Catal.* **2003**, *218* (2), 321–333.

(58) Akin, F. T.; Lin, J. Y. S. Oxygen Permeation through Oxygen Ionic or Mixed-Conducting Ceramic Membranes with Chemical Reactions. *J. Membr. Sci.* **2004**, *231* (1), 133–146.

(59) Tan, X.; Pang, Z.; Gu, Z.; Liu, S. Catalytic Perovskite Hollow Fibre Membrane Reactors for Methane Oxidative Coupling. *J. Membr. Sci.* **2007**, *302* (1), 109–114.

(60) Olivier, L.; Haag, S.; Mirodatos, C.; van Veen, A. C. Oxidative Coupling of Methane Using Catalyst Modified Dense Perovskite Membrane Reactors. *Catal. Today* **2009**, *142* (1–2), 34–41.

(61) Othman, N. H.; Wu, Z.; Li, K. An Oxygen Permeable Membrane Microreactor with an in-Situ Deposited $Bi_{1.5}Y_{0.3}Sm_{0.2}O_{3-\delta}$ Catalyst for Oxidative Coupling of Methane. *J. Membr. Sci.* **2015**, *488*, 182–193.

(62) Farrell, B.; Linic, S. Oxidative Coupling of Methane over Mixed Oxide Catalysts Designed for Solid Oxide Membrane Reactors. *Catal. Sci. Technol.* **2016**.

(63) Ormerod, R. M. Solid Oxide Fuel Cells. *Chem. Soc. Rev.* **2003**, *32* (1), 17–28.

Chapter 2

Experimental Techniques

2.1 Summary

This chapter presents a description of the various experimental techniques used in this dissertation work. It begins with a description of the procedures used to synthesize the catalysts and membranes for the OCM experiments. This is followed by a description of the experimental set-ups and the procedures used in the tests. Lastly, a detailed description of the various characterization techniques (microscopic and spectroscopic) used in this work is presented including the fundamental principles behind each technique. The information in this chapter would serve as a useful guide for researchers who wish to replicate the experimental work in this dissertation.

2.2 Synthesis Techniques

2.2.1 Synthesis of packed bed reactor catalysts

The catalysts tested for OCM in the packed bed reactor were synthesized using a modified Pechini sol-gel method.[1,2] Two perovskite oxide catalysts were synthesized: $BaCe_{0.8}Gd_{0.2}O_{3-\delta}$ (BCG) and a $BaCe_{0.4}Zr_{0.4}Gd_{0.2}O_{3-\delta}$ (BCZG). Details of the materials used in the synthesis including manufacturer and purity levels are given in Table 2.1. It includes high-purity metal nitrates, ethylenediaminetetraacetic acid (EDTA), aqueous ammonia (NH_4OH), ethylene glycol (EG) and deionized water. The EDTA serves as a chelating agent, while ethylene glycol serves as a polymerizing agent.[2–4] The molar ratio of EDTA to metal ion was 3/2, while that of EDTA to ethylene glycol was 1/3.

The overall synthesis procedure is illustrated in Figure 2.1. EDTA was added into a measured amount of DI water followed by the addition of NH_4OH, which aids the dissolution of EDTA. The measured pH of the solution after mixing with NH_4OH was ~10. In a separate beaker, stoichiometric amount of barium nitrate was dissolved in DI water while stirring at 80°C. The clear EDTA/NH_4OH solution was poured into the barium nitrate solution and labelled solution A. A separate solution (solution B) was prepared by dissolving stoichiometric amount of the remaining metal nitrates (i.e., cerium (III) nitrate hexahydrate and gadolinium (III) nitrate hexahydrate) in DI water with the aid of a sonicator. In the case of BCZG, a stoichiometric amount of zirconium dinitrate oxide hydrate was also added to solution B. Solution B was then added slowly (drop by drop) to solution A while stirring at 80°C. This dropwise addition helps prevent irreversible precipitation of the metal salts resulting in a clear solution. After mixing the two solutions, a measured amount of ethylene glycol was added. The beaker was sealed and left to stir over night at 80°C to promote polymerization between the EDTA and ethylene glycol. Thereafter, the

solution was opened and left to evaporate until a transparent gel like residue was formed. The gel was subsequently calcined at 250°C for 2 hours to form a black ash, which was lightly ground in a mortar and pestle. The black ash was calcined further at 1000°C for 4 hours to decompose any organics and form the final perovskite powders.

Table 2.1. Materials used in the synthesis of packed bed reactor catalysts

Chemical	Manufacturer or Vendor	Purity Level
Ethylenediaminetetraacetic acid (EDTA)	Fisher Scientific	99.7%
Aqueous ammonia (29% NH_4OH)	Fisher Scientific	> 95%
Barium nitrate [Ba $(NO_3)_2$]	Sigma Aldrich	≥ 99%
Cerium (III) nitrate hexahydrate [Ce $(NO_3)_3 \cdot 6H_2O$]	Acros Organics	99.5%
Gadolinium (III) nitrate hexahydrate [Gd $(NO_3)_3 \cdot 6H_2O$]	Acros Organics	99.9%
Zirconium dinitrate oxide hydrate [ZrO $(NO_3)_2 \bullet xH_2O$], x ~1.8	Alfa Aesar	99.9%
Ethylene Glycol ($C_2H_6O_2$)	J.T. Baker	≥ 99%

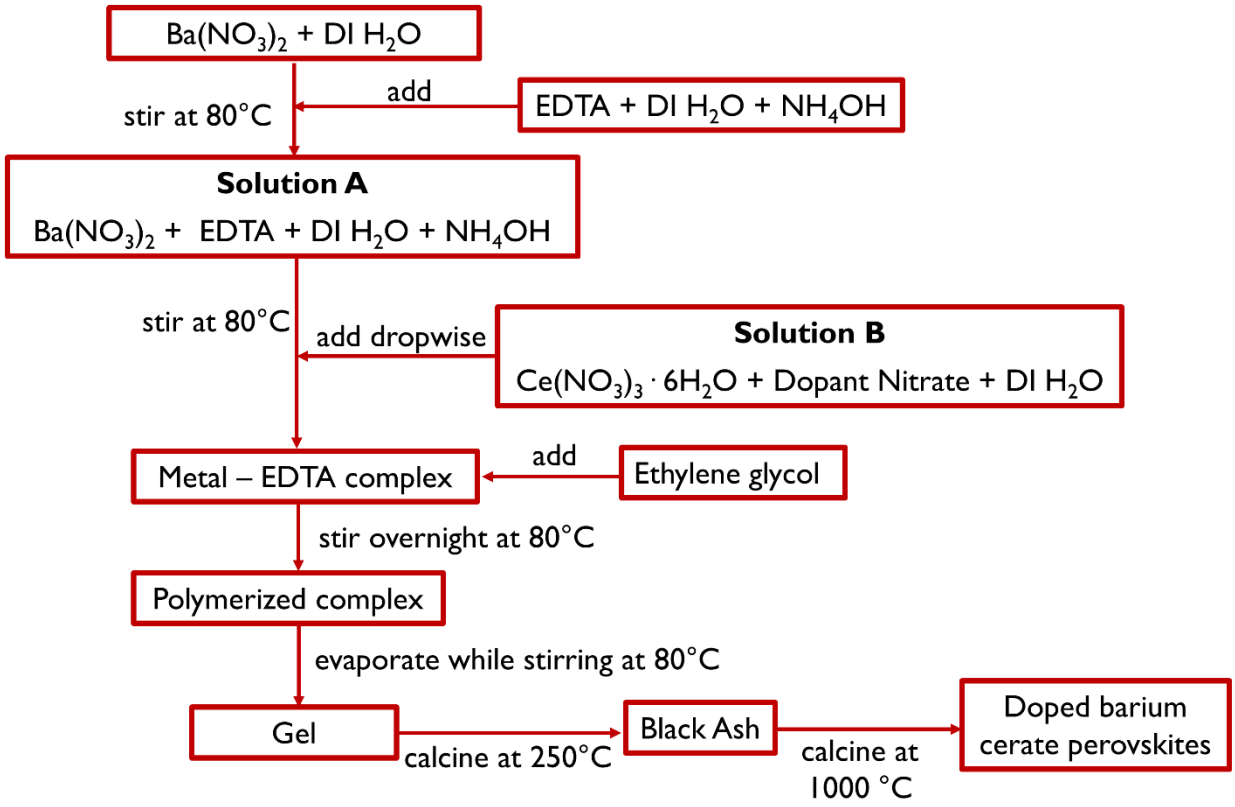

Figure 2.1. Procedure for the synthesis of doped barium cerate perovskite oxide powders using the modified pechini method.

2.2.2 Synthesis of button membranes

Button-shaped membrane reactors were synthesized and tested in OCM. These membranes have limited surface area compared to tubular membranes but are relatively easier to synthesize and require less material. The button membranes were used for preliminary performance evaluation of the membranes/catalysts in order to identify the most promising materials. In the button membranes, a thin porous layer of higher surface area was coated on one side of the membranes to act as the OCM catalyst and increase the ratio of active surface area to volume. Catalysts were of the same or similar composition to the membrane. This catalyst/membrane matching helps prevent undesired chemical reactions between the membrane and catalyst, in

addition to minimizing thermal stress. Three different button membrane/catalyst systems were synthesized in this work**.** This includes a BCG membrane coated with a BCG catalyst (BCG/BCG), a BCZG membrane coated with a BCZG catalyst (BCZG/BCZG) and a Ni doped $La_{0.8}Sr_{0.2}Ga_{0.8}Mg_{0.2}O_{3-\delta}$ (LSGM) membrane coated with LSGM catalyst (Ni-LSGM/LSGM). Note that the membrane portion of the LSGM system was doped with 15 mol% Ni to ensure its electron conductivity, since LSGM by itself has poor electron conductivity.[5,6] This was achieved by mixing LSGM (Sigma Aldrich, 99%) and NiO (Alfa Aesar, 99%) in a weight ratio of 5:0.28 using an agate mortar and pestle. The mixture was then placed on a yttria-stabilized zirconia (YSZ) plate and calcined in a muffle furnace at 1000°C for 6 hours using ramp rates of 2°C/min.

To synthesize the button membranes, the perovskite powders were first sifted through a 75 µm stainless steel sieve. A measured amount of sifted perovskite powders (0.3g of BCG or BCZG and 0.36g of Ni-LSGM) was uniaxially pressed into pellets in a 15 mm die press at ~ 40 MPa for 2-3 minutes. The pellets were carefully transferred onto a YSZ plate, which was previously covered with a powder bath of respective perovskite powders. The powder bath is necessary to help minimize chemical reaction of the pellets with the YSZ plate at the high fabrication temperatures. The pellets were covered with an extra layer of respective perovskite powders to minimize contamination and mitigate the evaporation of Ba from the doped barium cerate membranes at high temperatures.[7,8] The porous pellets were then transferred to a furnace where they were sintered at high temperature to transform them into dense (non-porous and gas-tight) membranes. The Ni-LSGM membranes were sintered at 1450°C for 4 hours while the BCG and BCZG membranes were sintered at 1650°C for 5 hours using slow ramp rates of 1°C/min to prevent cracking of the membranes due to thermal stress. The as-pressed pellets were 15 mm in diameter

while the sintered membranes were ~ 10 mm in diameter, corresponding to a linear shrinkage of ~ 33%. The final thickness of the sintered membranes was ~ 500 µm.

The catalyst layers were prepared by mixing respective perovskite powders (BCG, BCZG or LSGM) with graphite (Alfa Aesar, 75-micron size) in a 3:1 weight ratio using a mortar and pestle. 0.2 g of the mixture was first mixed with 600 µL of ethanol to form a suspension, then 25 µL of the suspension was drop-coated one side of the membranes. To minimize inconsistency in the area coated by the catalyst suspension, the surface of each membrane was first covered with Kapton tape containing a 3/8-inch center hole before drop-coating. After a few minutes of drying, the Kapton tape was peeled off the membrane leaving behind a circular layer of the catalyst coating. The coated membranes were covered with glass vials and left to dry slowly overnight to prevent cracking of the layers. Thereafter, they were transferred to a muffle furnace and calcined at 1150°C for 2 hours (for the LSGM system) or 1500°C for 4 hours (for the BCG and BCZG system) using ramp rates of 2°C/min. The calcination step burns off the graphite in the catalyst layers to create pores and adheres the catalysts to the membranes.

2.2.3 Synthesis of tubular membranes

Tubular BCG membranes were fabricated using a combination of slip-casting, solid-state reaction (SSR) and sintering. Slip-casting is a well-known traditional technique used for the preparation of ceramic objects with complex shapes and forms. It offers the advantage of being cheaper than extrusion-based methods of fabricating tubular membranes as it requires less equipment.[9,10] Specific details of the slip-casting process developed in this work is discussed later in this section. SSR is the traditional method used in synthesizing perovskite oxide powders. It is achieved by thoroughly mixing carbonate and oxide precursor powders, then heating the mixture to high temperatures for several hours.[11] For example, the synthesis of BCG by SSR can be

accomplished by ball milling a mixture $BaCO_3$, CeO_2 and Gd_2O_3 powder in stoichiometric weight ratios, followed by calcination in air at 1350°C for 6 – 10 hours.[12,13] The perovskite phase is formed due to diffusion of metal cations across the solid-solid interfaces of the different crystalline phases in the sample and the nucleation of the perovskite at the interfaces.[11] Compared to solution-based methods (e.g., sol gel), membranes synthesized from SSR require higher sintering temperature and longer sintering times due to the slow rate of solid-state diffusion.[2,11] However, SSR is easily scalable and useful for synthesizing large batches of perovskite material that is required for fabricating tubular membranes by slip-casting. The scalability of SSR is a major advantage over solution-based methods, which typically require substantial quantities of solvent per unit gram of perovskite powder resulting in large liquid waste. Details of the materials used in synthesizing of the tubular membranes are provided in Table 2.2. Figure 2.2 illustrates the process used in slip-casting the precursor tubes.

2.2.3.1 Preparation of plaster molds

Plaster molds were prepared by mixing gypsum powder and water in a 1:1 weight ratio. The plaster slurry was immediately poured in a cylindrical container then degassed under vacuum for 5 minutes to reduce air bubbles. After degassing, a glass test tube (16 mm OD) was carefully inserted vertically at the center of the slurry (~10 cm deep) avoiding contact with the bottom of the container. The slurry was left to solidify for a few minutes and then the test tube was carefully removed, creating a cylindrical hollow in the mold. The plaster mold was subsequently removed from the container and dried at 50°C for 72 hours.

2.2.3.2 Preparation of slip-casting slurry

The slurry (slip) for slip-casting was prepared by ball milling stoichiometric amounts of BCG precursor powders (e.g., 30 g of $BaCO_3$, 21 g of CeO_2 and 11 g of Gd_2O_3) in ethanol for 24 h using YSZ balls as the grinding media. After ball milling, the solution was dried under constant stirring. In a separate beaker, a measured amount of Gum Arabic (as binder) was dissolved in deionized water under continuous stirring at room temperature. The ball-milled precursor powder was added to the Gum Arabic solution and stirred for ~ 10 minutes. The weight ratio of binder: precursor powder: water used was 1:9:45. This specific ratio was determined by systematically tuning the quantities of each component until an effective slip-casting procedure was developed. CuO (0.82 g per 100 g of BCG precursor) was also added to the slurry as a sintering additive to help reduce the temperature required for densifying the BCG tubes. The sintering additive creates lower-melting phases and increases the concentration of electronic defects in the system, which promotes cation diffusion and mass transport, leading to densification at lower temperatures.[14,15] Note that CuO was measured in an amount required to achieve 4 mol% Cu in BCG.

2.2.3.3 Slip-casting of tubular precursors

To slip-cast the tubes, the slurry was poured into the dry plaster mold, which absorbs water leaving behind a solid layer of precursor powder on the wall. The slurry was poured in continuously ensuring that the top surface of the slurry in the plaster mold is kept at a constant level. After casting for one minute, the excess slurry was emptied. This process was repeated five times using the same plaster mold such that the total casting time was five minutes. The multiple casting layer approach helps to prevent the formation of continuous holes in the casted tubes by any bubbles present. After slip-casting, the mold was wrapped in parafilm and allowed to dry

slowly at room temperature. The solid layer (casted tube) shrank during drying and was carefully removed from the mold.

2.2.3.4 Sintering of tubular precursors

Once removed, the casted tubes (~14 mm ID, 16 mm OD and 10 cm in length) were carefully transferred to a YSZ plate within a furnace with the open-end of the tubes facing downwards. A thick layer of YSZ powder was placed underneath the open-end of the tubes to minimize stress. Alumina tubes (open both ends, 24 mm ID) were also placed over the casted tubes in the furnace to prevent them from falling over during sintering. The casted tubes were sintered at 1450°C for 5 hours using ramp rates of 1°C/min. After sintering, the open-end of the tubes were slightly deformed due to compressive stress and reaction with the YSZ powder on the sintering plate. Therefore, they were polished using 240 grit silica carbide paper until even. The dried casted tubes weighed ~ 12 g before sintering and ~ 10 g after sintering. The polished sintered tubes have ~10 mm ID, 11 mm OD and 6 cm length. The linear shrinkage of the tubes upon sintering was ~ 40%. Prior to testing, the tubular membranes were thoroughly cleaned by rinsing and sonicating in ethanol. Note that the sintering temperature mentioned above (1450°C) is ~ 200 °C less than that required for the BCG button membranes reported in Section 2.2.2 due to presence of the sintering additive. In the absence of a sintering additive, the BCG precursor tubes did not fully densify even after sintering at 1650°C for 5 hours using ramp rates of 1°C/min. Moreover, the higher sintering temperature promoted undesired chemical reactions between the tubes and the YSZ powder/support plate and created additional thermal stress that caused the tubes to crack.

In the synthesis described above, the SSR (where BCG perovskite phase is formed from the carbonate and oxide precursors) and sintering (densification) is achieved in a single high temperature step. In other words, the BCG perovskite phase is formed simultaneously during the

sintering process. The combination of both steps (SSR and sintering) with the aid of a metal oxide sintering additive is referred to as solid state reactive sintering (SSRS) and is technique that was recently developed as a simplified approach for the synthesis of barium cerate/zirconate perovskite membranes.[16,17]

2.2.3.5 Coating of tubular membranes with catalyst

A layer of BCG catalyst was coated on the inner surface of some of the tubular membranes. The coating layer was prepared by mixing BCG powder, graphite and binder (6wt% ethyl cellulose in terpineol) in ethanol to form a slurry. The BCG powder was prepared by SSR and sifted to < 75 μm size prior to use. The weight ratio of the binder: graphite: BCG powder: ethanol in the slurry was 4:7:21:80. The prepared slurry was sonicated for about 10 minutes to break up any agglomerates and then poured into the inner surface of the tubular membrane. After ~5 s, the slurry was emptied then the tubular membrane was dried at 70°C for 10 minutes. The coating process was repeated 10 times to increase the thickness of the coated layer. To minimize contamination, the outer surface of the tubular membrane was wrapped in Teflon tape before the coating process. After drying the final coating layer, the coated membranes were calcined at 900°C for 2 h (ramp rate 1.5°C/min) to burn off graphite and create a porous catalyst layer attached to the membrane.

Table 2.2. Materials used in the synthesis of tubular membranes

Chemical	Manufacturer or Vendor	Purity Level
Barium carbonate ($BaCO_3$) 1µm powder	Alfa Aesar	99.8%
Cerium (IV) oxide (CeO_2) 5 µm powder	Alfa Aesar	99.9%
Gadolinium (III) oxide (Gd_2O_3) <10 µm powder	Alfa Aesar	99.9%
Copper (II) oxide (CuO) <10 µm powder	Sigma Aldrich	98%
Gum Arabic	The Ceramic Shop	Not specified
Activa Art Plaster (Gypsum Powder)	Blick Art Materials	Not specified
Alpha-Terpineol	Acros Organics	97+%
Ethyl cellulose	Sigma Aldrich	48% ethoxyl
Graphite	Alfa Aesar	≥ 99%

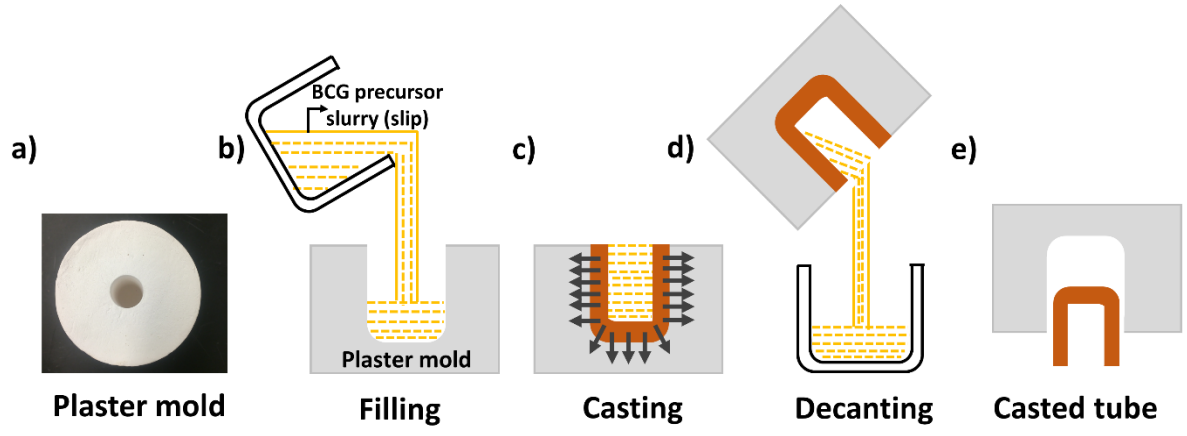

Figure 2.2. Five consecutive steps involved in slip casting precursor tubes: (a) a plaster mold is prepared from a mixture of gypsum plaster and water; (b) the dry mold is filled with slurry composed of chemical precursors and water; (c) the mold extracts water from the slurry forming a solid layer of precursor on the wall of the mold; (d) excess slip is decanted from the mold; (e) solid layer or casted tube is removed from mold after partial drying.

2.3 Experimental Set-ups

2.3.1 Packed bed reactor set-up

Figure 2.3 shows a schematic of the set-up used for the OCM packed bed reactor experiments. The catalyst powder was placed in the center of a quartz tube (6.35 mm ID and 9.5 mm OD) and supported on both sides with quartz wool. The quartz tube was oriented horizontally in an insulated furnace and a thermocouple was located near the catalyst bed. The reactor was heated to 750°C in a flow of Argon that was discontinued when the reactant gases were introduced. Methane (containing 5% He) and air were fed through separate mass flow controllers (Cole-Parmer) and were mixed before entering one end of quartz tube. The effluent gases pass through a condenser to remove any water vapor formed during the reaction before entering a Gas Chromatograph (GC) for compositional analysis.

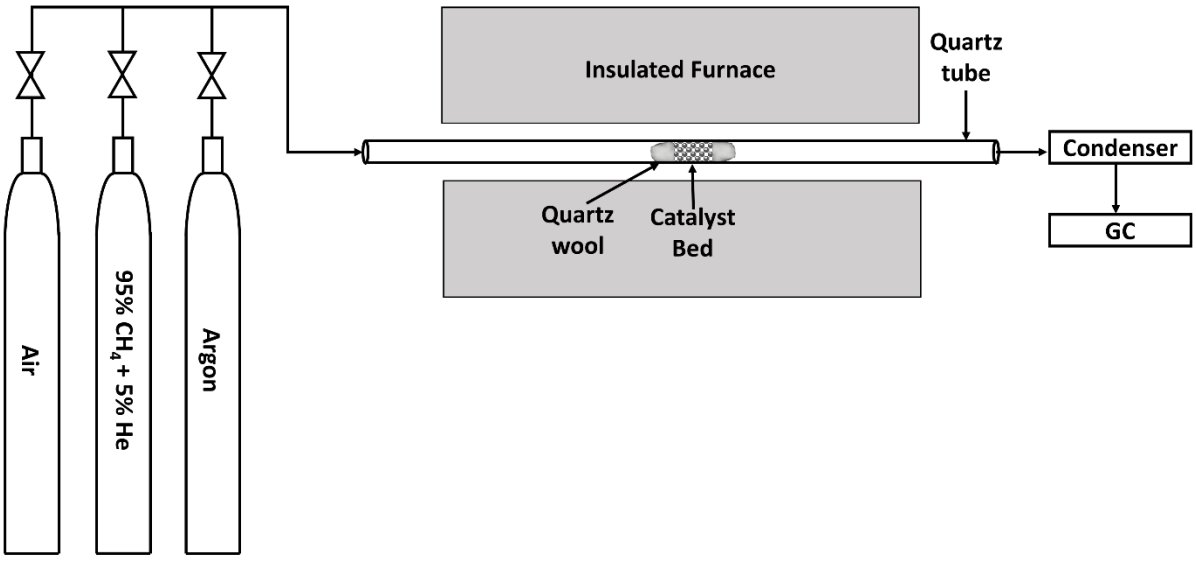

Figure 2.3. Packed bed reactor set-up for OCM

2.3.2 Button membrane reactor set-up

A diagram of the button membrane reactor set-up is shown in Figure 2.4. The reactor was housed in an insulated furnace. The button membrane was attached to the top of an alumina tube (12.7 mm OD and 9.5 mm ID) using glass and ceramic sealants (Aremco-Seal 617, Mo-Sci GL1729P/-45 and Ceramabond 552). The sealants were applied one layer after another (in the order mentioned above), dried after each layer, then cured by heating in the furnace to 880°C in helium flow. The reactor was then cooled down to desired reaction temperature. In the OCM experiments, a mixture of O_2 and N_2 (or air) was fed from the top through a quartz tube (19 mm OD and 17 mm ID) to the membrane region. Methane and helium flow upwards through a smaller inner quartz tube (6.35 mm OD and 4 mm ID) to the catalyst-coated side of the membrane where the reaction occurs with permeated oxygen. The effluent gases from the methane side flow down the annular region between the alumina tube and the inner quartz tube to a GC for analysis.

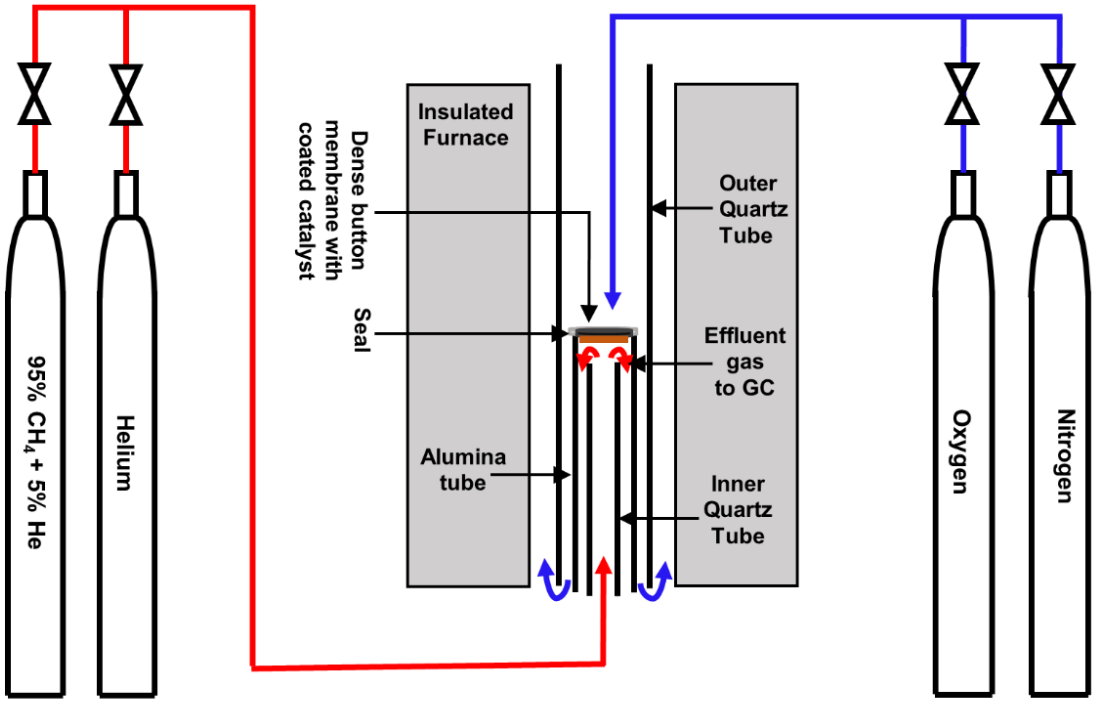

Figure 2.4. Button membrane reactor set-up. Note that air was sometimes used in place of a mixture of oxygen and nitrogen

2.3.3 Tubular membrane reactor set-up

The tubular membranes were tested in the membrane reactor set-up shown in Figure 2.5a. This set-up is very similar to that of the button membranes. The open-end of the tubular membrane was sealed to the top of an alumina tube (12.7 mm OD and 9.5 mm ID) using glass and ceramic sealants. Methane and helium were introduced through an inner quartz tube (6.35 mm OD and 4 mm ID) that extends towards the dead-end of the tubular membrane. A mixture of O_2 and N_2 was fed from the top through a larger quartz tube (19 mm OD and 17 mm ID) to the membrane region. The effluent gas containing products formed from the reaction between methane and permeated oxygen is sent to a GC for analysis. The tubular membranes were also tested in a "co-fed reactor" configuration where CH_4 is co-fed with O_2 on one side of the membrane while pure N_2 is fed on

the opposite side as shown in Figure 2.5b**.** This configuration was used to evaluate the effect of changing the mode of feeding oxygen (distributed vs co-fed) on the OCM performance when all other conditions are kept the same as the membrane reactor. This approach allowed us to test our overall hypothesis of the improved performance of a membrane reactor over a conventional co-fed reactor.

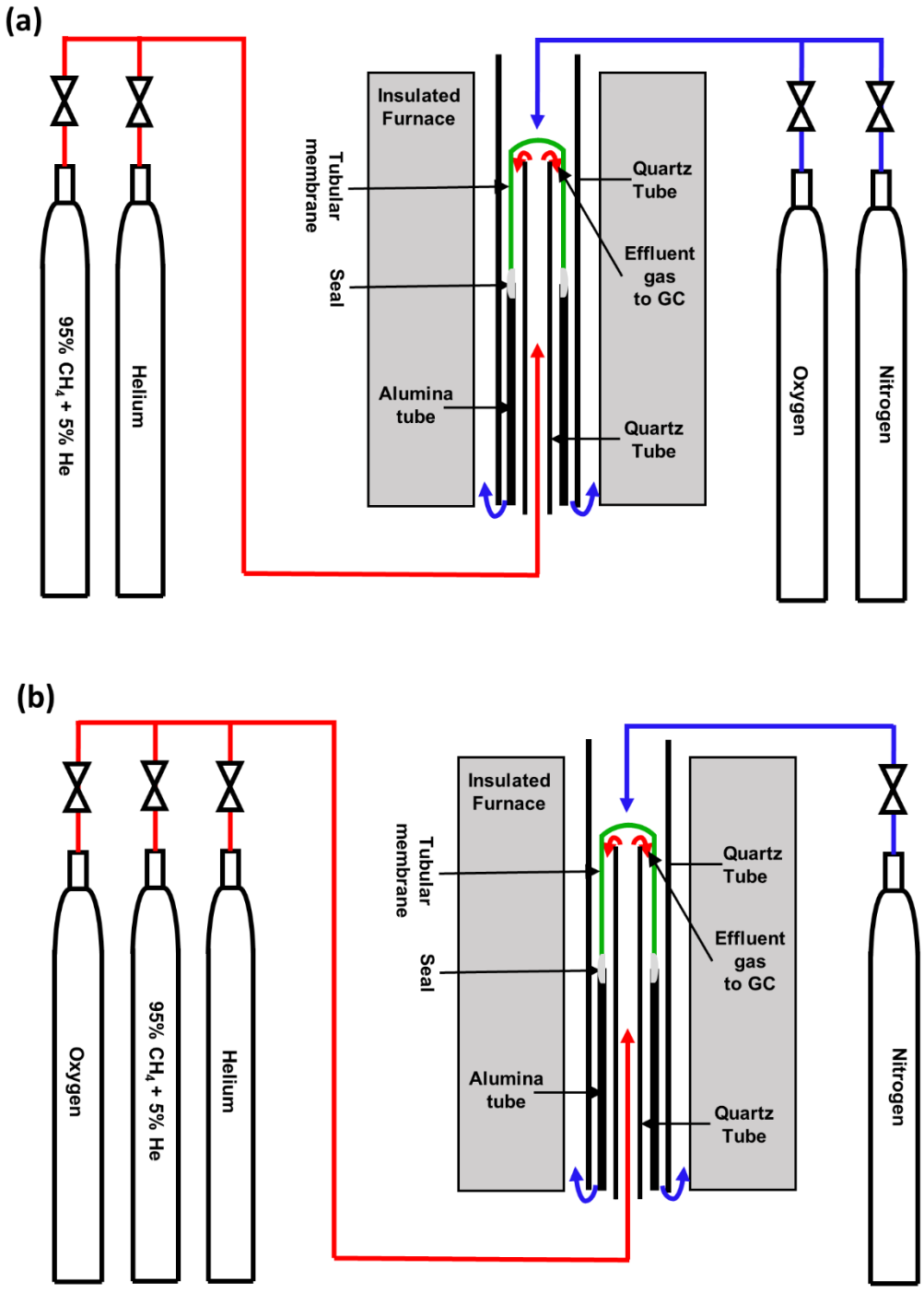

Figure 2.5. Tubular membrane experimental set-up (a) membrane reactor configuration (b) co-fed reactor configuration.

2.4 Characterization Techniques

Several characterization techniques were used in this dissertation work. In this section, a general description of each characterization technique is provided along with specific descriptions of the equipment and conditions employed this work.

2.4.1 X-ray diffraction

X-ray diffraction (XRD) is a technique used for analyzing the structure of crystalline materials. It is primarily a bulk-sensitive technique because it has a large penetration depth (~1 – 500 μm) into the material.[18] XRD utilizes two key properties of X-ray electromagnetic radiation: (i) An X-ray travels in a straight line with speed c, (ii) An X-ray interferes with itself and with objects on the order of its wavelength. Since X-rays have wavelength (0.01 – 100 Å) of similar dimensions as the inter-atomic spacing in crystalline materials (0.5 – 2.5 Å), they can interfere these materials.[18]

In XRD, a beam of X-ray photons generated from a source is directed towards a sample. The incident X-ray beam can be treated as a wave with an oscillating electric field. When the X-ray hits the sample at an angle (θ), the waves are scattered by the sample. In other words, the electrons surrounding the atoms in the sample start to oscillate about a mean position, emitting an electromagnetic wave that interacts with the oscillating electric field of the X-ray wave.[18] The scattered waves can either undergo constructive or destructive interference depending on how the waves overlap with each other.[18] In most directions, the waves are out of phase with each other and destructive interference (incoherent scattering) occurs resulting in lower scattered intensity. However, in a few directions, the waves will move in phase and reinforce each other resulting in greater scatter intensity. This is termed constructive interference (coherent scattering). For an

idealized sample consisting of parallel plane of atoms separated by a distance d, constructive interference is achieved when Bragg's Law (Equation 2.1) is satisfied.[18]

$$n\lambda = 2d \sin\theta \tag{2.1}$$

Where n is an integer, d is the interatomic spacing, θ is the incident angle and λ is the wavelength of the X-ray beam. The angle between the incoming and outgoing beam directions is called the scattering or diffraction angle (2θ). Prior to hitting the sample, the X-ray beam is typically filtered to produce monochromatic (single wavelength) radiation.

The XRD measurements in this work was obtained using a Rigaku MiniFlex 600 spectrometer, equipped with JADE software for phase identification and data processing. The device utilized a Cu Kα radiation source with wavelength (λ) =1.54059 Å and was operated at a tube voltage and current of 40kV and 15mA, respectively. The sample (typically in powder form) was loaded onto a sample holder and inserted into the device chamber, where it was continuously scanned through a range of 2θ angles at a speed of 2°(2Θ) per minute and a step size of 0.02°. The detector records the X-ray scattering intensity at each 2θ angle and a plot of the scattering intensity as a function of 2θ is obtained in the XRD spectrum. The relative peak positions obtained in the spectrum is a function of the d-spacing (determined by the crystal structure), while the peak width is related to the mean crystallite size with smaller crystals resulting in more peak broadening.[18]

2.4.2 Scanning electron microscopy

Scanning electron microscopy (SEM) is a technique used to obtain magnified images of samples. The images obtained give information on the dimensions, topography, morphology and composition of the samples. In this technique, a beam of electrons emitted from an electron source (e.g., tungsten filament) are accelerated to high energy (E_0 = 0.1 to 30 keV). The high energy beam is then finely focused on the sample by passing it through a series of apertures, lenses, and

electromagnetic coils. The focused beam is scanned by the coils in a rectangular raster (x-y) pattern such that it is placed sequentially at neighboring but distinct positions on the sample. At each distinct position, the interaction between the electron beam and the sample produces secondary and back-scattered electrons.

The secondary electrons are electrons ejected from atoms at the surface of the sample after interaction with the electron beam, while the back-scattered electrons are beam electrons (i.e., not ejected from sample atoms) that retain a large fraction of incident energy after interacting with the electric fields of atoms in the sample. The intensities of the secondary and back-scattered electron signals are measured using respective detectors, digitized and stored in a computer memory. The stored signals are then used to determine relative brightness levels in the resulting gray-scale image which is displayed on the computer screen. Compared to secondary electrons, images obtained from back scattered electrons give significant contrast between elements of different atomic numbers, and therefore give information on the composition of the sample. Images obtained from the lower energy (0 - 50 eV) secondary electrons give information on the topography of the sample.[19]

To prevent attenuation of the electrons (both incoming beam electrons and the emitted electrons) by the atoms and molecules in atmospheric gases, the conventional SEM sample chamber and electron-optical column are maintained under high-vacuum conditions ($< 10^{-4}$ Pa). Furthermore, non-conductive samples will accumulate charges when impacted by the high-electron beam in a conventional SEM, which results in bad image quality. To prevent charge accumulation, such samples need a pathway for electrical discharge that is well grounded. This is commonly achieved by coating the samples with a conductive layer such as gold or carbon.[19]

In this dissertation work, secondary electron SEM images of samples were obtained using a Tescan MIRA3 FEG microscope, which has spatial resolution < 10 nm. The device was equipped with an EDAX detector that can be used for Energy Dispersive X-ray Spectroscopy (EDS) measurements as described in the following section. Samples were typically sputter coated with a thin gold layer to minimize charging during image collection. The images were collected at accelerating voltages ≤12 keV and working distances ≤ 15 mm.

2.4.3 Energy dispersive x-ray Spectroscopy

Energy dispersive x-ray spectroscopy (EDS) is a technique used for the identification and quantification of elements present in a sample. It is typically used in conjunction with an electron microscope (e.g., SEM) to determine the elemental composition of the imaged sample. In EDS, a beam electron (at energy E_0) incident on a sample, ejects an electron in the inner (core) shell of an atom in the sample leaving the atom in an excited (ionized) state. In this process, the incident beam electron loses energy (E) which is transferred to the ejected electron. The ejected electron goes to an empty energy level or vacuum leaving behind a hole that is then filled with an electron from an outer (higher energy) shell. As the outer electron relaxes to fill the hole, it releases a characteristic X-ray photon which has energy equivalent to the difference in energy in the outer shell and the core shell.[20,21] The characteristic X-ray emitted is specific for each element and can be used for elemental analysis. Figure 2.6 illustrates the EDS process using a simple Bohr model of an atom.

To ionize an atom, the incoming beam electron must have enough energy that exceeds the binding energy of the specific inner shell electrons (i.e., the energy of the characteristic X-rays). Therefore, the accelerating voltage of the beam must be selected such it exceeds (by about 1.5 – 3 times) the minimum specific energy required to excite the inner electron, known as the absorption edge energy or critical excitation potential.[20] In addition to the characteristic X-rays, continuum

(Bremsstrahlung) X-rays are also emitted due to interaction of beam electrons with the atomic nucleus. However, these X-rays occur at a wide range of energies and have relatively weaker intensities; thus, they show up as background in the EDS spectrum.

The nomenclature of the characteristic X-ray emitted is dependent on the relative positions of the outer and inner electrons. For example, if an electron from an L or M shell drops to fill a hole in the K-shell, it emits a Kα and Kβ X-radiation, respectively. Likewise, if the electron transfer is from an M-shell to an L-shell, Lα radiation is emitted etc.[20,21] EDS can be used for spot analysis, line scan analysis or elemental mapping. In spot analysis the beam is focused on one or consecutive spots in a sample to obtain local information on sample composition. In line scan analysis, the beam follows a straight line drawn on the sample and a spectrum showing the relative amounts of various identified elements along that line is obtained. Elemental maps are obtained over a rectangular scanned image area and show the distribution and relative amounts of identified elements over the scanned area. The EDS detector is typically semi-conductor based and can detect X-ray photons from a threshold of approximately 40 eV to E_0 as high as 30 keV.[19] The lightest element that can be analyzed in most conventional SEM/EDS is Be as Li emits characteristic X-rays that are too low in energy, and H and He do not emit X-rays.

The EDS measurements reported in the dissertation were obtained using an EDAX Octane Plus EDS unit, which was connected to the Tescan Mira FEG SEM machine. The device was equipped with TEAM software for data collection and analysis. The working distance was fixed at a specified optimal of 15 mm and the accelerating voltage for each measurement was selected to be at least 1.5 times the maximum absorption edge energy of elements to be detected in the sample. Elemental maps were obtained at a resolution (matrix size) of 256 x 200 pixels and dwell

time of 200 µs. A drift corrected mode was used during mapping to minimize effect of sample drifting.

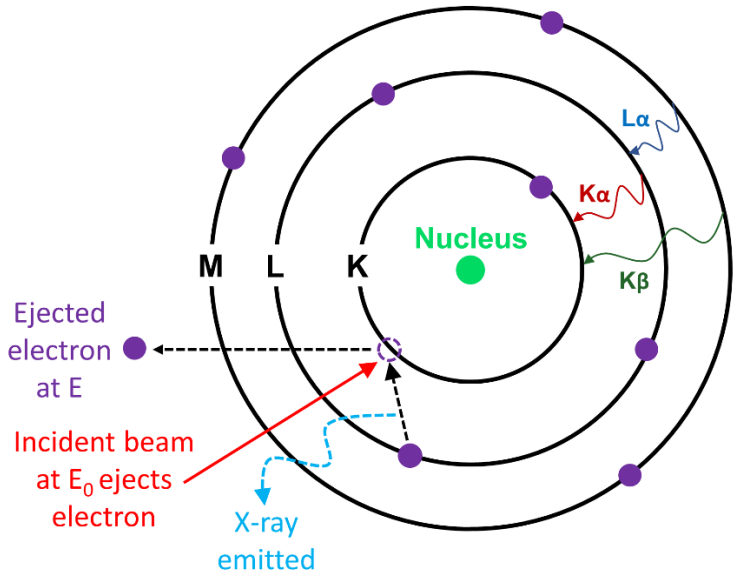

Figure 2.6. Schematic of EDS process using a simple Bohr model of an atom

2.4.4 Wavelength dispersive spectroscopy

Wavelength dispersive spectroscopy (WDS) was used to determine the composition of some samples in this dissertation work. In WDS, a sample is bombarded by a beam of electrons which leads to the generation of characteristics X-rays. A fraction of the emitted X-rays is directed to an analyzing crystal with a specific lattice spacing (d). The X-rays hit the crystal at an incident angle (θ) and are strongly diffracted by the crystal if the wavelengths satisfy Bragg's law (Equation 2.1). The diffracted X-rays leave the crystal at an angle 2θ relative to the incident X-ray beam and are focused such that a single wavelength is sent to a detector. The detector collects and counts the X-rays at that wavelength, processes them and generates an output signal that represents the X-ray intensity at the specific wavelength.[22]

Only a single wavelength (and therefore a single element in a sample) can be analyzed by the detector at a given time. To analyze the wavelength from a different element in the sample, the incident angle (θ) of the X-rays on the analyzing crystal must be changed. In original WDS spectrometers, the incident angle (θ) of the X-rays on the analyzing crystal is modified by moving the crystal along an arc (known as a Rowland circle) relative to the sample, such that different wavelengths are selected for detection and analysis. Since the diffracted X-rays leave at a 2θ angle, the detector in the Rowland circle must also be rotated at twice the angular speed of the analyzing crystal to ensure that the diffracted beam hits the center of the detector. Only a limited range of wavelengths can be achieved from a single analyzing crystal, therefore multiple crystals with different lattice (d) spacings are typically applied to allow the analysis of a wide range of elemental wavelengths. Multiple detectors are normally included in the WDS unit such that the wavelengths of the different elements' samples can be analyzed simultaneously.[22,23]

WDS is typically performed in a specialized Electron Probe Microanalyzer (EPMA) unit, although it is sometimes integrated into a microscopy (e.g., SEM) device. For accurate estimation of sample composition, the samples should ideally be flat and well-polished to ensure uniform emission of X-rays. The analysis system must also be calibrated with standards of known composition as the X-ray intensities are corrected for matrix effects (e.g., atomic-number, absorption and fluorescence excitation effects) by a computer program which compares the raw intensities to that of the known standards.[23] The main advantages of WDS over EDS for sample composition analysis include lower detection limits, higher spectral resolution and better accuracy. The detection limit for WDS is ~ 100 ppm, while that of EDS is ~ 1000 ppm.[20] WDS signals also have narrower peak widths (~ 5 – 20 eV) and therefore lower peak interference compared to EDS

signals, which have spectral resolution of ~ 100 - 200 eV. However, WDS requires a longer data acquisition compared to EDS.[21–23]

In this work, WDS measurement were obtained using a Cameca SX100 EPMA. A focused electron beam with an accelerating voltage of 15 keV and a beam current of 20 nA was used for the measurements. Standard samples were used for calibration and the raw intensities were corrected using the X-PHI intensity correction method.[24]

2.4.5 Raman spectroscopy

Raman spectroscopy is a technique that can be used to identify the molecules or bonding present in a sample based on the energy of the vibrational modes detected. In Raman spectroscopy, monochromatic light (laser) irradiated on a sample is scattered by molecules in the sample. Most of the scattered photons have same frequency as the incoming photons (Rayleigh scattered) while a minor amount of the scattered photons have different frequency (Raman scattered). The Raman scattered light detected with a lower frequency (lower energy) than Rayleigh scattered light is referred to as Stokes radiation, while that detected at higher frequency (higher energy) is referred to as anti-Stokes radiation. In other words, Rayleigh scattering leaves the molecule in its original vibrational state, while Stokes and anti-Stokes scattering leaves the molecule in a higher and lower energy vibrational state, respectively.[25]

Stokes lines typically arise from molecules initially in their ground vibrational state, while anti-Stokes originate from molecules initially in a vibrational excited state. Since most molecules are found in the ground state at ambient conditions, Stokes lines have much higher intensity than anti-Stokes and are used for analysis. The frequency difference between the vibrational state of the incident light and final vibrational state of the scattered light is known as the "Raman shift" (in units of wavenumbers, cm^{-1}) and is calculated using Equation 2.2, where λ_i and λ_s is the wavelength

(in nm) of the incident and scattered light, respectively. The Raman spectrum of a sample plots the intensity of the scattered light as a function of the Raman shift. The spectrum is plotted with reference to the incident laser wavelength such that the Rayleigh band lies at 0 cm^{-1}.[25]

$$Raman\ shift\ (cm^{-1}) = 10^7\ (\frac{1}{\lambda_i} - \frac{1}{\lambda_s}) \tag{2.2}$$

In this dissertation work, Raman spectrum of samples were obtained at ambient conditions using a Horiba LabRAM HR system. The spectra were collected at constant laser power using a 532 nm green excitation laser (at 50% intensity).

2.4.6 Nitrogen physisorption

Nitrogen physisorption was used to estimate the surface area of catalyst powders. This technique estimates the surface area of the powders from the monolayer volume of adsorbed N_2 (V_m), which is calculated from a relationship between the amount of nitrogen adsorbed and its pressure. The most prevalent method used as an approximation for this relationship is based on the Brunauer–Emmett–Teller (BET) gas adsorption theory[26,27] and is given in Equation 2.3, where V is the volume of adsorbed N_2 gas, V_m is the monolayer volume of adsorbed N_2 gas, P/P_0 is the relative pressure, and ${}^{C}BET$ is the BET constant.[27]

$$\frac{P/P_0}{V(1 - P/P_0)} = \frac{1}{V_m \cdot {}^{C}BET} + \frac{P/P_0 \cdot ({}^{C}BET - 1)}{V_m \cdot {}^{C}BET} \tag{2.3}$$

The BET surface areas of the catalyst powders in this work were obtained using a Micrometrics 3-Flex Surface Characterization Analyzer. To begin the process, the catalyst powders (~1g) were loaded onto pre-weighed glass tubes and degassed under vacuum at 698 K for 4 hours. The degassing step is necessary to remove any contaminants (e.g., moisture, organics) from the catalyst, which improves the accuracy of the N_2 adsorption measurement. After

degassing, the glass tubes were weighed together with the sample and the total mass recorded. The "dry" weight of the degassed samples, obtained by subtracting the weight of each empty glass tube from the total weight of glass tube with degassed sample, was inputted into the BET analysis software. The degassed samples in the glass tubes were loaded into the 3-Flex Analyzer. Nitrogen gas was introduced into the system and the adsorption process was initiated by inserting the tubes into a Dewar containing liquid nitrogen at boiling point (77K), since N_2 physisorption is a weak process at room temperature. During the run, the relative pressure (P/P_0) of nitrogen gas in the glass tubes is tuned and the amount of nitrogen adsorbed by the samples at each relative pressure is recorded. The software generates a straight-line plot of $\frac{P/P_0}{V(1-P/P_0)}$ vs $\frac{P}{P_0}$ known as the BET surface area plot and uses the slope and intercept of this plot to calculate V_m, from which the BET surface area is derived.[27]

2.4.7 Temperature programmed reduction

Temperature programmed reduction (TPR) is a technique used to evaluate the reducibility of solid materials. In this technique, the solid material is exposed to a reducing gas (e.g., hydrogen) while the temperature of the system is increased at a specific ramp rate. The concentration of the gaseous effluent from the system is measure and recorded and used to generate a reduction profile. When hydrogen is used as the reducing gas on a solid oxide material, the reduction profile can either be a plot of the H_2 consumed or H_2O produced as a function of temperature. Each peak observed in the reduction profile indicates the occurrence of a distinct reduction process in the material and the temperature at which the peak occurs is called the reduction temperature. In general, the lower the reduction temperature, the more reducible the material is. The area under the peak also indicates the concentration of a component (e.g., oxygen) present in the solid material.[28]

In this work, H_2-TPR experiments were conducted using a Micrometrics Autochem II 2920 equipped with a mass spectrometer. 500 mg of catalyst powder was loaded into a U-shaped quartz tube and pretreated at 200°C for 30 minutes under helium flow. After cooling down to 30°C, the temperature was ramped up to 1000°C at 10°C/min under 5% H_2 in Argon stream at a flow rate of 50 L/min. The mass spectrometer records the signal for H_2O, which is used to generate the reduction profiles.

2.4.8 Gas chromatography

Gas chromatography (GC) is a technique used for the identification and quantification of molecules in a gaseous stream. A gas chromatograph utilizes a stationary phase, a mobile phase, a sample introduction device, columns and detectors. The stationary phase is located on the inside of the column and can be a solid or a liquid (e.g., a highly viscous polymer with negligible vapor pressure) coated on a solid support. The mobile phase is typically an inert carrier gas such as helium, argon or nitrogen.[29] In a typical GC run, a gaseous sample is injected alongside a carrier gas through an appropriate sample introduction device. The sample is sent through one or multiple columns where the molecules in the stream are separated based on differences in the interaction of the molecules with the mobile phase and the stationary phase. Specific properties of the molecules such as vapor pressure, size, etc., causes the differences in these interactions. After passing through the column, the separated sample in the carrier gas is sent to a detector. The detector outputs the signal which is sent to a data analysis software on a computer that produces a spectrum (chromatogram) and provides additional information such as height, width and areas of the resolved peaks in the chromatogram.[29]

Two types of GC detectors were used in this dissertation work; a thermal conductivity detector (TCD) and a flame ionization detector (FID). The TCD is a non-destructive concentration-

sensitive detector that uses a Wheatstone bridge circuit to detect changes in the thermal conductivity of the column effluent in comparison to a reference carrier gas. In a basic circuit with two filaments, the column effluent gas flows over one filament while a reference gas (e.g., carrier gas) flows over a second filament. The carrier gases used typically have much higher thermal conductivity than the analytes. This means that the carrier gas can remove heat from the filament much faster than the analytes.[30] Therefore, the temperature of the filament in contact the effluent gas will become higher than the reference filament. The measured increase in temperature of the effluent filament (relative to the reference filament) is thus proportional to the thermal conductivity of the solutes in the effluent (relative to the carrier gas), as well as the concentration of the solutes.[29,30] The FID is a destructive mass-sensitive detector which operates by combusting the column effluent gases in a flame produced from hydrogen/air mixture. The combustion process produces positively charged intermediate species (primarily CHO^+) that are collected in a negatively biased electrode. This process generates current which creates an electrical signal.[30] The current produced is directly proportional to the mass of carbon atoms passing through the detector per unit time and is independent of the molecule structure.[29,30]

Two different GCs were used in this dissertation work; a Varian CP-3800 and an Agilent 7890B. The Varian CP-3800 GC was used in the work reported in Chapter 3, while the more modern Agilent 7890B GC was used in the work reported in Chapters 4 and 5. The Agilent 7890B was acquired as a replacement for the Varian CP-3800 and both GCs had similar configurations. The GCs were equipped with several multiple port valves, sample loops, columns, two TCDS and one FID detector. One TCD, using helium as the carrier gas, detects O_2, N_2, CO, CO_2 and low molecular weight hydrocarbons (CH_4, C_2H_4, C_2H_6 and C_{3s}). An auxiliary TCD detector, using argon as the carrier gas, was specifically used for detecting H_2 and He. The FID detector detects

all gaseous hydrocarbons present in the sample. The GCs were calibrated (using certified gas mixtures) before the experiments to obtain linear calibration curves that relate component concentrations to the peak areas obtained from the chromatograms.

2.5 References

(1) Agarwal, V.; Liu, M. Preparation of Barium Cerate-Based Thin Films Using a Modified Pechini Process. *J. Mater. Sci.* **1997**, *32* (3), 619–625.

(2) Carneiro, J. S.; Williams, J.; Gryko, A.; Herrera, L. P.; Nikolla, E. Embracing Complexity of Catalytic Structures: A Viewpoint on Synthesis of Non-Stoichiometric Mixed Metal Oxides for Catalysis. *ACS Catal.* **2020**, *10*, 516–527.

(3) E. Danks, A.; R. Hall, S.; Schnepp, Z. The Evolution of "sol–gel" Chemistry as a Technique for Materials Synthesis. *Mater. Horiz.* **2016**, *3* (2), 91–112.

(4) Esposito, S. "Traditional" Sol-Gel Chemistry as a Powerful Tool for the Preparation of Supported Metal and Metal Oxide Catalysts. *Materials* **2019**, *12* (4), 668.

(5) Farrell, B. L.; Linic, S. Oxidative Coupling of Methane over Mixed Oxide Catalysts Designed for Solid Oxide Membrane Reactors. *Catal. Sci. Technol.* **2016**, *6*, 4370–4376.

(6) Ishihara, T.; Ishikawa, S.; Hosoi, K.; Nishiguchi, H.; Takita, Y. Oxide Ionic and Electronic Conduction in Ni-Doped $LaGaO_3$-Based Oxide. *Solid State Ion.* **2004**, *175* (1), 319–322.

(7) Ricote, S.; Bonanos, N. Enhanced Sintering and Conductivity Study of Cobalt or Nickel Doped Solid Solution of Barium Cerate and Zirconate. *Solid State Ion.* **2010**, *181* (15), 694–700.

(8) VahidMohammadi, A.; Cheng, Z. Fundamentals of Synthesis, Sintering Issues, and Chemical Stability of $BaZr_{0.1}Ce_{0.7}Y_{0.1}Yb_{0.1}O_{3-\delta}$ Proton Conducting Electrolyte for SOFCs. *J. Electrochem. Soc.* **2015**, *162* (8), F803–F811.

(9) Zhang, Y.; Zeng, F.; Yu, C.; Wu, C.; Ding, W.; Lu, X. Fabrication and Characterization of Dense $BaCo_{0.7}Fe_{0.2}Nb_{0.1}O_{3-\delta}$ Tubular Membrane by Slip Casting Techniques. *Ceram. Int.* **2015**, *41* (1), 1401–1411.

(10) Choi, M.-B.; Lim, D.-K.; Jeon, S.-Y.; Kim, H.-S.; Song, S.-J. Oxygen Permeation Properties of BSCF5582 Tubular Membrane Fabricated by the Slip Casting Method. *Ceram. Int.* **2012**, *38* (3), 1867–1872.

(11) Athayde, D. D.; Souza, D. F.; Silva, A. M. A.; Vasconcelos, D.; Nunes, E. H. M.; Diniz da Costa, J. C.; Vasconcelos, W. L. Review of Perovskite Ceramic Synthesis and Membrane Preparation Methods. *Ceram. Int.* **2016**, *42* (6), 6555–6571.

(12) Agarwal, V.; Liu, M. Preparation of BaCe03-Based Electrolyte Films. In *Proceedings of the First International Symposium on Ceramic Membranes*; The Electrochemical Society, 1997; Vol. 95, p 177.

(13) Venkatasubramanian, A.; Gopalan, P.; Prasanna, T. R. S. Synthesis and Characterization of Electrolytes Based on $BaO–CeO_2–GdO_{1.5}$ System for Intermediate Temperature Solid Oxide Fuel Cells. *Int. J. Hydrog. Energy* **2010**, *35* (10), 4597–4605.

(14) Medvedev, D. A.; Murashkina, A. A.; Demin, A. K. Formation of Dense Electrolytes Based on $BaCeO_3$ and $BaZrO_3$ for Application in Solid Oxide Fuel Cells: The Role of Solid-State Reactive Sintering. *Rev. J. Chem.* **2015**, *5* (3), 193–214.

(15) Nikodemski, S.; Tong, J.; O'Hayre, R. Solid-State Reactive Sintering Mechanism for Proton Conducting Ceramics. *Solid State Ion.* **2013**, *253*, 201–210.

(16) Tong, J.; Clark, D.; Bernau, L.; Subramaniyan, A.; O'Hayre, R. Proton-Conducting Yttrium-Doped Barium Cerate Ceramics Synthesized by a Cost-Effective Solid-State Reactive Sintering Method. *Solid State Ion.* **2010**, *181* (33), 1486–1498.

(17) Babilo, P.; Haile, S. M. Enhanced Sintering of Yttrium-Doped Barium Zirconate by Addition of ZnO. *J. Am. Ceram. Soc.* **2005**, *88* (9), 2362–2368.

(18) Lee, M. *X-Ray Diffraction for Materials Research: From Fundamentals to Applications*; Apple Academic Press, 2017.

(19) Goldstein, J. I.; Newbury, D. E.; Michael, J. R.; Ritchie, N. W.; Scott, J. H. J.; Joy, D. C. *Scanning Electron Microscopy and X-Ray Microanalysis*; Springer, 2017.

(20) Friel, J. J. *X-Ray and Image Analysis in Electron Microscopy*, Second.; Princeton Gamma-Tech, Incorporated, 2003.

(21) Garratt-Reed, A. J.; Bell, D. C. *Energy Dispersive X-Ray Analysis in the Electron Microscope*; BIOS: S.l., 2003.

(22) Egerton, R. F. *Physical Principles of Electron Microscopy*; Springer, 2005.

(23) Reimer, L. *Scanning Electron Microscopy: Physics of Image Formation and Microanalysis*; Springer, 1998.

(24) Merlet, C. An Accurate Computer Correction Program for Quantitative Electron Probe Microanalysis. *Microchim. Acta* **1994**, *114* (1), 363–376.

(25) Larkin, P. *Infrared and Raman Spectroscopy: Principles and Spectral Interpretation*; Elsevier, 2017.

(26) Brunauer, S.; Emmett, P. H.; Teller, E. Adsorption of Gases in Multimolecular Layers. *J. Am. Chem. Soc.* **1938**, *60* (2), 309–319.

(27) Naderi, M. Surface Area: Brunauer–Emmett–Teller (BET). In *Progress in filtration and separation*; Elsevier, 2015; pp 585–608.

(28) Jones, A. *Tempature-Programmed Reduction for Solid Materials Characterization*; CRC Press, 2014.

(29) Dettmer-Wilde, K.; Engewald, W. *Practical Gas Chromatography*; Springer-Verlag Berlin Heidelberg, 2014.

(30) Poole, C. F. *Gas Chromatography*; Elsevier: New York, 2012.

Chapter 3

In Search of Membrane/Catalyst Materials for Oxidative Coupling of Methane: Performance and Phase Stability Studies of Gadolinium-Doped Barium Cerate and the Impact of Zr Doping

3.1 Summary

Oxidative coupling of methane (OCM) is a promising technology for the direct conversion of methane to ethylene and ethane (C_2). This process is yet to be commercialized due its poor yield reflected in the formation of undesired products such as CO and CO_2 (CO_x) as methane conversion increases, particularly in conventional packed bed reactors (PBRs). It has been argued that by applying O^{2-} conducting membrane reactors that distribute the oxygen feed, the selectivity to the C_2 products can be increased. A practical design for these membrane reactors would include combining a selective catalyst, preferably O^{2-} conducting, with an O^{2-} conducting membrane. In this work, we studied an O^{2-} conducting material, gadolinium-doped barium cerate ($BaCe_{0.8}Gd_{0.2}O_{3-\delta}$ or BCG), to evaluate its potential applicability as a catalyst and membrane in OCM membrane reactors. From PBR tests, we found that this material was active for OCM, and achieved a maximum C_{2+} yield of ~14% at 1023 K. Furthermore, at low oxygen partial pressures expected to occur in membrane reactors, a C_{2+} selectivity of ~90% was obtained at methane conversions of ~3%. Although the C_{2+} yield from this material was stable over 48 hours on stream at high methane conversions, X-ray diffraction data showed that the BCG perovskite phase, which is required for its conductive (membrane) properties, decomposes into $BaCO_3$, CeO_2 and Gd_2O_3

like phases, due to reactions with CO_2. We showed that doping BCG with Zr was effective at suppressing the phase instability in OCM without significantly affecting the C_{2+} yields in a PBR.

3.2 Introduction

Natural gas is an abundant resource with over 500 trillion cubic feet of proven reserves in the US.[1] Its production is projected to increase due to the availability of unconventional sources such as shale gas, and the possibility of harnessing methane hydrates in the long term. [2,3] It is composed mainly of methane which has vast potential as an advantaged feedstock for chemical and fuel production. In general, converting methane directly into chemicals under mild conditions is challenging due to its strong C-H bonds (bond strength ~ 434 kJ/mol). [3–5] Commercially, methane is converted through a high temperature, energy intensive reforming process to syngas (mixture of mainly CO and H_2), which is then used to produce chemicals such as methanol and higher hydrocarbons. This indirect conversion of methane to chemicals via syngas production is only commercially practical when applied on a large scale. Consequently, methane from isolated small-scale sources (e.g., associated gas), that cannot be economically transported, is commonly flared causing the release of greenhouse gases. [3,5] Direct conversion of methane into valuable chemicals can alleviate the need for costly syngas production and is potentially more suitable for valorizing methane released from small scale sources. Therefore, there is significant interest in the development of direct methane conversion routes. [5–7]

A potential route for direct methane conversion is through a process known as the oxidative coupling of methane (OCM) which was first reported in the early 1980s. [8] In OCM, methane is activated at high temperatures (923 – 1173 K) in the presence of oxygen and an active catalyst to produce C_2 hydrocarbons (ethane and ethylene).[9] It has been proposed that during OCM, hydrogen is abstracted from methane to form methyl radicals which couple in the gas phase to form ethane.

[6,10,11] The ethane formed is subsequently dehydrogenated to ethylene through catalytic and gas phase reaction steps.[7,12] Various mixed metal oxide catalysts have been investigated for OCM and some of the best C_2 yields have been achieved on $Mn/Na_2WO_4/SiO_2$ and Li/MgO catalysts.[13,14] Even for these catalysts, the reported performance have largely remained below the widely-cited commercial viability target of a minimum single-pass C_2 yield of ~ 30% at a C_2 selectivity of ~ 90%, using undiluted feed streams.[15,16]

A fundamental issue with OCM is that, at the high temperatures applied, undesired over oxidation products such as CO and CO_2 (CO_x) are more thermodynamically favored than the C_2 products.[15] Furthermore, when conventional co-fed packed bed reactors (PBRs) are used, the desired C_2 products can be converted sequentially to CO_x at relatively higher rates, [12,17] and in general the C_2 selectivity decreases as methane conversion increases. It has also been demonstrated that the C_2 selectivity in OCM is higher at lower oxygen partial pressures (i.e., higher CH_4/O_2 ratios) [12,18]. These observations have been used to argue that reactors with a distributed oxygen feed, such as a membrane reactor, can give significantly higher C_2 yields than a co-fed packed bed reactor modeled under the same operating conditions.[15]

The most common type of membrane reactor studied in OCM are solid oxide membranes which operate at high temperatures (> 923 K). The configuration of these membranes is such that the methane and oxygen-containing streams (e.g., air) are separated by an ion-conducting membrane which transfers O^{2-} from the oxygen side to the methane side where the OCM reaction occurs. An added advantage of this membrane reactor is that it is able to supply the catalyst with pure oxygen from air without a costly separation step due to the lack of transfer of other air components (e.g., N_2).[15] For these membranes to conduct O^{2-} effectively, there is a need for countercurrent flow of electrons to fulfill overall charge neutrality in the membrane. This is

commonly achieved by using a mixed ionic and electronic conducting (MIEC) membrane, where the electrons are transferred through the membrane itself in the opposite direction of O^{2-}.

Despite the potential benefits of solid oxide membrane reactors over conventional co-fed reactors, the performance of these systems in OCM are also generally below the techno-economic target.[15,19] An issue that has limited the performance of membrane reactors in OCM is the relatively low oxygen fluxes through the membranes which, aside from limiting methane conversion, promotes carbon deposition and catalyst/membrane deactivation. In general, MIEC membranes doped with transition metal ions (e.g., Co and Fe) give higher oxygen fluxes.[20] However, it has been demonstrated that the presence of transition metal ions in membrane materials leads to a dramatic decline in OCM selectivity.[21]

In the present study, we aim to develop alternative O^{2-} conducting materials that are selective for OCM. This step is considered crucial to the advancement of OCM membrane reactors. Specifically, we focus our attention on doped barium cerates because they are a class of high temperature O^{2-} conducting membrane materials composed of elements that have been shown to be selective in OCM. [9,22–25] A potential problem in using doped barium cerate membranes in OCM is that the perovskite structure of barium cerate ($BaCeO_3$) is prone to destruction on prolonged exposure to CO_2-containing atmospheres.[26] This phase instability has been attributed to a thermodynamically favorable reaction of the perovskite with CO_2 to form $BaCO_3$ and CeO_2 at temperatures below ~ 1373 K.[26–28] Destruction of the perovskite structure can lead to conductivity losses and mechanical failure which are both detrimental to the performance of these membrane reactors.[29]

In this contribution, we study the performance and stability of gadolinium-doped barium cerate ($BaCe_{0.8}Gd_{0.2}O_{3-\delta}$ or BCG) and Zr-doped BCG under OCM operating conditions. The

rationale behind studying the Zr-doped sample is that doped barium zirconates ($BaZrO_3$) are more thermodynamically resistant to CO_2 attack compared to doped barium cerates.[26–28] We present conversion-selectivity and conversion-yield curves that illustrate the OCM performance of the BCG and Zr-doped BCG powders in a packed bed reactor. The phase instability of BCG under OCM conditions is confirmed and related to the presence of CO_2, with higher CO_2 concentrations leading to more rapid transformation of BCG into $BaCO_3$, CeO_2 and Gd_2O_3 like phases. We show that the phase stability of BCG in OCM can be improved by doping with Zr without significantly affecting the C_2 yields obtained. To our knowledge, the phase structure and performance stability of gadolinium-doped barium cerate powders in OCM has not been previously investigated.

3.3 Experimental

3.3.1 Catalyst synthesis

The doped barium cerate powders were synthesized using a modified pechini method described partly elsewhere.[30] In this method, ethylenediaminetetraacetic acid (EDTA, Fisher Scientific, 99.7%) was mixed with deionized water followed by the addition of aqueous ammonia (29% NH_4OH, Fisher Scientific) to aid the dissolution of EDTA and adjust the pH of the solution to ~ 10. In another flask, barium nitrate (Sigma Aldrich, ≥ 99%) was dissolved in deionized water. The EDTA/NH_4OH solution was added to the barium nitrate solution under continuous stirring at 353 K (solution A). In a third flask, stoichiometric amounts of cerium (III) nitrate hexahydrate (Acros Organics, 99.5%) and gadolinium (III) nitrate hexahydrate (Acros Organics, 99.9%) required to form the composition of BCG were dissolved in deionized water (solution B). For the $BaCe_{0.4}Zr_{0.4}Gd_{0.2}O_{3-\delta}$ (BCZG) catalyst, a stoichiometric amount of zirconium dinitrate oxide hydrate (Alfa Aesar, 99.9%) was also added to solution B. Solution B was added dropwise to solution A while stirring at 353 K. Subsequently, ethylene glycol (J.T. Baker) was added to the

mixture. The EDTA/metal ion and EDTA/ethylene glycol molar ratio used in synthesis were 1.5 and 1/3, respectively. The resulting mixture was sealed and left to stir overnight at 353 K to promote polymerization, and then evaporated at the same temperature until a viscous gel was formed. The gel was calcined at 523 K for 2 hours with temperature ramps of 2 K/min resulting in a black ash. The ash was lightly grinded using a mortar and pestle then calcined again at 1273 K for 4 hours with temperature ramps of 2 K/min to form the final powder.

3.3.2 Catalyst characterization

The X-ray Diffraction (XRD) patterns of the catalyst powders was obtained using a Rigaku MiniFlex 600 spectrometer (Cu Kα source, $\lambda = 1.54059$ Å) equipped with JADE software for phase identification and data processing. The device was operated at a tube voltage and current of 40kV and 15mA, respectively. A continuous sweep mode was used to collect the data in a 2Θ range from 20 to 90 at a speed of 2°(2Θ) per minute and a step size of 0.02°. The BET surface areas of the catalysts were measured using a Micrometrics 3-Flex Surface Characterization Analyzer. Prior to the BET measurement, the catalysts were degassed under vacuum at 698 K for 4 hours to remove moisture and other adsorbed volatiles. Bulk composition of the materials was measured using Wavelength Dispersive X-ray Spectrometry (WDS), using a Cameca SX100 electron probe microanalyzer (EPMA) at the University of Michigan Electron Microbeam Analysis Lab (EMAL). WDS measurements were conducted using a focused electron beam with an accelerating voltage of 15 keV and a beam current of 20 nA. Synthetic zircon (Zr Lα), synthetic gadolinium-aluminum garnet (Gd Lα), synthetic alforsite (Ba Lα) and synthetic $CePO_4$ (Ce Lα) were used for calibration. Compositions were calculated from raw intensities using the X-PHI intensity correction method.[31] In preparation for WDS measurements, the catalyst powders were pressed into cylindrical pellets, sintered at 1650°C to reduce porosity and polished to reduce surface defects.

3.3.3 OCM catalytic tests

Prior to the catalyst tests, the synthesized powders were pressed, crushed and sifted to agglomerates of ~ 125 - 350 μm in diameter. Unless stated otherwise, approximately 110 mg of sifted powder was used in each experiment. The sifted powder was positioned in the center of a 6.35 mm ID quartz tube and held in place with silica wool on both sides. The quartz tube containing the catalyst powder was oriented horizontally in a furnace and heated to the desired temperature at a rate of 2 K/min under argon flow. A thermocouple was positioned next to the center of the quartz tube to monitor the reactor temperature. At the desired reactor temperature, methane (containing 5% helium) and air were fed to the reactor through mass flow controllers (Cole-Palmer) and the argon flow was discontinued. The effluent gases leaving the reactor were analyzed in a Varian CP-3800 gas chromatograph (GC) equipped with thermal conductivity and flame ionization detectors. The GC was calibrated for each measured component using certified gas mixtures supplied by Cryogenic Gases (PurityPlus). The methane conversion (X), C_{2+} selectivity (S) and C_{2+} yield (Y) were calculated using Equations 3.1 – 3.3,[21] where C_{2+} denotes ethane, ethylene, propane and propylene. In all experiments, the estimated carbon balance was ≥ 96%. The data points reported are averages of at least 3 experimental measurements and the error bars represent the calculated standard deviations.

$$X(\%) = \frac{moles\ of\ methane\ consumed}{moles\ of\ methane\ fed} \times 100 \tag{3.1}$$

$$S(\%) = \frac{[2(moles\ of\ C_2H_4 + C_2H_6\ ) + 3(moles\ of\ C_3H_6 + C_3H_8)]_{products}}{moles\ of\ methane\ consumed} \times 100 \tag{3.2}$$

$$Y(\%) = \frac{SX}{100} \tag{3.3}$$

3.4 Results and Discussion

3.4.1 Synthesis

The XRD spectra of the as-synthesized BCG and BCZG powders are shown in Figure 3.1. The spectra confirm that the perovskite structures were successfully obtained without the presence of significant secondary phases. The spectra also show that the peak positions from BCZG is at slightly higher angles compared to BCG which is expected as the perovskite unit volume should decrease when the Zr^{4+} ion of smaller ionic radius (R^{IV} = 0.72 Å) partially replaces the larger Ce^{4+} ion (R^{IV} = 0.87 Å).[28,32] The estimated BET surface area of the as-synthesized BCG and BCZG catalyst were ~ 3.7 m^2/g and 6.5 m^2/g, respectively. Such low surface area is expected for unsupported perovskite oxide catalysts calcined in air at a high temperature of 1273 K.[33,34] Table 3.1 shows the bulk composition of the BCG and BCZG catalysts from stoichiometric calculations and WDS measurements. The stoichiometric weight (%) was calculated based on the weight of each metal element required for the synthesis of the catalysts. As shown in Table 3.1, the WDS composition are reasonably close to the stoichiometric composition.

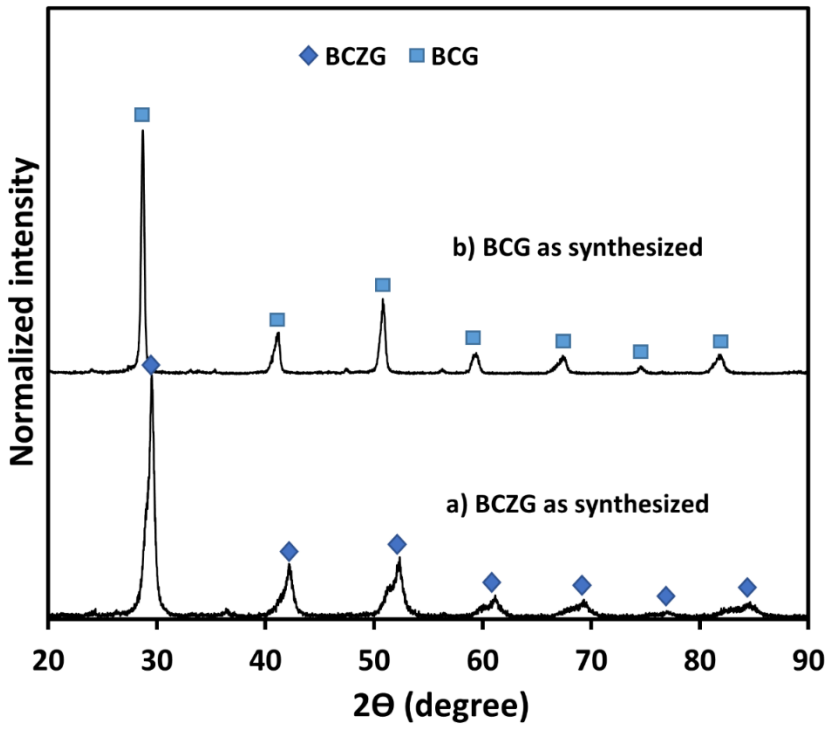

Figure 3.1. XRD patterns of as-synthesized powders (a) BCZG and (b) BCG

Table 3.1. Catalyst composition from stoichiometric calculations and WDS measurements

	$BaCe_{0.8}Gd_{0.2}O_{3-\delta}$		$BaCe_{0.4}Zr_{0.4}Gd_{0.2}O_{3-\delta}$	
Element	Stoichiometric (wt%)	WDS (wt%)	Stoichiometric (wt%)	WDS (wt%)
Ba	41.8	39.6	44.4	42.6
Ce	34.1	35.3	18.1	19.9
Zr	-	-	11.8	10.4
Gd	9.6	9.4	10.2	8.7

3.4.2. Catalytic performance of BCG in OCM

The data in Figure 3.2 show the C_{2+} selectivity, C_{2+} yield, and methane conversion for the BCG catalyst as a function of the CH_4/O_2 feed ratio. These experiments were performed at 1023 K and the different CH_4/O_2 ratios were obtained by varying the flowrate of the methane and air streams while keeping the total flow rate constant at 100 cm^3/min. Note that all flow rates are given at standard conditions (STP). The methane stream (containing 5% He) flowrate was varied between 25 – 95 cm^3/min, while the air flowrate was varied between 5 – 75 cm^3/min. The data show that the C_{2+} selectivity decreases with increasing methane conversion which is typical for OCM catalytic reactions and attributable to increased sequential reactions of the desired C_2 products to more thermodynamically favored CO_x products at higher methane conversions. A maximum C_{2+} selectivity of ~ 90% was attained at a high CH_4/O_2 ratio of 86, which resulted in relatively low methane conversion. The C_{2+} yield increased with methane conversion to a maximum value of ~ 14 % at a CH_4/O_2 ratio of 2.4. It should be noted that, at 1023 K and a CH_4/O_2 ratio of 2.4, the CH_4 conversion and C_{2+} yield obtained from experiments with silica wool only was 2.2% and 1.2%, respectively. Furthermore, at a CH_4/O_2 of 86, a methane conversion of ~ 0.01% was achieved in the presence of silica wool only at 1023K. These values are considered negligible compared to that obtained in the presence of the BCG catalyst.

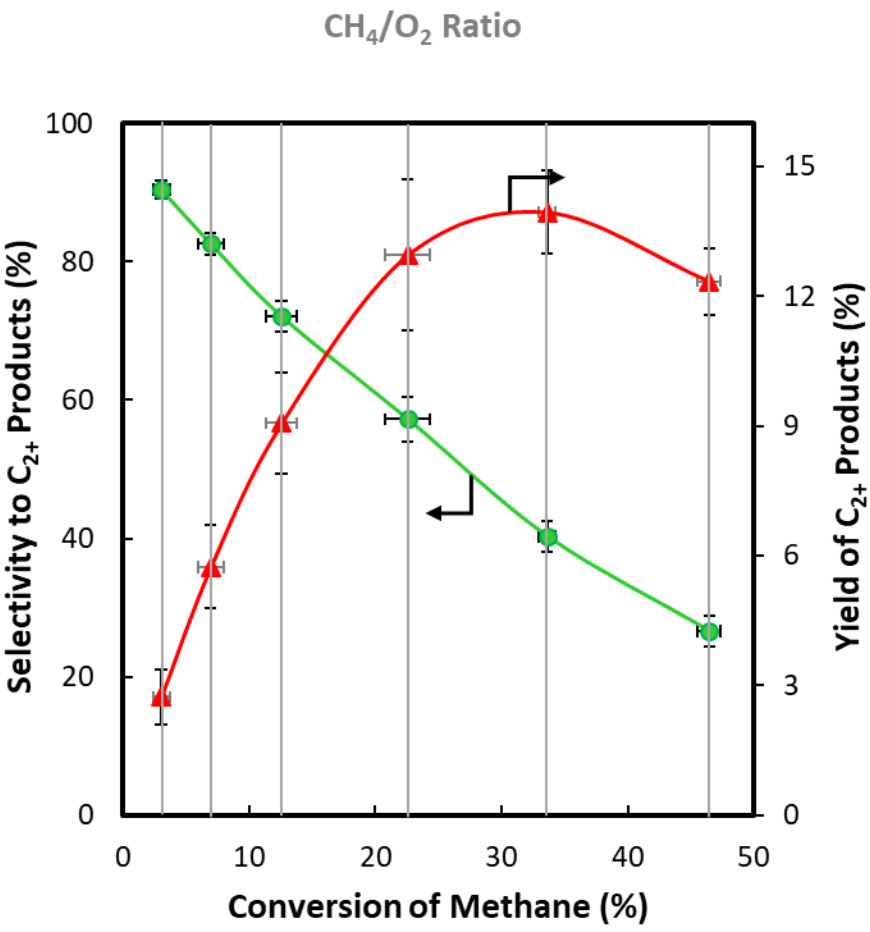

Figure 3.2. Dependence of C_{2+} selectivity, C_{2+} yield and methane conversion from BCG catalyst on CH_4/O_2 feed ratio. Temperature = 1023 K. Total flow = 100 cm^3/min. Catalyst weight = 110 mg.

The BCG catalyst was tested at different temperatures while using a constant methane stream flow of 35 cm^3/min and an air flow of 65 cm^3/min (i.e., CH_4/O_2 feed ratio of 2.4). The amount of higher hydrocarbons (i.e. propane and propylene) produced in these experiments were below 0.08 mol % and considered negligible. The data in Figure 3.3a show the methane conversion, C_{2+} selectivity and the C_2H_4/C_2H_6 ratio at temperatures between 1023 K and 1123 K. The data show that methane conversion was not significantly affected by temperature in the studied temperature range which is expected since oxygen is nearly exhausted (oxygen conversion ≥ 97%)

at these conditions. The effect of temperature on methane conversion is expected to become significant under conditions where the oxygen conversion is relatively low (e.g., lower temperatures). The data also show that the overall C_{2+} selectivity decreases while the C_2H_4/C_2H_6 ratio increases with increasing temperature. This is accompanied by a decrease in the yield of ethane, and an increase in the yield of ethylene as shown in Figure 3.3b. The data indicates increased occurrence of sequential reactions of ethane to ethylene and CO_x at higher temperatures.

3.4.3 Stability studies of BCG in OCM

The spent catalyst was collected and characterized using XRD. The XRD spectrum of the spent BCG catalyst is shown in Figure 3.4b. This catalyst was characterized after testing for several hours at 1023 K, using CH_4/O_2 ratios ranging from 1.5 to 86 consecutively. The spectrum of unreacted BCG catalyst is also included (Figure 3.4a) for comparison. Analysis of the spectrum of the reacted catalyst reveals that the BCG perovskite phase, which is required for ion and electron conduction,[29] had been significantly transformed. The spectrum suggests the emergence of $BaCO_3$, CeO_2 and Gd_2O_3 like phases. This phase transformation is likely caused by a reaction of BCG with CO_2 as discussed previously.

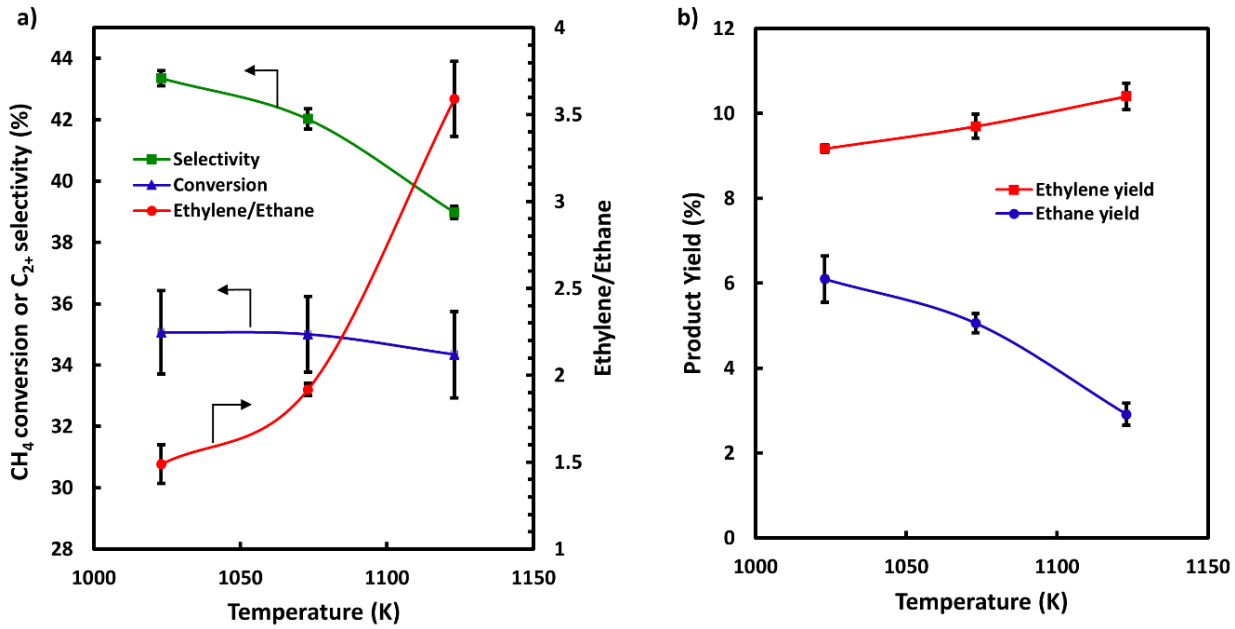

Figure 3.3. Effect of temperature on (a) CH_4 conversion, C_{2+} selectivity and C_2H_4/C_2H_6 ratio, (b) Ethylene and Ethane yields, from BCG catalyst. Total flow = 100 cm^3/min. CH_4/O_2 = 2.4. Catalyst weight = 110 mg.

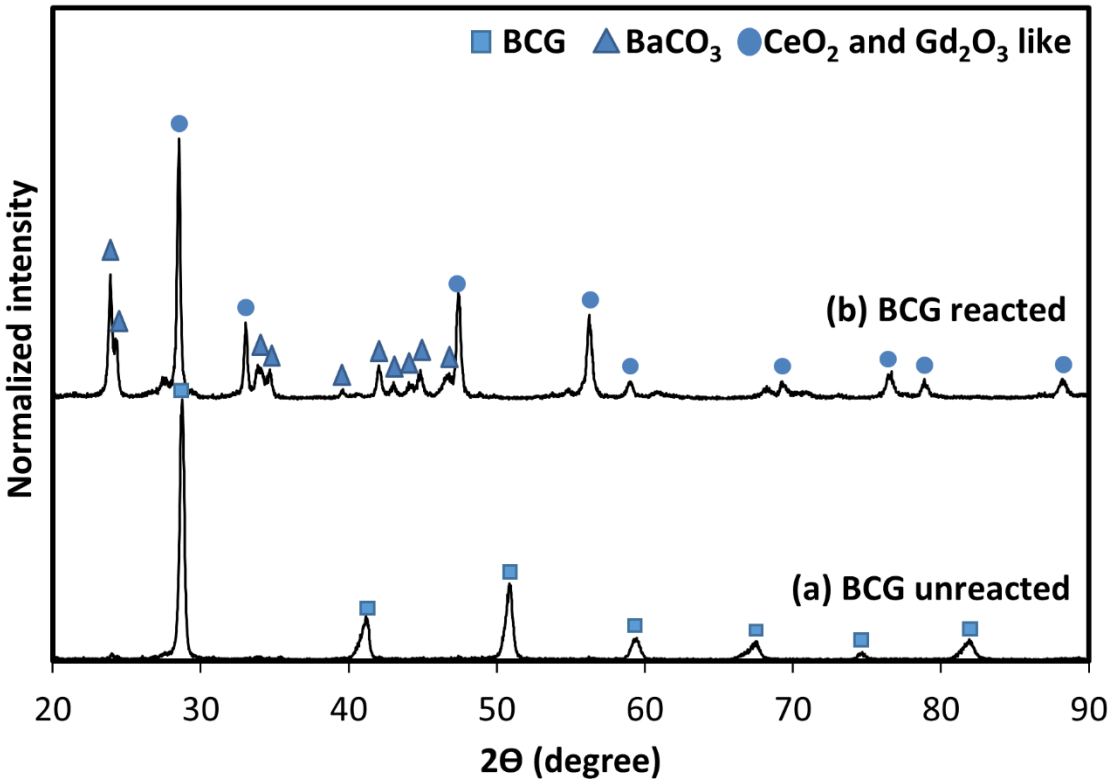

Figure 3.4. XRD patterns of (a) unreacted BCG and (b) BCG reacted at 1023 K using CH_4/O_2 ratios ranging from 1.5 to 86 consecutively.

To determine the effect of CO_2 concentration on BCG phase stability in OCM, additional experiments were conducted using high and low CH_4/O_2 ratios. As shown above, the CO_2 concentration is higher at lower CH_4/O_2 ratios. These experiments were performed at 1023 K with a total flowrate of 100 cm^3/min using 200 mg of catalyst powder. In each experiment, the catalyst was heated and cooled in argon flow to minimize any chemical transformations that could occur during heating and cooling. The XRD data for the unreacted BCG catalyst and BCG catalysts reacted at different CH_4/O_2 ratios are presented in Figure 3.5. The data show that the catalysts tested at a high CH_4/O_2 ratio of 26 for one hour (Figure 3.5b) and six hours (Figure 3.5c) largely retained their perovskite structure. On the other hand, the catalyst used for only 1 hour, at a low CH_4/O_2 ratio of 2.4 (Figure 3.5d), changed significantly, segregating into the $BaCO_3$, CeO_2 and Gd_2O_3 phases. The estimated CO_2 concentration at the reactor outlet was ~ 0.7 mol% for the reaction performed at a CH_4/O_2 ratio of 26, while it was ~ 6.2 mol% at a CH_4/O_2 ratio of 2.4. These data show that the phase structure of BCG is more readily decomposed at higher CO_2 concentrations. Furthermore, despite the observed changes in phase structure of the BCG catalyst, the data in Figure 3.6 show that the methane conversion, C_{2+} selectivity and C_{2+} yield obtained was relatively stable over 48 hours on stream using a low CH_4/O_2 ratio of 2.4. The data suggest that the phase change in the catalyst does not result in a significant change in the catalyst performance. The performance of BCG remains stable even with significant phase changes probably because at least one of the new phases formed is also active for OCM. For example, $BaCO_3$ and Ba/CeO_2 have been shown to be active for OCM in previous studies.[22,23,35]

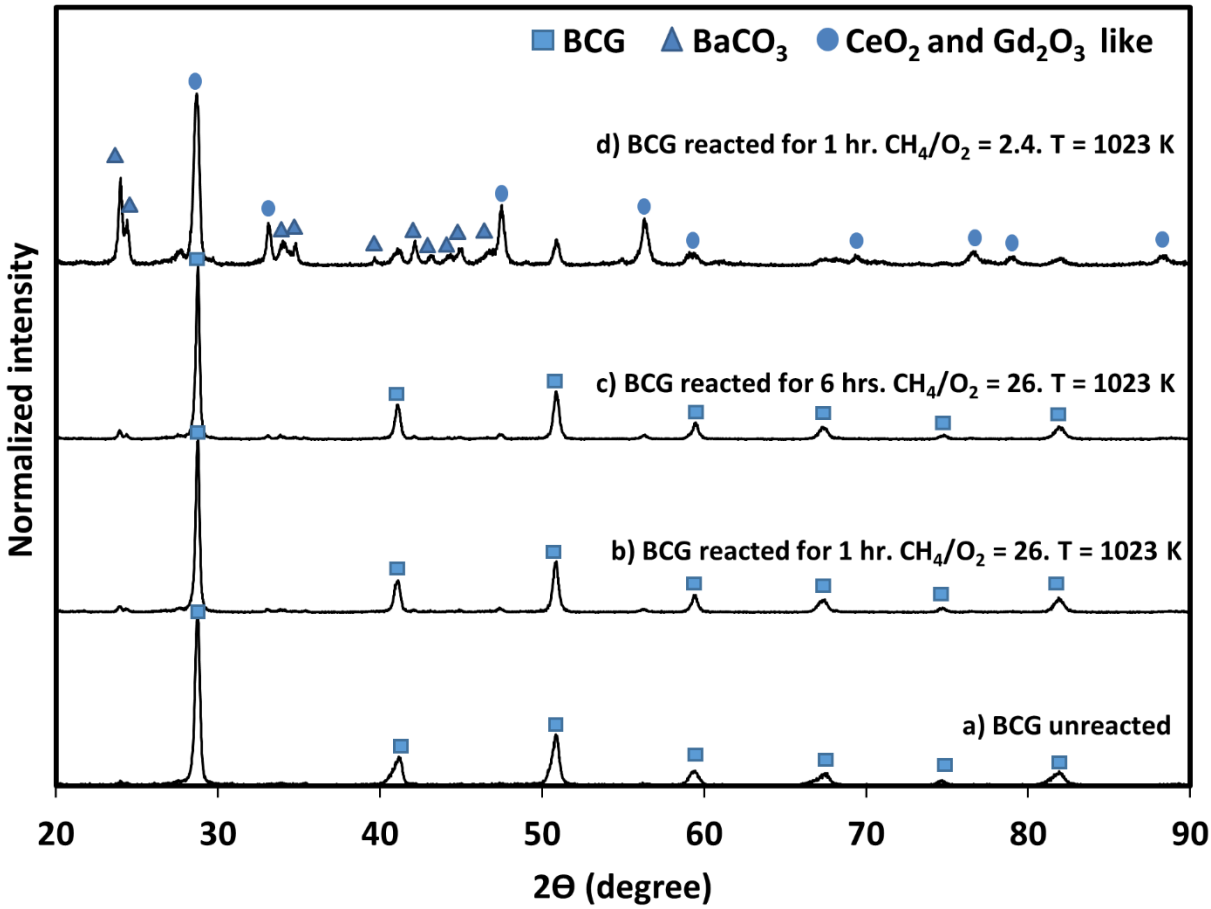

Figure 3.5. XRD patterns from (a) unreacted BCG (b) BCG reacted for 1 hour at CH_4/O_2 = 26 and T = 1023 K (c) BCG reacted for 6 hours at CH_4/O_2 = 26 and T = 1023 K and (d) BCG reacted for 1 hour at CH_4/O_2 = 2.4 and T = 1023 K.

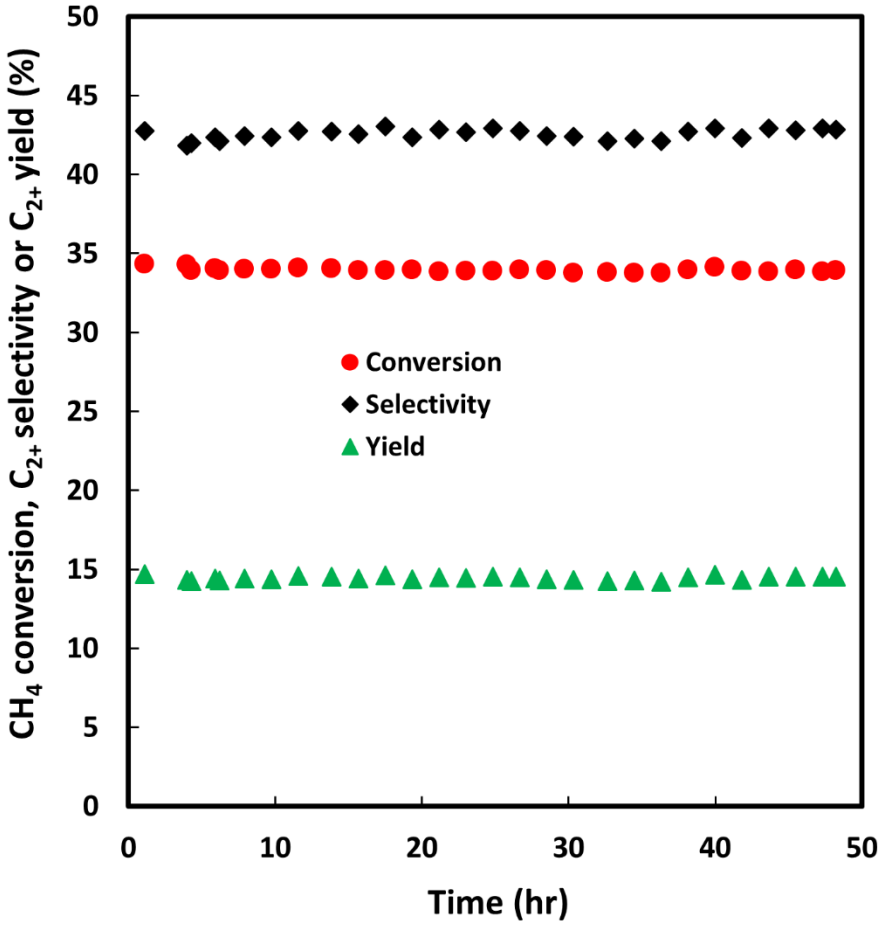

Figure 3.6. Plot of CH_4 Conversion, C_{2+} selectivity and C_{2+} yield over time from BCG catalyst. Catalyst weight = 110 mg. CH_4/O_2 = 2.4. Total flow rate = 100 cm^3/min. Temperature = 1023 K.

3.4.4 Effect of Zr doping on BCG performance and phase stability

Based on our analysis of the performance of the BCG catalyst, we conclude that this material can perform OCM with high selectivity to C_{2+} products under low O_2/CH_4 ratios. This high performance along with the ion/electron conducting properties of BCG makes it a promising material for use as membrane or catalyst in solid oxide membrane reactors for OCM. The issue with this material is that, as we described above, even small amounts of CO_2, which is inevitable

at elevated (and realistic) methane conversion, results in changes in its perovskite structure. While these changes do not have much effect on the catalytic performance of this material, these changes are expected to have a dramatic effect on its ion/electron conducting properties. To address this problem of instability of the perovskite phase of BCG in OCM, we probed the impact of introducing Zr into the structure of BCG. As mentioned previously, the phase structure of $BaZrO_3$ is more stable than $BaCeO_3$ in CO_2 containing environment.

Data in Figure 3.7a and b show respective conversion-selectivity and conversion-yield curves from the Zr-doped BCG catalyst (BCZG) and undoped BCG. These experiments were also performed at 1023 K, CH_4/O_2 ratios of 1.5 - 86 and using 110 mg of catalyst. The data show that the catalysts exhibit very similar performance, and that the introduction of Zr has no negative effect on the catalytic performance of BCG. Data in Figure 3.8a and b show the selectivity of carbon-containing products formed during the reaction with BCG and BCZG catalyst, respectively, as a function of the methane conversion. As shown in the figures, the product distribution obtained from the BCG and BCZG catalyst is similar, which indicates a similar reaction mechanism on the both catalysts. The ethane selectivity is high at low methane conversions, which corresponds to high CH_4/O_2 ratios. As the methane conversion increases due to decreasing the CH_4/O_2 ratio, the ethane selectivity decreases monotonously. The ethylene and C_3 (propane and propylene)

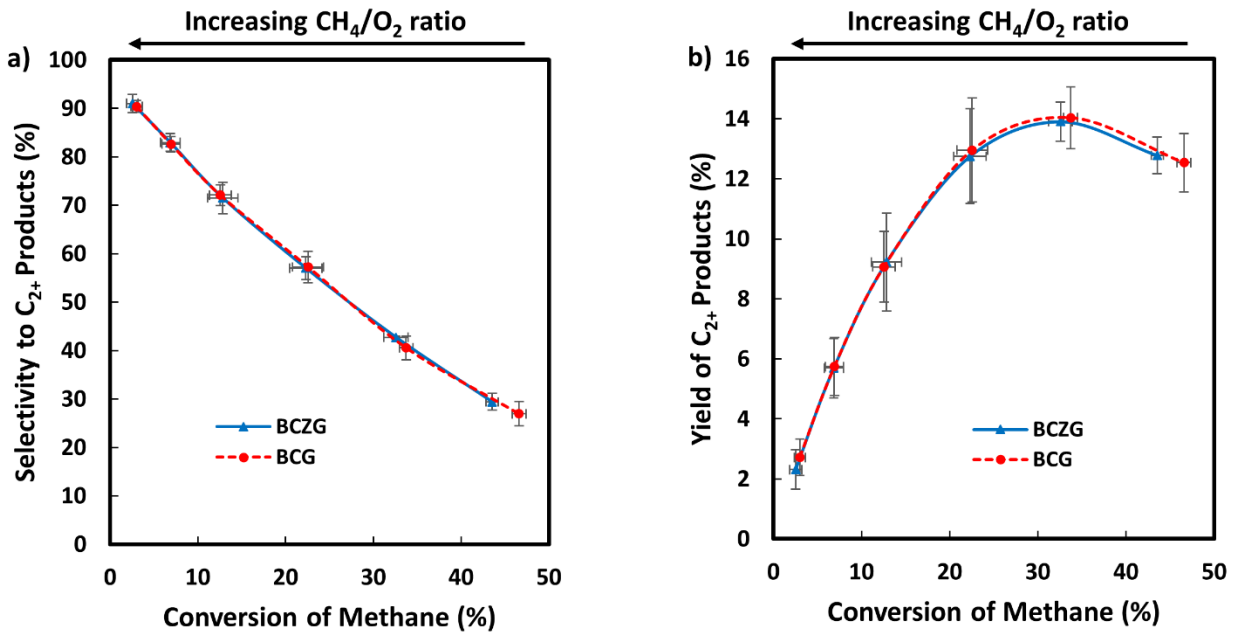

Figure 3.7. (a) Conversion-selectivity curve and (b) conversion-yield curve from BCG and BCZG catalyst. Temperature = 1023 K. Total flow =100 cm^3/min. Catalyst weight = 110 mg. CH_4/O_2 ratio = 1.5 – 86. The CH_4/O_2 ratio increases from the right to the left of the plots as indicated by the arrows above the figures

selectivity increase with increasing methane conversion, reach a maximum, and then decrease. The CO_x selectivity increased monotonously with increasing methane conversion (i.e., decreasing CH_4/O_2 ratio). This data indicate that ethane is the primary product formed in the reaction. The decrease in ethane selectivity and increase in CO_x selectivity with increasing methane conversion is consistent with the occurrence of higher sequential reactions of ethane to CO_x at lower CH_4/O_2 feed ratios.

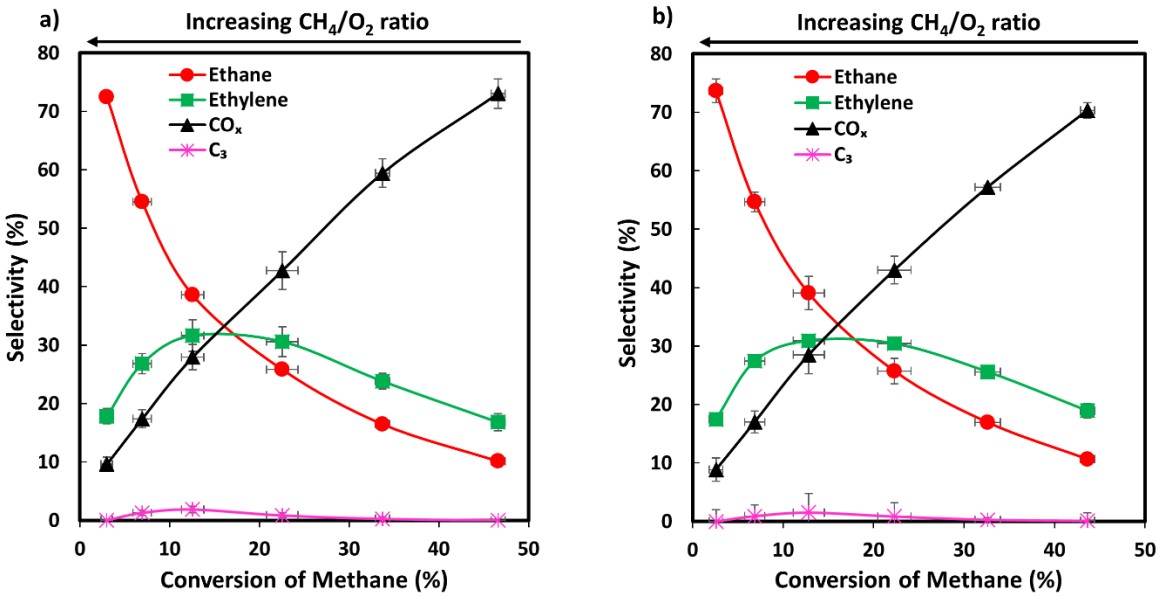

Figure 3.8. Selectivity of carbon-containing products (C_2H_6, C_2H_4, CO_x and C_3) as a function of methane conversion for (a) BCG catalyst (b) BCZG catalyst. C_3 represents propane and propylene. The CH_4/O_2 ratio increases from the right to the left of the plots as indicated by the arrows above the figures.

The XRD spectra for unreacted and reacted BCG and BCZG catalysts are shown in Figure 3.9. The spectra of the reacted catalysts were obtained from samples tested at 1023 K, a low CH_4/O_2 feed ratio of 2.4 and a total flow rate of 100 cm^3/min. The data show that there was no significant change in the phase structure of the BCZG catalyst reacted for 1 hour (Figure 3.9c) compared to the unreacted BCZG catalyst (Figure 3.9a). New phases corresponding to $BaCO_3$, CeO_2 and Gd_2O_3 start appearing in the BCZG catalyst reacted for over 48 hours (Figure 3.9d). Comparison between the XRD spectrum of the BCG catalyst reacted for 1 hour (Figure 3.9e) and the spectra of the reacted BCZG catalysts showed that the introduction of Zr to BCG improves phase stability, without changing the C_{2+} yields. Figure 3.10 presents a plot of CH_4 conversion,

C_{2+} selectivity and C_{2+} yield from BCZG over time using a CH_4/O_2 ratio of 2.4. The data show that the catalytic performance was relatively stable over 48 hours.

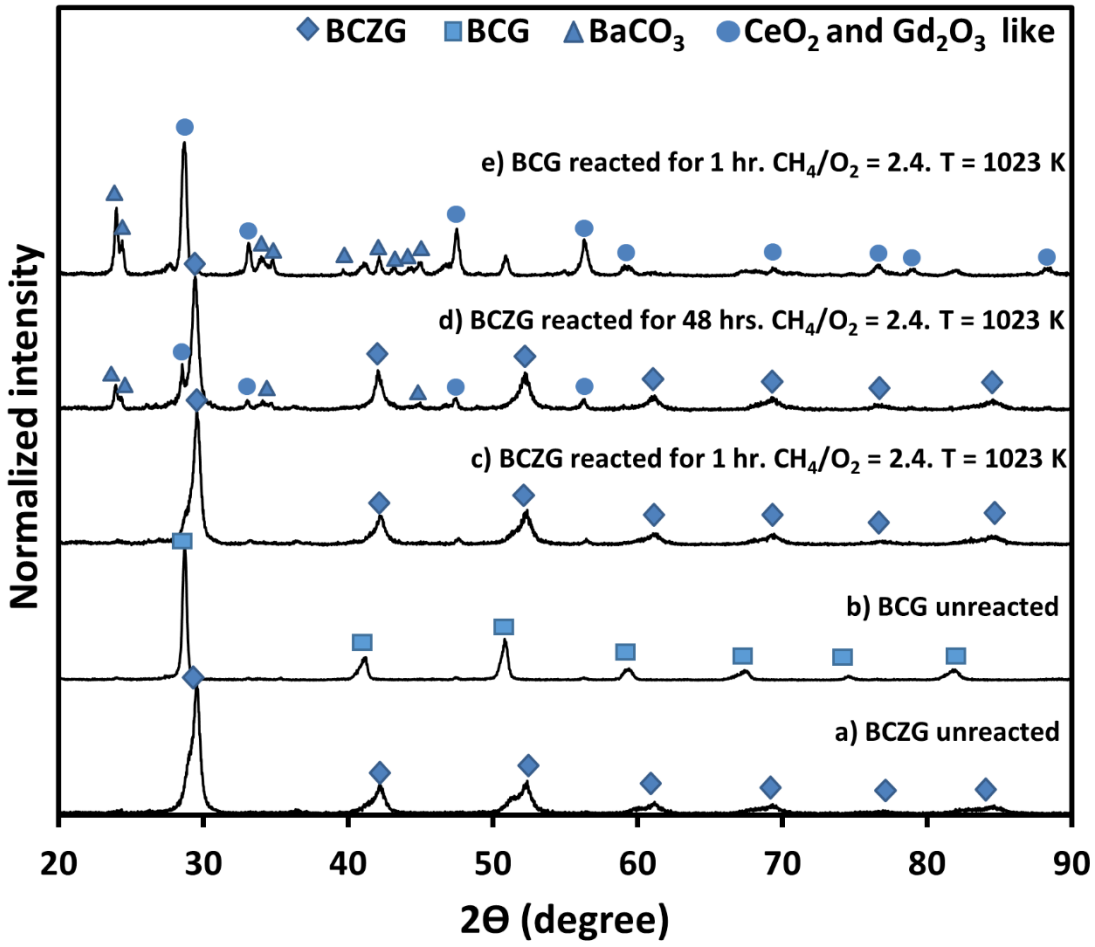

Figure 3.9. XRD patterns of (a) unreacted BCZG (b) unreacted BCG (c) BCZG reacted for 1 hour at CH_4/O_2 = 2.4 and T = 1023 K (d) BCZG reacted for 48 hours at CH_4/O_2 = 2.4 and T = 1023 K (e) BCG reacted for 1 hour at CH_4/O_2 = 2.4 and T = 1023 K.

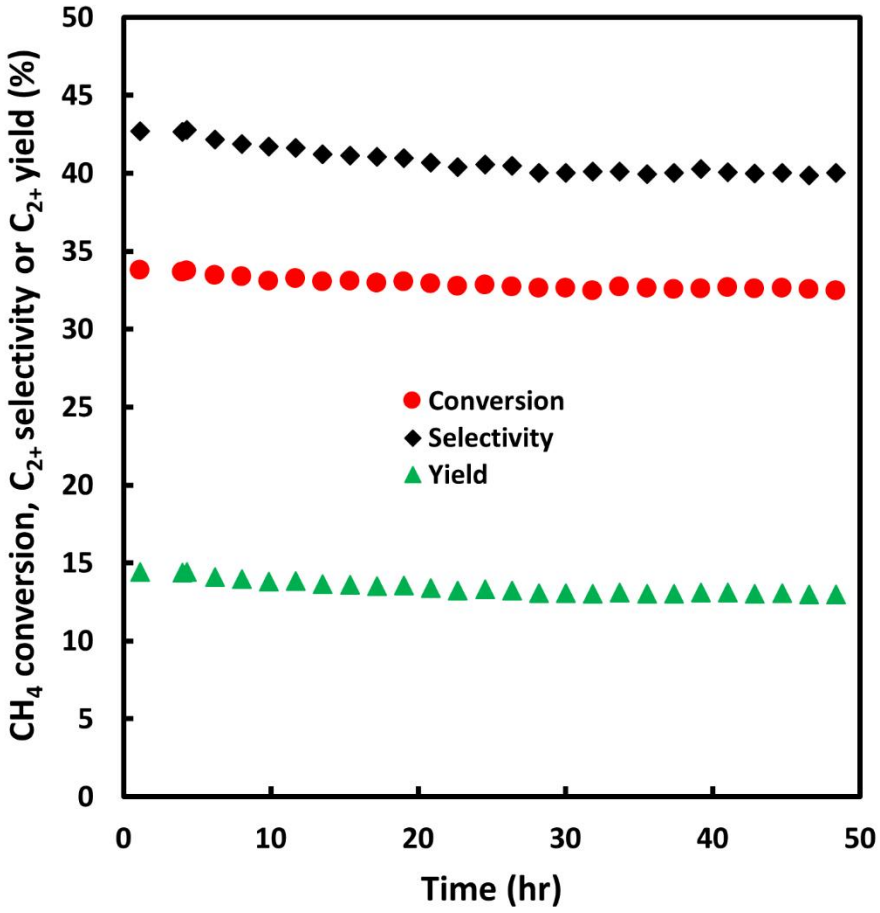

Figure 3.10. Plot of CH_4 Conversion, C_{2+} selectivity and C_{2+} yield over time from BCZG catalyst. Catalyst weight = 110 mg. CH_4/O_2 = 2.4. Total flow rate = 100 cm^3/min. Temperature = 1023 K.

3.5 Conclusions

We performed OCM tests on $BaCe_{0.8}Gd_{0.2}O_{3-\delta}$ (BCG) powders in a packed bed reactor (PBR) and obtained high C_{2+} selectivities (up to 90%) at low O_2 partial pressures expected to occur in membrane reactors. For the conditions tested, a maximum C_{2+} yield of ~ 14% was achieved at 1023 K and a CH_4/O_2 feed ratio of 2.4. Under this reaction condition, phase segregation of BCG into $BaCO_3$, CeO_2 and Gd_2O_3 like phases occurred, and this phase instability was related to the presence of CO_2. While this phase transformation is not detrimental to the CH_4 conversion, C_{2+} selectivity and C_{2+} yield, the loss of the perovskite structure is detrimental to the ionic and electronic conductivity of the material, which is important for its application in OCM membrane reactors. We showed that by doping BCG with Zr, the phase instability in OCM is suppressed without significantly affecting the C_2 yields in a PBR.

3.6 References:

(1) U.S. Crude Oil, Natural Gas, and Natural Gas Proved Reserves, Year-end 2018 https://www.eia.gov/naturalgas/crudeoilreserves/ (accessed Dec 17, 2019).

(2) Horn, R.; Schlögl, R. Methane Activation by Heterogeneous Catalysis. *Catal. Lett.* **2015**, *145* (1), 23–39.

(3) McFarland, E. Unconventional Chemistry for Unconventional Natural Gas. *Science* **2012**, *338* (6105), 340–342.

(4) Guo, X.; Fang, G.; Li, G.; Ma, H.; Fan, H.; Yu, L.; Ma, C.; Wu, X.; Deng, D.; Wei, M.; et al. Direct, Nonoxidative Conversion of Methane to Ethylene, Aromatics, and Hydrogen. *Science* **2014**, *344* (6184), 616–619.

(5) Olivos-Suarez, A. I.; Szécsényi, À.; Hensen, E. J.; Ruiz-Martinez, J.; Pidko, E. A.; Gascon, J. Strategies for the Direct Catalytic Valorization of Methane Using Heterogeneous Catalysis: Challenges and Opportunities. *ACS Catal.* **2016**, *6* (5), 2965–2981.

(6) Schwach, P.; Pan, X.; Bao, X. Direct Conversion of Methane to Value-Added Chemicals over Heterogeneous Catalysts: Challenges and Prospects. *Chem. Rev.* **2017**, *117* (13), 8497–8520.

(7) V. Kondratenko, E.; Peppel, T.; Seeburg, D.; A. Kondratenko, V.; Kalevaru, N.; Martin, A.; Wohlrab, S. Methane Conversion into Different Hydrocarbons or Oxygenates: Current

Status and Future Perspectives in Catalyst Development and Reactor Operation. *Catal. Sci. Technol.* **2017**, *7* (2), 366–381.

(8) Keller, G. E.; Bhasin, M. M. Synthesis of Ethylene via Oxidative Coupling of Methane: I. Determination of Active Catalysts. *J. Catal.* **1982**, *73* (1), 9–19.

(9) Zavyalova, U.; Holena, M.; Schlögl, R.; Baerns, M. Statistical Analysis of Past Catalytic Data on Oxidative Methane Coupling for New Insights into the Composition of High-Performance Catalysts. *ChemCatChem* **2011**, *3* (12), 1935–1947.

(10) Driscoll, D. J.; Martir, W.; Wang, J. X.; Lunsford, J. H. Formation of Gas-Phase Methyl Radicals over Magnesium Oxide. *J. Am. Chem. Soc.* **1985**, *107* (1), 58–63.

(11) Luo, L.; Tang, X.; Wang, W.; Wang, Y.; Sun, S.; Qi, F.; Huang, W. Methyl Radicals in Oxidative Coupling of Methane Directly Confirmed by Synchrotron VUV Photoionization Mass Spectroscopy. *Sci. Rep.* **2013**, *3*.

(12) Stansch, Z.; Mleczko, L.; Baerns, M. Comprehensive Kinetics of Oxidative Coupling of Methane over the La_2O_3/CaO Catalyst. *Ind. Eng. Chem. Res.* **1997**, *36* (7), 2568–2579.

(13) Arndt, S.; Otremba, T.; Simon, U.; Yildiz, M.; Schubert, H.; Schomäcker, R. Mn–Na_2WO_4/SiO_2 as Catalyst for the Oxidative Coupling of Methane. What Is Really Known? *Appl. Catal. Gen.* **2012**, *425*, 53–61.

(14) Arndt, S.; Laugel, G.; Levchenko, S.; Horn, R.; Baerns, M.; Scheffler, M.; Schlögl, R.; Schomäcker, R. A Critical Assessment of Li/MgO-Based Catalysts for the Oxidative Coupling of Methane. *Catal. Rev.* **2011**, *53* (4), 424–514.

(15) Farrell, B. L.; Igenegbai, V. O.; Linic, S. A Viewpoint on Direct Methane Conversion to Ethane and Ethylene Using Oxidative Coupling on Solid Catalysts. *ACS Catal.* **2016**, *6* (7), 4340–4346.

(16) Kuo, J. C. W.; Kresge, C. T.; Palermo, R. E. Evaluation of Direct Methane Conversion to Higher Hydrocarbons and Oxygenates. *Catal. Today* **1989**, *4* (3–4), 463–470.

(17) Labinger, J. A.; Ott, K. C. Mechanistic Studies on the Oxidative Coupling of Methane. *J. Phys. Chem.* **1987**, *91* (11), 2682–2684.

(18) Tiemersma, T. P.; Tuinier, M. J.; Gallucci, F.; Kuipers, J. A. M.; van Sint Annaland, M. A Kinetics Study for the Oxidative Coupling of Methane on a Mn/Na_2WO_4/SiO_2 Catalyst. *Appl. Catal. Gen.* **2012**, *433*, 96–108.

(19) Wang, B.; Albarracín-Suazo, S.; Pagán-Torres, Y.; Nikolla, E. Advances in Methane Conversion Processes. *Catal. Today* **2017**, *285*, 147–158.

(20) Sunarso, J.; Baumann, S.; Serra, J. M.; Meulenberg, W. A.; Liu, S.; Lin, Y. S.; Da Costa, J. D. Mixed Ionic–electronic Conducting (MIEC) Ceramic-Based Membranes for Oxygen Separation. *J. Membr. Sci.* **2008**, *320* (1), 13–41.

(21) Farrell, B.; Linic, S. Oxidative Coupling of Methane over Mixed Oxide Catalysts Designed for Solid Oxide Membrane Reactors. *Catal. Sci. Technol.* **2016**, *6*, 4370–4376.

(22) Au, C. T.; Chen, K. D.; Ng, C. F. The Modification of Gd_2O_3 with BaO for the Oxidative Coupling of Methane Reactions. *Appl. Catal. Gen.* **1998**, *170* (1), 81–92.

(23) Otsuka, K.; Shimizu, Y.; Komatsu, T. Ba Doped Cerium Oxides Active for Oxidative Coupling of Methane. *Chem. Lett.* **1987**, *16* (9), 1835–1838.

(24) Lu, Y.; Dixon, A. G.; Moser, W. R.; Ma, Y. H.; Balachandran, U. Oxygen-Permeable Dense Membrane Reactor for the Oxidative Coupling of Methane. *J. Membr. Sci.* **2000**, *170* (1), 27–34.

(25) Hibino, T.; Sato, T.; Ushiki, K.; Kuwahara, Y. Membrane Reactor for Oxidative Coupling of CH_4 with an Oxide Ion–electron Hole Mixed Conductor. *J Chem Soc Faraday Trans* **1995**, *91* (24), 4419–4422.

(26) Medvedev, D. A.; Lyagaeva, J. G.; Gorbova, E. V.; Demin, A. K.; Tsiakaras, P. Advanced Materials for SOFC Application: Strategies for the Development of Highly Conductive and Stable Solid Oxide Proton Electrolytes. *Prog. Mater. Sci.* **2016**, *75*, 38–79.

(27) Talimi, M.; Thangadurai, V. Electrical Conductivity and Chemical Stability of Perovskite-Type $BaCe_{0.8-x}Ti_xY_{0.2}O_{3-\delta}$. *Ionics* **2011**, *17* (3), 195–200.

(28) Ryu, K. H.; Haile, S. M. Chemical Stability and Proton Conductivity of Doped BaCeO 3–$BaZrO_3$ Solid Solutions. *Solid State Ion.* **1999**, *125* (1), 355–367.

(29) Wang, Y.; Wang, H.; Liu, T.; Chen, F.; Xia, C. Improving the Chemical Stability of $BaCe_{0.8}Sm_{0.2}O_{3-\delta}$ Electrolyte by Cl Doping for Proton-Conducting Solid Oxide Fuel Cell. *Electrochem. Commun.* **2013**, *28*, 87–90.

(30) Agarwal, V.; Liu, M. Preparation of Barium Cerate-Based Thin Films Using a Modified Pechini Process. *J. Mater. Sci.* **1997**, *32* (3), 619–625.

(31) Merlet, C. An Accurate Computer Correction Program for Quantitative Electron Probe Microanalysis. *Microchim. Acta* **1994**, *114* (1), 363–376.

(32) Zuo, C.; Dorris, S. E.; Balachandran, U.; Liu, M. Effect of Zr-Doping on the Chemical Stability and Hydrogen Permeation of the Ni-$BaCe_{0.8}Y_{0.2}O_{3-\alpha}$ Mixed Protonic-Electronic Conductor. *Chem. Mater.* **2006**, *18* (19), 4647–4650.

(33) Kirchnerova, J.; Klvana, D.; Vaillancourt, J.; Chaouki, J. Evaluation of Some Cobalt and Nickel Based Perovskites Prepared by Freeze-Drying as Combustion Catalysts. *Catal. Lett.* **1993**, *21* (1), 77–87.

(34) Gunasekaran, N.; Saddawi, S.; Carberry, J. J. Effect of Surface Area on the Oxidation of Methane over SolidOxide Solution Catalyst $La_{0.8}Sr_{0.2}MnO_3$. *J. Catal.* **1996**, *159* (1), 107–111.

(35) Aika, K.; Moriyama, T.; Takasaki, N.; Iwamatsu, E. Oxidative Dimerization of Methane over $BaCO_3$, $SrCO_3$ and These Catalysts Promoted with Alkali. *J. Chem. Soc. Chem. Commun.* **1986**, No. 15, 1210–1211.

Chapter 4

Oxidative Coupling of Methane over Membrane/Catalyst Hybrid Systems: Reactor Performance at High Methane Concentrations

4.1 Summary

Solid oxide membrane/catalyst hybrid systems have been proposed as a promising platform for selective oxidative coupling of methane to form higher values C_{2+} products. In these hybrid systems, the membrane controls the local chemical potential of reacting oxygen atoms while the catalyst allows for selective reaction of these oxygen atoms with methane to form the desired C_2 products. One critical challenge with these systems is that due to relatively low local O_2/CH_4 ratios, they can promote carbon-induced catalyst deactivation. Herein, we demonstrate that a $BaCe_{0.8}Gd_{0.2}O_{3-\delta}$ based membrane/catalyst system can achieve excellent carbon resistance at low O_2/CH_4 ratios, and high and stable selectivity (over 80%) to C_{2+} products (ethane, ethylene, propane and propylene). Our analysis of the system suggests that its high carbon resistance is due to its relatively high oxygen storage/release capacity which suppresses carbon deposition in the system.

4.2 Introduction

Oxidative Coupling of Methane (OCM) is a chemical transformation that converts methane directly into ethane and ethylene (C_2). This reaction occurs at ~ 600-900°C on several heterogeneous oxide catalysts, albeit with limited C_2 product yields. The main issue is that at near stoichiometric feed ratios (O_2/CH_4 ratio ~ 0.5), where the reaction is typically performed, the C_2 product selectivity is limited as thermodynamically stable over-oxidation products, such as CO and CO_2 (CO_x), are formed at the expense of the C_2 products.[1] Figure 4.1a shows the equilibrium distribution of carbon-containing products as a function of the O_2/CH_4 feed ratio at 1073K and 1atm, calculated by minimizing the Gibbs free energy of the system. The data show that the thermodynamically favored product at near stoichiometric feed ratios is CO, and this changes to CO_2 as the O_2/CH_4 ratio increases. The unselective reactions that lead to the formation of CO_x often proceed through chemical pathways that include direct gas-phase reactions of hydrocarbon radicals and O_2 as shown in Figure 4.1b.[2,3]

To overcome this challenge of low C_2 selectivity and yield, it has been proposed that solid oxide membranes are applied in combination with catalysts to deliver oxygen to the active site in a more controlled way.[1,4,5] In these membrane/catalyst systems, methane and an oxygen-containing stream (e.g., air) are separated by a dense (non-porous) oxide membrane which conducts O^{2-} from the oxygen-side of the membrane to the methane-side where the reaction occurs.[6–10,11] The membrane also conducts electrons in the opposite direction to O^{2-} for charge neutrality (Figure 4.1c).[12,13] In this system, since the lattice oxygen species in the membrane are utilized as the main source of reactive oxygen, the local partial pressure of gas phase O_2 on the methane side is low

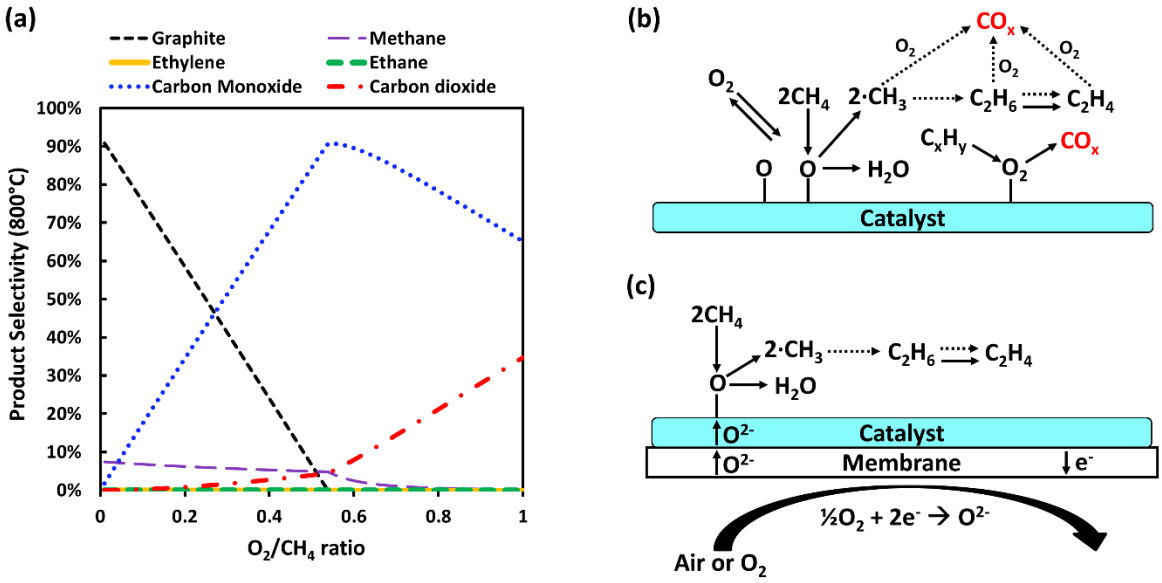

Figure 4.1. (a) Plot of thermodynamic carbon-containing product selectivity (obtained by minimizing Gibbs free energy) as a function of the O_2/CH_4 feed ratio at 800°C and 1atm. Simplified mechanism for OCM on a (b) catalyst co-fed with methane and oxygen (c) catalyst coupled with a solid oxide membrane. Dashed lines represent gas-phase reactions

(and can approach zero) limiting the rates of formation of undesired CO_x products. Additional benefits of these membrane/catalyst systems include: (1) better control of reactor temperature i.e., minimizing hot-spots which are typically formed due to high rates of deep oxidations reactions and (2) simultaneous OCM and separation of pure oxygen from nitrogen and other components in air, thereby simplifying potential downstream separation of valuable C_2 products.

While this membrane/catalyst system seems promising, it introduces other set of technical challenges that need to be addressed. One critical challenge is that due to relatively low partial pressure of oxygen (low oxygen to hydrocarbon ratio), these membrane systems promote higher carbon deposition rates on the surface of the membrane/catalyst on the methane side. The data in Figure 4.1a shows that the thermodynamically favored product in the limit of low O_2/CH_4 ratios is solid carbon. This solid carbon poisons the membrane/catalyst material, leading to a reduction in the performance over time.[14,15] Identifying membrane/catalyst systems that can conduct O^{2-} ions

and concurrently retain high carbon tolerance and C_{2+} selectivity when operating under high methane concentration is a critical challenge that needs to be addressed. We note that the challenge of carbon deposition has often been neglected in previous OCM literature since the primary issue in conventional co-fed packed bed reactor systems, operating near stoichiometric feed ratios, is to minimize overoxidation to CO_x. On the other hand, in membrane/catalyst systems, which operate at very low gas-phase O_2/CH_4 ratios, an additional challenge of minimizing carbon deposition is critical. To avoid this issue of carbon deposition, previous OCM studies in membrane/catalyst systems have typically employed heavily diluted methane feed streams ($\leq$ 0.1 bar of methane).[7–10] However, this approach is commercially impractical as it exacerbates downstream separation costs.

Herein, we have investigated selected button-shaped membrane/catalyst systems in OCM. Our goal was to evaluate the OCM performance of these systems at high methane concentrations (low oxygen to hydrocarbon ratios). A thin porous layer of same or similar composition as the membrane, but of higher surface area to volume ratio, was coated on one side of each membrane to act as the OCM catalyst. Specifically, we studied a $BaCe_{0.8}Gd_{0.2}O_{3-\delta}$ (BCG) membrane coated with BCG catalyst (BCG/BCG), a $BaCe_{0.4}Zr_{0.4}Gd_{0.2}O_{3-\delta}$ (BCZG) coated with BCZG catalyst (BCZG/BCZG) and a Ni doped $La_{0.8}Sr_{0.2}Ga_{0.8}Mg_{0.2}O_{3-\delta}$ (LSGM) membrane coated with LSGM catalyst (Ni-LSGM/LSGM). We chose to study these materials (BCG, BCZG and LSGM) because they emerged as promising membrane and catalyst candidates from previous packed bed reactor screening studies in our group.[16,17] We note that the membrane portion of the LSGM system was doped with Ni to ensure its mixed ion and electron conductivity, since LSGM by itself is a poor electron conductor.[17,18]

Our results demonstrate that the BCG/BCG system exhibits high C_2 selectivity and relatively stable OCM performance in the limit of high methane concentration. On the other hand, the Ni-LSGM/LSGM system exhibits an anticipated behavior that plagues most membrane materials, characterized by a decline in performance over time due to carbon-induced membrane/catalyst deactivation. Our analysis of the chemical characteristics of both membrane materials suggest that the high carbon resistance of the BCG catalyst is related to its relatively high surface reducibility and oxygen storage/release capacity which suppresses carbon deposition on the catalyst surface. We also show that the BCZG/BCZG system exhibits significantly lower and almost negligible oxygen flux compared to the BCG/BCG system. The reduced oxygen flux was attributed to a reduction in the electron conductivity of the BCZG membrane due to the presence of the Zr dopant.[19]

4.3 Experimental

4.3.1 Membrane fabrication and catalyst addition

LSGM was doped with 15 mol% of Ni to improve its mixed ion and electronic conductivity.[18] The Ni doped LSGM (Ni-LSGM) powder was synthesized by mixing NiO (Alfa Aesar) and LSGM (Sigma Aldrich) powder in a weight ratio of 0.28:5 using a mortar and pestle. The mixture was then calcined in air at 1000°C for 6 hours using ramp rates of 2 °C/min. BCG and BCZG powder were synthesized using a modified pechini method described in our previous work.[16] A measured amount of the sifted powder (Ni-LSGM, BCG or BCZG) was pressed into pellets in a 15 mm die press. After pressing, the pellets were placed on a zirconia plate covered with powder bath of the same composition as the pellets to minimize contamination and Ba evaporation from the BCG and BCZG pellets during sintering.[20,21] The BCG and BCZG pellets were sintered in air at 1650°C for 5 hours, while the Ni-LSGM pellets were sintered in air at

1450°C for 4 hours, using ramp rates 1 °C/min. The sintered pellets (membranes) were ~ 10 mm in diameter. To add the porous catalyst layers to the membranes, LSGM, BCG or BCZG powder was mixed with graphite powder in a 3:1 ratio using a mortar and pestle. 0.2 g of the mixture was mixed with 600 µL of ethanol to form a suspension. 25 µL of the suspension was drop-coated on one side of the membrane and air-dried. The coated membranes were calcined in air at 1150°C for 2 hours (for the Ni-LSGM membrane) and 1500°C for 4 hours (for the BCG and BCZG membrane) at ramp rates of 2°C/min to burn off graphite and create a porous catalyst layer adhered to the membrane surface.

4.3.2 Membrane and catalyst characterization

4.3.2.1 X-ray diffraction (XRD)

XRD was used to determine the crystalline phases present in the membranes and catalysts. The XRD patterns were collected at room temperature using a Rigaku MiniFlex 600 spectrometer (Cu Kα source, λ = 1.54059 Å). A continuous scan mode was used to collect 2Θ data with a step size of 0.02°and speed of 2°/min. The tube voltage and current were set at 40kV and 15mA, respectively. Phases were identified with the aid of JADE software.

4.3.2.2 Scanning Electron Microscopy (SEM) and Energy Dispersive X-ray Spectroscopy (EDS)

The membranes and catalysts were examined by SEM and EDS to evaluate the morphology, thickness, composition and interaction between membrane and catalyst layers. SEM images were collected using a Tescan MIRA3 microscope. The images were collected at an accelerating voltage of 5 – 12 kV and working distance of 8 – 15 mm. The device was equipped with an EDAX detector and TEAM software which were used for EDS measurements. The EDS elemental maps were collected at an accelerating voltage of 12 kV, working distance of 15 mm, dwell time of 200 µs, and resolution of 256 x 200 pixels. A drift corrected mode was used during

mapping to minimize effect of sample drifting. Samples were sputtered with gold beforehand to minimize charging during image collection.

4.3.2.3 Raman spectroscopy

Raman spectra was collected at room temperature using a Horiba LabRAM HR system. The membrane with coated catalyst was placed on a flat transparent holder with the catalyst side facing upwards. A 532 nm green excitation laser (at 50% intensity) was focused on the catalyst surface while been monitored with the aid of a microscope. The spectra were collected at a constant laser power.

4.3.2.4 H_2-TPR measurements

The H_2-TPR experiments were conducted using a Micrometrics Autochem II 2920 equipped with a thermal conductivity (TCD) detector and a mass spectrometer. Prior to the tests, the catalysts were calcined at the same temperature used to adhere the catalyst to the membranes (i.e., 1150°C for LSGM and 1500°C for BCG). ~0.5g of each catalyst was loaded in a U-shaped quartz tube, pretreated at 200°C for 30 minutes under 50 ml/min flow of helium, then cooled back down to 30 °C. Afterwards, the sample were heated at 10°C/min to 1000°C under a 5% H_2 in Argon stream at a flow rate of 50 L/min. The H_2O signal at the outlet of the reactor was monitored by the mass spectrometer.

4.3.3 Membrane reactor set-up and testing

A schematic of the button membrane reactor set-up is shown in Figure 4.2. Membranes were sealed to the top of an alumina tube (12.7 mm OD and 9.5 mm ID) using a combination of glass and ceramic sealants with the porous catalyst layer facing downwards. The alumina tube containing the sealed membrane was oriented vertically over a quartz tube (6.35 mm OD and 4 mm ID) in a furnace. The furnace was heated to 880°C at a ramp rate of 1°C/min under helium

flow. High purity gases purchased from Cryogenic Gases were used in the experiments. The gases were supplied to the reactor through mass flow controllers (Cole-Parmer). For the oxygen permeation measurements, 50 cm^3/min of air or a mixture of oxygen and nitrogen was fed from the top through a larger quartz tube (19 mm OD and 17 mm ID) to the membrane region and 5 cm^3/min of helium was fed from the bottom through the smaller quartz tube towards the porous catalyst side of the membrane. Note that all flow rates reported here are given at standard conditions (STP). For the OCM performance measurements, 5 cm^3/min of methane (containing 5% helium) was fed from the bottom through the smaller quartz tube and 50 cm^3/min of air was fed on the opposite side. Temperature was monitored by a thermocouple placed next to the membrane region. The effluent gases flow down the alumina tube to an Agilent 7890B GC equipped with two thermal conductivity (TCD) detectors and a flame ionization detector (FID) for analysis. The GC was calibrated beforehand using certified gas mixtures.

The oxygen flux (J_{O2}) was calculated using Equation 4.1**,** where y_{O2} is the concentration of oxygen permeated, F_e is the total exit flow rate and A_{eff} is the effective membrane surface area**.** y_{O2} was calculated using an oxygen mole balance. A_{eff} is calculated as the geometric surface area (πr^2) of the membrane exposed to the methane stream which was estimated to be ~ 0.7 cm^2. Sealing can be a problem with button-shaped membranes especially due to their relatively high

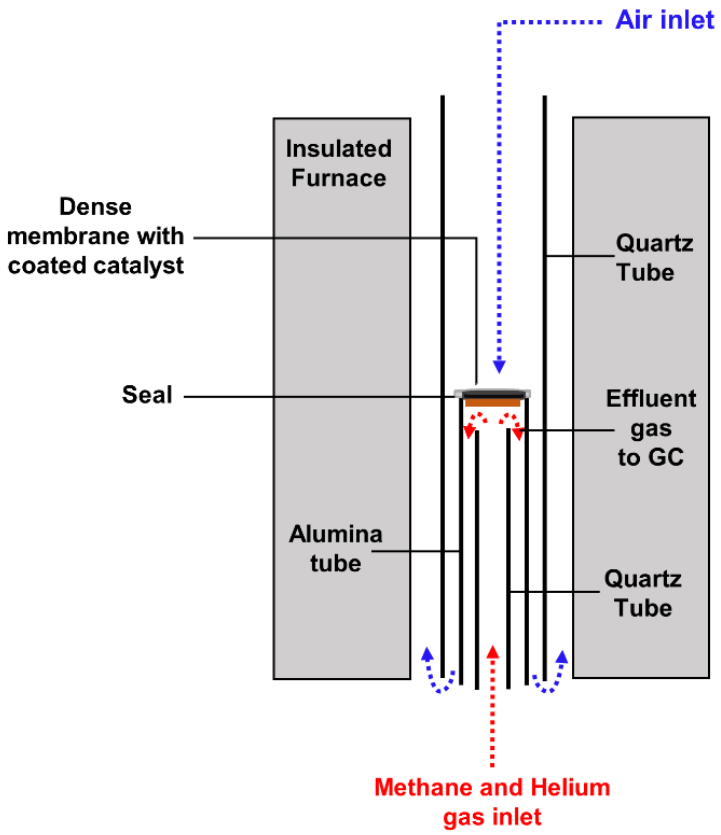

Figure 4.2. Schematic of experimental set-up for button membrane reactor

sealing/membrane area ratio. The amount of leak in the reactor can be determined by monitoring the N_2 concentration in the outlet stream. In our tests, the molar fraction of N_2 in the outlet stream was typically very low ($\leq$ 0.3%). Therefore, any O_2 leaked into reactor is considered negligible compared to the O_2 permeated though the membrane.

$$J_{O_2}\ (\mu\text{mol}\ cm^{-2}min^{-1}) = \frac{y_{o_2}F_{exit}\ (\mu mol/min)}{A_{eff}\ (cm^2)} \tag{4.1}$$

CH_4 conversion (%) and C_{2+} selectivity (%) were calculated using Equations 4.2 and 4.3.[17] The CH_4 conversion rate (in μmol cm^{-2} min^{-1}) was calculated using Equation 4.4, where X_{CH4} is the CH_4 conversion (in fraction) and F_{CH4in} is the flow rate of methane in the inlet stream.

$$X(\%) = \frac{moles\ of\ methane\ consumed}{moles\ of\ methane\ fed} \times 100 \tag{4.2}$$

$$S(\%) = \frac{[2(moles\ of\ C_2H_4 + C_2H_6\ ) + 3(moles\ of\ C_3H_6 + C_3H_8)]_{products}}{moles\ of\ methane\ consumed} \times 100 \tag{4.3}$$

$$\mathrm{CH_4\ conversion\ rate\ (\mu mol}\ cm^{-2}min^{-1}) = \frac{X_{CH_4}F_{CH_4in}(\mu mol/min)}{A_{eff}\ (cm^2)} \tag{4.4}$$

4.4. Results and Discussion

Cross-section and surface SEM micrographs of as-synthesized LSGM, BCG and BCZG membrane/catalyst systems are shown in (Figure 4.3). The images show that the membranes are dense with only a few isolated pores. The cross-section micrographs also show that all three membranes are ~500 μm thick while the porous catalyst layers are ~100 μm thick. The estimated surface area of the catalyst layers was ~80 cm^2 based on a catalyst weight of ~2 mg and the measured BET surface area of ~ 4 m^2/g.[16,17] Note that the actual active surface area of the catalyst layers is expected to be lower than this value due to partial sintering of the layers to the membranes at the high calcination temperatures (> 1000°C) required for adhesion. Energy Dispersive Spectroscopy (EDS) maps of La and Ni at the interface of Ni doped LSGM (Ni-LSGM) membrane and LSGM catalyst suggests that there was no migration of Ni from the membrane to the catalyst layer during synthesis and testing (Figure 4.4a-d). X-ray diffraction (XRD) patterns from the membranes (Figure 4.5a) also confirmed that they have the desired perovskite structures with no

significant secondary crystalline phases. The diffraction pattern from the Ni-LSGM membrane shows no significant peak corresponding to that of NiO (also shown in Figure 4.5a), which suggests that Ni was either incorporated into the perovskite lattice and/or highly dispersed within the membrane.

The data in Figure 4.5b shows the oxygen flux from the Ni-LSGM/LSGM, BCG/BCG and BCZG/BCZG system as a function of temperature. The oxygen flux from all three membranes increases with increasing temperature which is expected as the oxygen ion transport is thermally activated. The oxygen flux follows the order BCG > Ni-LSGM > BCZG. In particular, the oxygen flux from BCZG was significantly lower compared to BCG. We hypothesize that the lower oxygen flux from BCZG in part due to its lower electronic conductivity compared to BCG. Electron conduction in doped barium cerate/zirconate systems has been linked to a reduction of the Ce ions present from +4 to +3 oxidation state at high temperatures.[19,22] Therefore, partial substitution of Ce by Zr in the BCZG membrane could have led to a significant reduction in the electronic conductivity and therefore the oxygen flux. The surface SEM image of the BCZG membrane (Figure 4.3i) also shows that it has smaller grain size in comparison to that of BCG (Figure 4.3f). This indicates that the BCZG membrane has a higher grain boundary volume fraction than the BCG membrane and therefore may possess higher grain boundary resistance to the transport of oxygen ions.[23] Due to the low oxygen flux from the BCZG/BCZG system, the remainder of this study was focused on the BCG/BCG and Ni-LSGM/LSGM system.

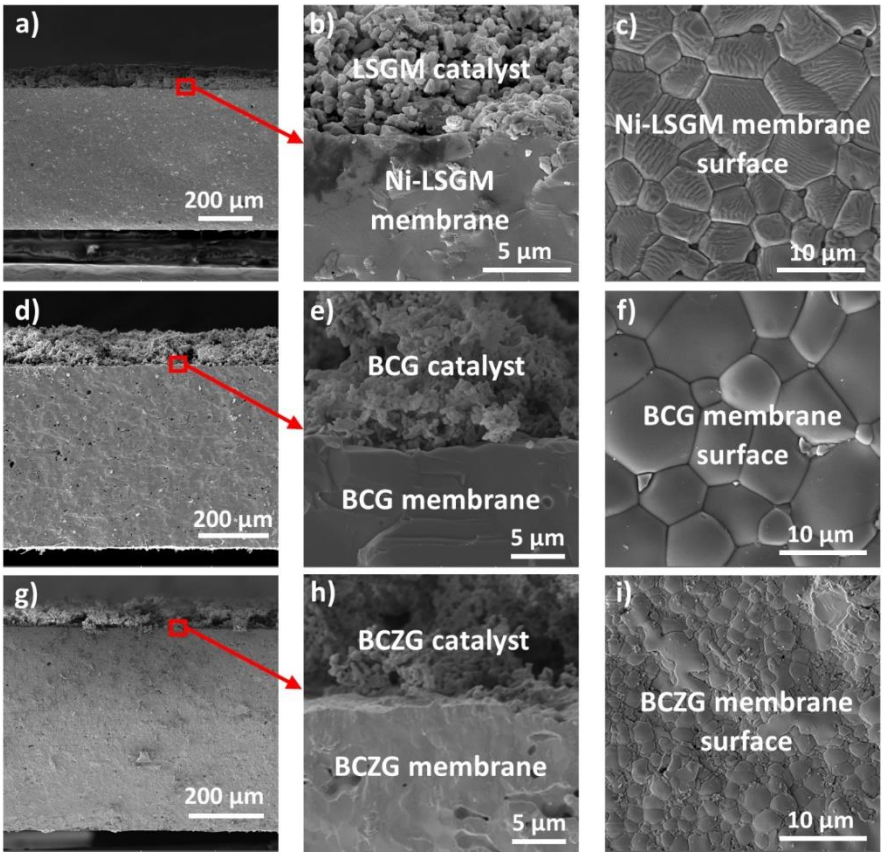

Figure 4.3. Cross-section and surface SEM micrographs of synthesized LSGM, BCG and BCZG membrane/catalyst systems.

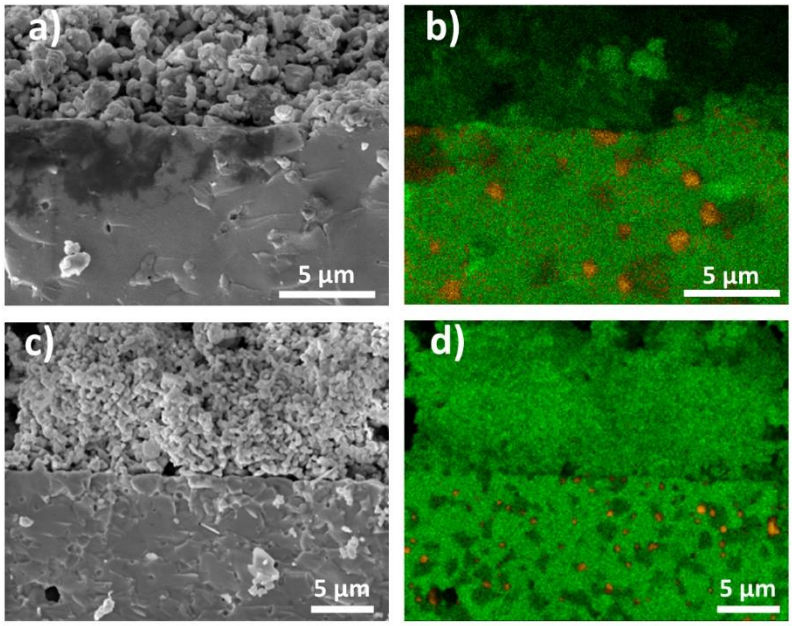

Figure 4.4. SEM images and corresponding EDS maps of La (green) and Ni (yellow) at the interface of (a,b) as-synthesized and (c,d) reacted Ni-LSGM membrane and LGSM catalyst.

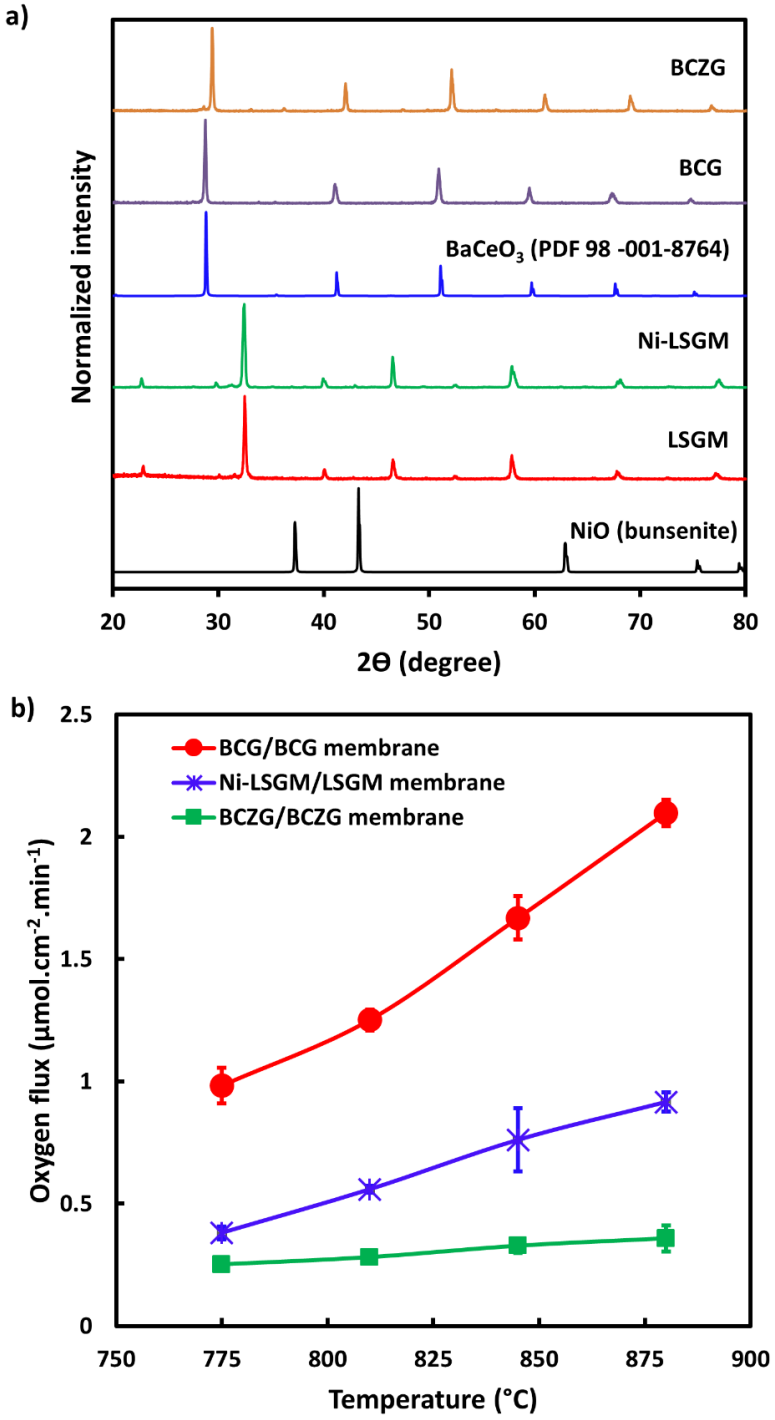

Figure 4.5. a) XRD patterns from as-sintered membranes and NiO b) Oxygen flux from Ni-LSGM/LSGM, BCG/BCG and BCZG/BCZG membrane systems as a function of temperature

The data in Figure 4.6a and b show the methane conversion rate (in μmol cm^{-2} min^{-1}) and C_{2+} selectivity as a function of time measured for the Ni-LSGM/LSGM and BCG/BCG membrane/catalyst system (C_{2+} includes propane and propylene), respectively. The reactor tests were performed at 810°C using 5 cm^3/min of 95 % CH_4 in helium on the permeate side and 50 cm^3/min of air on the opposite side of the membrane. We chose to operate our system at high partial pressures of methane (as opposed to highly diluted methane stream typically reported in the literature) since these conditions are more technologically relevant and there is a strong thermodynamic driving force to form solid carbon (Figure 4.1a). Note that due to the low membrane surface area, the percentage methane conversion in both systems was low (~ 1.4 % for the BCG/BCG and ≤ 0.5 % for the Ni-LSGM/LSGM). By operating in the differential conversion regime, we are essentially assessing the inherent propensity of the materials to form different products, including solid carbon. The data in Figure 4.6a show that the C_{2+} selectivity from the Ni-LSGM/LSGM system decreased from ~ 70% to 30% over 24 hours. Conversely, the data in Figure 4.6b show that the C_{2+} selectivity from the BCG/BCG membrane/catalyst system was relatively stable at ~ 80% over 24 hours. The data also show that, over the 24-hour period, the methane conversion rate dropped by ~ 30 % for the Ni-LSGM/LSGM membrane/catalyst, while this drop was < 10 % for the BCG/BCG system. We also tested the BCG/BCG system at similar methane conversion rates (controlled by controlling the flux of oxygen through the membrane as shown in Figure 4.6c) as the Ni-LSGM/LSGM system and found that the OCM performance of the BCG/BCG system was consistently more stable than that of the Ni-LSGM/LSGM system (Figure 4.6d).

To shed light on the observed difference in the performance of the two systems, we characterized both systems. The XRD spectra of as-synthesized and used LSGM and BCG

catalysts on respective membranes are shown in Figure 4.7a. The XRD pattern from the used LSGM catalyst shows a peak at ~ 26°, indicative of the presence of graphitic carbon. The XRD spectra from used BCG catalyst shows no detectable carbon diffraction pattern, suggesting a lower degree of carbon build-up. The data in Figure 4.7b presents the Raman spectra from as prepared and used LSGM and BCG systems**.** The spectrum from the used LSGM catalyst show peaks at approximately 1350 cm^{-1} and 1580 cm^{-1}, assigned to the D- and G-band of solid carbon, due to the stretching of the C-C bond in sp^2-bonded carbon and the presence of disorder in the carbon deposits, respectively[24]. The Raman spectrum from the used BCG catalyst has no feature corresponding to carbon.

SEM images and corresponding EDS elemental maps obtained from the catalyst surface side of the as-prepared and used Ni-LSGM/LSGM membrane/catalyst system are shown in Figure 4.8 (a,e) and 4.8(b,f), respectively. The elemental maps from the reacted catalyst show that the surface was covered with a significant amount of carbon (in red) that was absent in the unreacted catalyst. Figure 4.8(c,g) and 4.8(d,h) shows the SEM image and corresponding EDS elemental maps of the fresh and spent BCG systems. The EDS maps from the spent BCG catalyst (Figure 4.8h) does not show detectable carbon build up suggesting a lower rate of carbon deposition on this catalyst compared to the LSGM catalyst. The SEM images suggest some morphological changes in the used BCG and LSGM catalysts compared to the fresh catalysts. These changes are mainly due to the formation of new phases (e.g., carbonates and oxides) which are a common feature of the OCM process.[16,17] Raman spectrum from the reacted BCG catalyst (Figure 4.9a) also shows a new peak appearing at around 470 cm^{-1}, which indicates the presence of a CeO_2-like phase that was absent in the spectrum of the unreacted BCG catalyst (also shown in Figure 4.9a**)**. Despite

these changes in morphology, the performance of BCG with respect to both activity and selectivity is very stable over the time on stream studied.

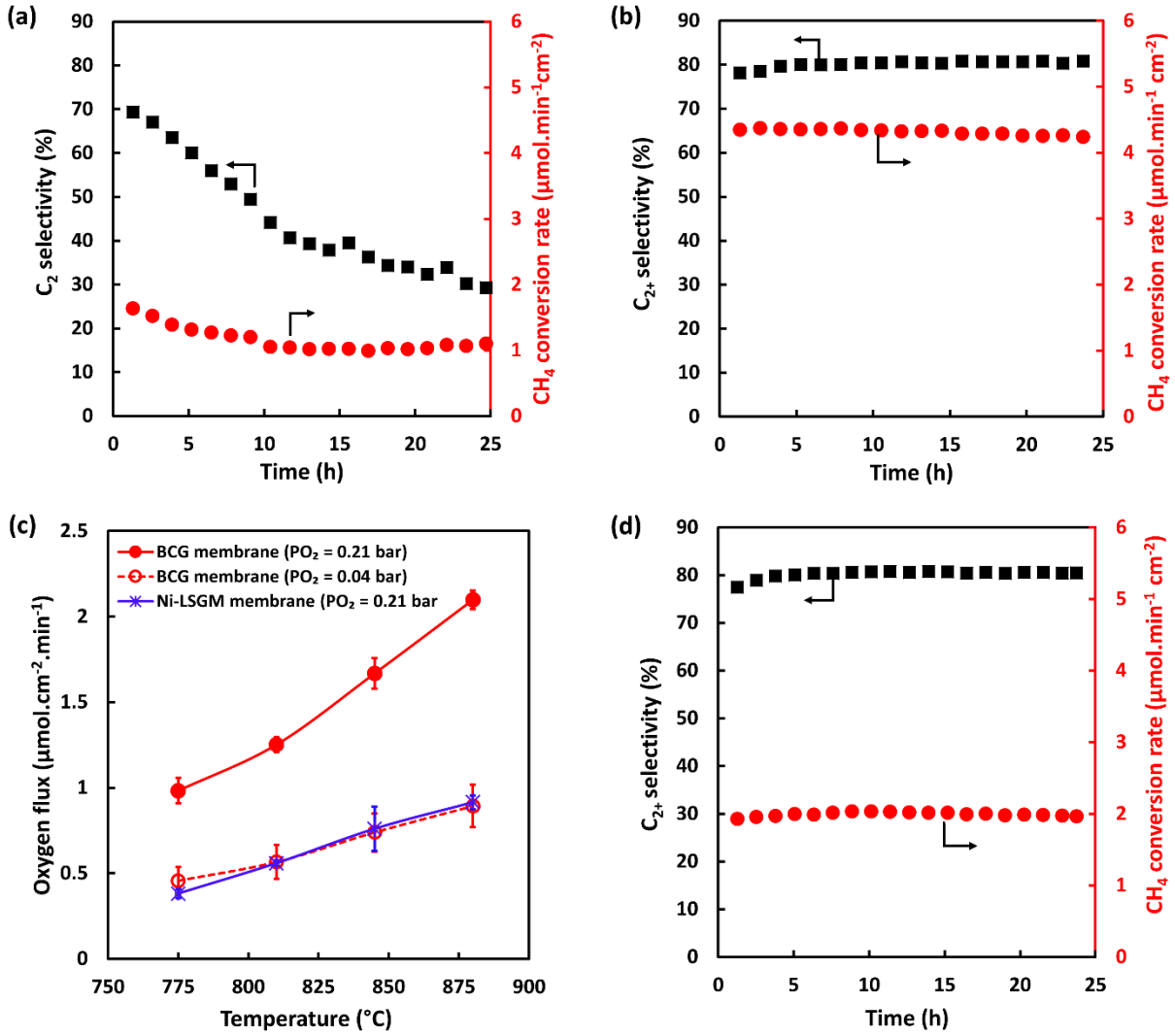

Figure 4.6. Methane conversion rate and C_{2+} selectivity over time from (a) Ni-LSGM/LSGM membrane/catalyst and (b) BCG/BCG membrane/catalyst (c) Oxygen flux through ~ 500 µm thick Ni-LSGM and BCG button membrane as a function of temperature. The oxygen flux through the BCG membrane was lowered by reducing the O_2 partial pressure on the air-side of the membrane (PO_2) from 0.21 bar to 0.04 bar (d) Methane conversion rate and C_{2+} selectivity over time from BCG/BCG membrane/catalyst at 810°C and similar oxygen flux as Ni-LSGM/LSGM membrane/catalyst.

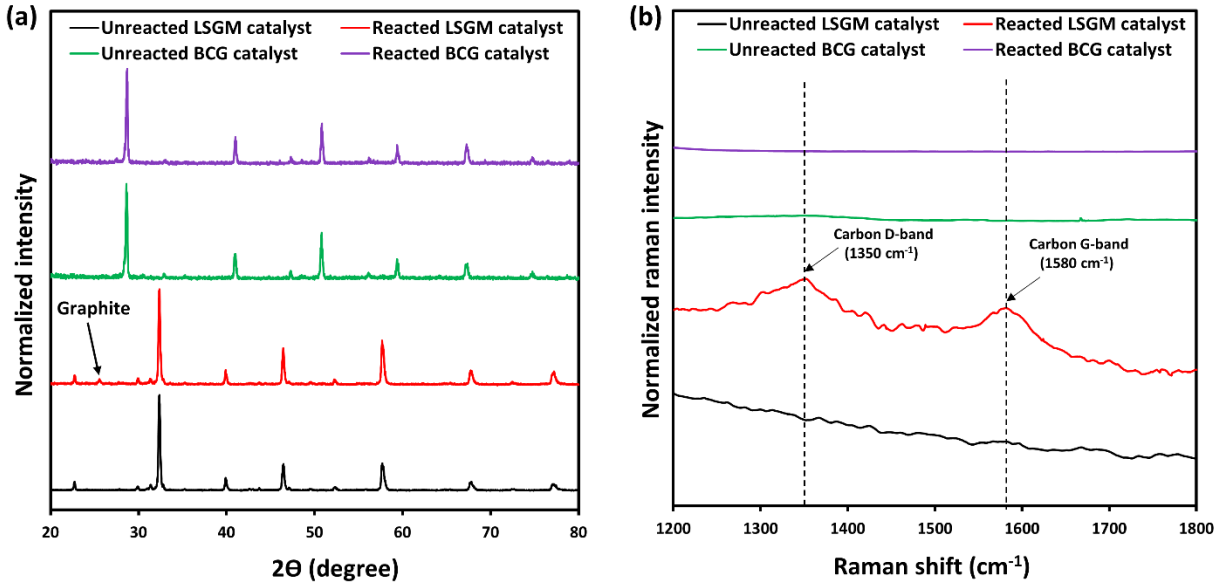

Figure 4.7. (a) X-ray diffraction patterns (b) Raman spectra, from unreacted and reacted LSGM and BCG catalyst on respective membranes.

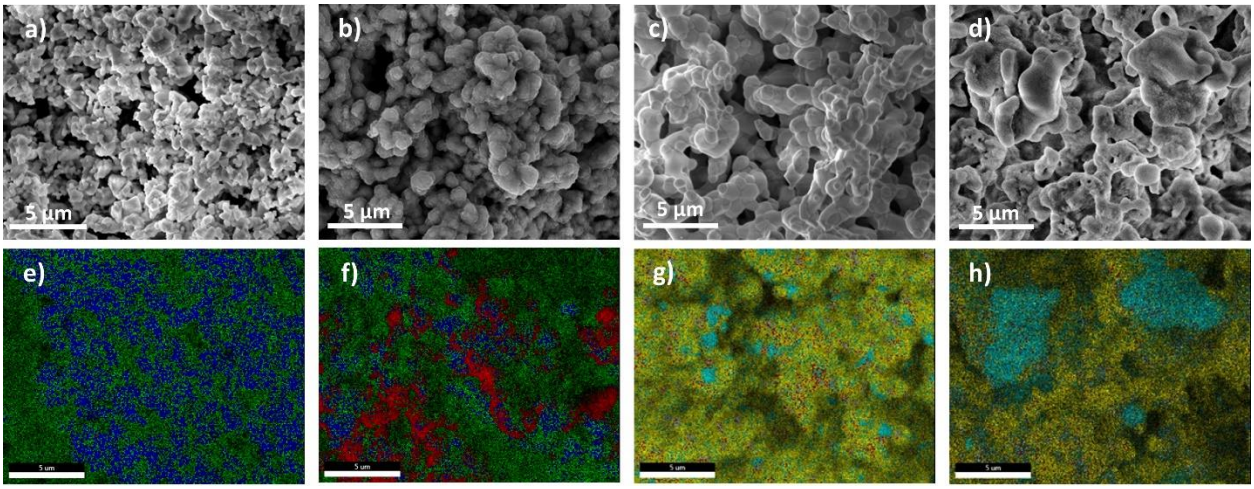

Figure 4.8. SEM images and corresponding EDS maps from the surface of (a,e) unreacted LSGM catalyst (b,f) reacted LSGM catalyst (c,g) unreacted BCG catalyst (d, h) reacted BCG catalyst, supported on respective membranes. La is depicted by light green, Ga by dark blue, Ba by cyan, Ce by yellow and carbon by red.

The characterization data from XRD, Raman spectroscopy and EDS paint a consistent picture indicating that under identical external conditions, there is a significant carbon build-up on the reacted LSGM catalyst, while BCG is less prone to the carbon deposition. Based on these data, we hypothesize that the decline in the C_{2+} selectivity and methane conversion over time, observed for the Ni-LSGM/LSGM membrane/catalyst, is due to carbon deposition on the LSGM catalyst surface. The higher carbon resistance of the BCG/BCG system prolongs the membrane/catalyst lifetime which is desired as it allows for fewer regeneration cycles in long-term (e.g., commercial) operations. We speculate that the high carbon resistance of the BCG/BCG system is related to its intrinsic oxygen storage/release capacity (i.e., the chemical potential of oxygen in the surface layers of the material). We note that oxygen suppresses carbon deposition on the catalyst surface as these highly chemically active oxygen atoms serve to oxidize carbon deposits before they can nucleate and grow on the catalyst surface.

One measure of this oxygen storage/release capacity is the reducibility of the material. We have conducted H_2-Temperature Programmed Reduction (TPR) studies on the BCG and LSGM catalyst powders (using ~ 0.5 g of each) to compare their relative reducibilities. Figure 4.9b shows H_2-TPR profiles obtained from the BCG and LSGM catalysts. The data for the BCG sample show a peak around 330°C and a larger broader peak around 560°C. The H_2-TPR profile for the LSGM sample shows smaller peaks around 340°C and 610°C. A comparison of the H_2-TPR peak intensities from BCG and LSGM catalysts in Figure 4.9b suggests that for the same amount of material, the H_2 consumption by the BCG catalyst is overall larger than the LSGM catalyst indicating higher storage of available O^{2-} in BCG. In addition, the lower reduction temperatures for BCG compared to LSGM suggests that the BCG catalyst is more reducible than the LSGM catalyst, i.e., it binds the reactive oxygen atoms with a lower interaction energy. This essentially

means that the oxygen stored in BCG is more chemically reactive that that stored in LSGM. Note that the BET surface areas of both catalyst powders are very similar (< 4 m^2/g), therefore the differences observed cannot be attributed to differences in surface area. Another manifestation of the intrinsic oxygen storage/release capacity is the oxygen permeation flux through the membranes**.** The resistance to oxygen ion transport appears to be higher in the Ni-LSGM membrane as evidenced by its lower oxygen flux compared to the BCG membrane at similar operating conditions (Figure 4.6c**)**. This result is consistent with the H_2-TPR data which shows a lower capacity of LSGM to store and release oxygen compared to BCG.

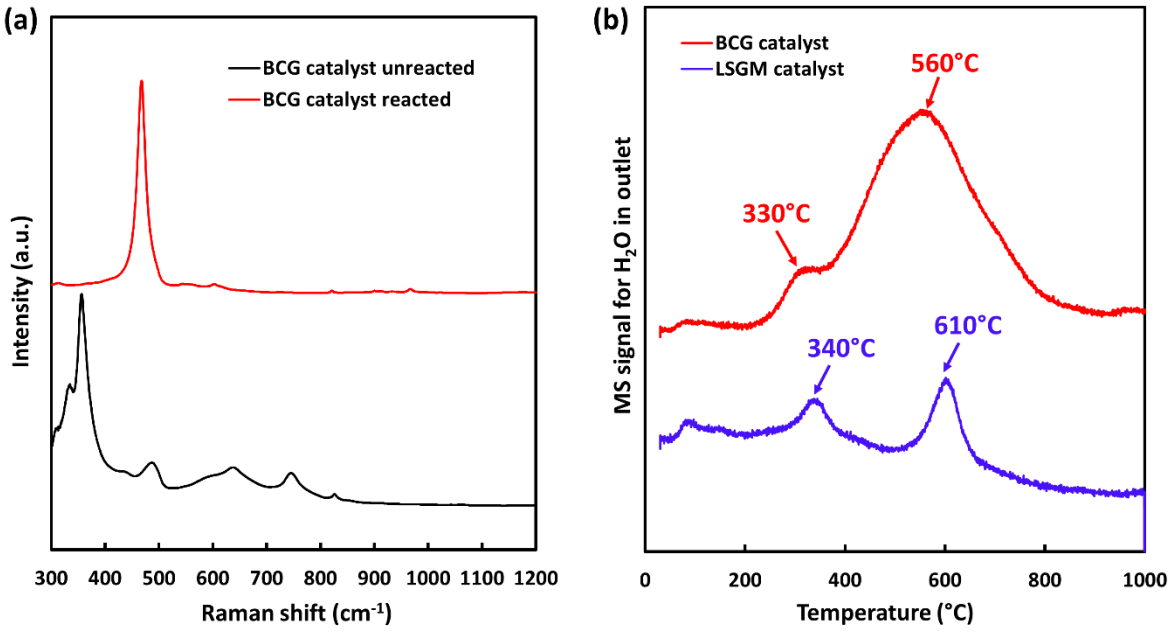

Figure 4.9. (a) H_2-TPR profiles from LSGM and BCG catalyst (b) Oxygen flux through ~ 500 µm thick Ni-LSGM/LSGM and BCG/BCG button membrane as a function of temperature.

4.5 Conclusions

We have tested BCG/BCG, BCZG/BCZG and Ni-LSGM/LSGM membrane/catalyst systems to evaluate their OCM performance at high methane concentrations. We discovered that

the BCG/BCG membrane system exhibits more stable C_{2+} selectivity compared to the Ni-LSGM/LSGM system. Characterization data confirmed the presence of significant amount of carbon deposits on the reacted LSGM catalyst and negligible amounts on the reacted BCG catalyst (supported on respective membranes). We hypothesize that the decline in C_{2+} selectivity over time from the Ni-LSGM/LSGM system is due to a higher carbon deposition rate compared to the BCG/BCG system. We attribute the higher carbon tolerance of the BCG/BCG system to a higher oxygen storage/release capacity of the BCG material compared to LSGM. We also found that the BCZG/BCZG system gives significantly lower oxygen flux compared to the BCG/BCG system. We hypothesize that the lower oxygen flux from BCZG is related to a reduction in its electron conductivity compared to BCG due the presence of the Zr dopant.

4.6 References

(1) Farrell, B. L.; Igenegbai, V. O.; Linic, S. A Viewpoint on Direct Methane Conversion to Ethane and Ethylene Using Oxidative Coupling on Solid Catalysts. *ACS Catal.* **2016**, *6* (7), 4340–4346.

(2) Lane, G. S.; Wolf, E. E. Methane Utilization by Oxidative Coupling: I. A Study of Reactions in the Gas Phase during the Cofeeding of Methane and Oxygen. *J. Catal.* **1988**, *113* (1), 144–163.

(3) Luo, L.; You, R.; Liu, Y.; Yang, J.; Zhu, Y.; Wen, W.; Pan, Y.; Qi, F.; Huang, W. Gas-Phase Reaction Network of Li/MgO-Catalyzed Oxidative Coupling of Methane and Oxidative Dehydrogenation of Ethane. *ACS Catal.* **2019**, *9* (3), 2514–2520.

(4) Eng, D.; Stoukides, M. Catalytic and Electrocatalytic Methane Oxidation with Solid Oxide Membranes. *Catal. Rev.* **1991**, *33* (3–4), 375–412.

(5) Wang, B.; Albarracín-Suazo, S.; Pagán-Torres, Y.; Nikolla, E. Advances in Methane Conversion Processes. *Catal. Today* **2017**, *285*, 147–158.

(6) Tan, X.; Pang, Z.; Gu, Z.; Liu, S. Catalytic Perovskite Hollow Fibre Membrane Reactors for Methane Oxidative Coupling. *J. Membr. Sci.* **2007**, *302* (1), 109–114.

(7) Tan, X.; Li, K. Oxidative Coupling of Methane in a Perovskite Hollow-Fiber Membrane Reactor. *Ind. Eng. Chem. Res.* **2006**, *45* (1), 142–149.

(8) Lu, Y.; Dixon, A. G.; Moser, W. R.; Ma, Y. H.; Balachandran, U. Oxygen-Permeable Dense Membrane Reactor for the Oxidative Coupling of Methane. *J. Membr. Sci.* **2000**, *170* (1), 27–34.

(9) Othman, N. H.; Wu, Z.; Li, K. A Micro-Structured $La_{0.6}Sr_{0.4}Co_{0.2}Fe_{0.8}O_{3-\delta}$ Hollow Fibre Membrane Reactor for Oxidative Coupling of Methane. *J. Membr. Sci.* **2014**, *468*, 31–41.

(10) Akin, F. T.; Lin, Y. S. Oxidative Coupling of Methane in Dense Ceramic Membrane Reactor with High Yields. *AIChE J.* **2002**, *48* (10), 2298–2306.

(11) Xu, S. J.; Thomson, W. J. Stability of $La_{0.6}Sr_{0.4}Co_{0.2}Fe_{0.8}O_{3-\delta}$ Perovskite Membranes in Reducing and Nonreducing Environments. *Ind. Eng. Chem. Res.* **1998**, *37* (4), 1290–1299.

(12) Mukherjee, J.; Linic, S. First-Principles Investigations of Electrochemical Oxidation of Hydrogen at Solid Oxide Fuel Cell Operating Conditions. *J. Electrochem. Soc.* **2007**, *154* (9), B919–B924.

(13) Ingram, D. B.; Linic, S. First-Principles Analysis of the Activity of Transition and Noble Metals in the Direct Utilization of Hydrocarbon Fuels at Solid Oxide Fuel Cell Operating Conditions. *J. Electrochem. Soc.* **2009**, *156* (12), B1457–B1465.

(14) ten Elshof, J. E.; Van Hassel, B. A.; Bouwmeester, H. J. Activation of Methane Using Solid Oxide Membranes. *Catal. Today* **1995**, *25* (3–4), 397–402.

(15) Zeng, Y.; Lin, Y. S.; Swartz, S. L. Perovskite-Type Ceramic Membrane: Synthesis, Oxygen Permeation and Membrane Reactor Performance for Oxidative Coupling of Methane. *J. Membr. Sci.* **1998**, *150* (1), 87–98.

(16) Igenegbai, V. O.; Meyer, R. J.; Linic, S. In Search of Membrane-Catalyst Materials for Oxidative Coupling of Methane: Performance and Phase Stability Studies of Gadolinium-Doped Barium Cerate and the Impact of Zr Doping. *Appl. Catal. B Environ.* **2018**, *230*, 29–35.

(17) Farrell, B. L.; Linic, S. Oxidative Coupling of Methane over Mixed Oxide Catalysts Designed for Solid Oxide Membrane Reactors. *Catal. Sci. Technol.* **2016**, *6*, 4370–4376.

(18) Ishihara, T.; Ishikawa, S.; Hosoi, K.; Nishiguchi, H.; Takita, Y. Oxide Ionic and Electronic Conduction in Ni-Doped $LaGaO_3$-Based Oxide. *Solid State Ion.* **2004**, *175* (1), 319–322.

(19) Dippon, M.; Babiniec, S. M.; Ding, H.; Ricote, S.; Sullivan, N. P. Exploring Electronic Conduction through $BaCe_xZr_{0.9-x}Y_{0.1}O_{3-d}$ Proton-Conducting Ceramics. *Solid State Ion.* **2016**, *286*, 117–121.

(20) Ricote, S.; Bonanos, N. Enhanced Sintering and Conductivity Study of Cobalt or Nickel Doped Solid Solution of Barium Cerate and Zirconate. *Solid State Ion.* **2010**, *181* (15), 694–700.

(21) VahidMohammadi, A.; Cheng, Z. Fundamentals of Synthesis, Sintering Issues, and Chemical Stability of $BaZr_{0.1}Ce_{0.7}Y_{0.1}Yb_{0.1}O_{3-\delta}$ Proton Conducting Electrolyte for SOFCs. *J. Electrochem. Soc.* **2015**, *162* (8), F803–F811.

(22) Kruth, A.; Davies, R. A.; Islam, M. S.; Irvine, J. T. S. Combined Neutron Diffraction and Atomistic Modeling Studies of Structure, Defects, and Water Incorporation in Doped Barium Cerate Perovskites. *Chem. Mater.* **2007**, *19* (6), 1239–1248.

(23) Wang, B.; Bi, L.; Zhao, X. S. Exploring the Role of NiO as a Sintering Aid in $BaZr_{0.1}Ce_{0.7}Y_{0.2}O_{3-\delta}$ Electrolyte for Proton-Conducting Solid Oxide Fuel Cells. *J. Power Sources* **2018**, *399*, 207–214.

(24) S. Blinn, K.; Abernathy, H.; Li, X.; Liu, M.; A. Bottomley, L.; Liu, M. Raman Spectroscopic Monitoring of Carbon Deposition on Hydrocarbon -Fed Solid Oxide Fuel Cell Anodes. *Energy Environ. Sci.* **2012**, *5* (7), 7913–7917.

Chapter 5

Enhancing Selectivity in Oxidative Coupling of Methane Using Tubular Catalytic Solid Oxide Membrane Reactors

5.1 Summary

The oxidative coupling of methane (OCM) is a promising route for the direct conversion of methane (the principal component of natural gas) to higher value C_2 hydrocarbons (ethylene and ethane). The main challenge with this process is the formation of undesired by-products (CO and CO_2) from over-oxidation reactions, which limits the C_2 product selectivity. This selectivity problem is particularly significant in conventional reactors, where methane and oxygen are co-fed, due to the presence of high gas-phase O_2 concentrations at the reactor inlet that accelerates the over-oxidation reactions. To overcome this challenge, catalytic solid oxide membrane reactors have been proposed as an alternative to co-fed reactors. The membrane reactors allow the delivery of oxygen-ions (O^{2-}) to the catalytically active sites in a distributed and controlled manner, thereby reducing the gas-phase O_2 concentration in the reactor, which should limit the occurrence of over-oxidation reactions. In this work, catalytic $BaCe_{0.8}Gd_{0.2}O_{3-\delta}$ (BCG) tubular membranes were synthesized via a combination of slip-casting and solid-state reactive sintering (using Cu as a sintering additive) and tested in OCM. The Cu modified BCG (Cu-BCG) membrane reactor achieved a methane conversion of ~ 6% and a C_{2+} selectivity of ~ 65% at 845°C. The Cu-BCG membrane reactor also achieved significantly higher C_{2+} selectivity (≥ 14% increase) compared to a co-fed reactor at similar methane conversions. This finding provides conclusive evidence of the

improved OCM performance of a catalytic membrane reactor over a conventional co-fed reactor. However, stability studies revealed that the methane conversion from the Cu-BCG membrane reactor declined over time. The decline in catalytic activity of the Cu-BCG membrane was attributed to phase changes occurring on the membrane surface under the operating conditions.

5.2 Introduction

The increase in the supply of low-cost natural gas from unconventional sources (e.g., shale oil and gas reserves) in the United States is causing a shift from petroleum to natural gas as the main source of hydrocarbon feedstock for the chemical industry.[1] Methane (the principal component of natural gas) is industrially converted to value-added chemicals such as methanol and higher hydrocarbons via technologies requiring an intermediate syngas (CO, H_2) production step.[2,3] However, the high cost associated with these technologies indicate that they benefit from economies of scale and are not suitable for small-scale operations. Since it is expensive to transport the "stranded" natural gas from small-scale sources, they are typically flared or vented. This practice does not only lead to the waste of a valuable resource but also contributes towards the emission of deleterious greenhouse gases. Therefore, the desire for modular upgrading technologies that are applicable to stranded natural gas is a major driver for the development of direct methane conversion routes.[3–5]

The oxidative coupling of methane (OCM) is a promising route for the direct conversion of methane to higher value C_2 hydrocarbons such as ethylene and ethane. This process occurs at high temperatures (600-900°C) in the presence of oxygen and an active catalyst.[6] The widely proposed mechanism for OCM begins with the abstraction of hydrogen from methane by a surface oxygen specie to form methyl radicals. The methyl radicals are released to the gas-phase where they couple to form ethane, which can be further dehydrogenated into ethylene.[7–9] The main

challenge with OCM is that the C_2 selectivity is limited due to the formation of thermodynamically favored over-oxidation products, CO and CO_2 (CO_x). This problem is particularly significant in conventional OCM reactors where methane and oxygen are co-fed at the reactor inlet.[10] Since the total oxygen amount is fed together with methane, co-fed reactors enable high concentrations of gas-phase O_2 at the reactor inlet. The gas-phase O_2 reacts with hydrocarbon radicals to form CO_x, which limits the overall C_2 selectivity.[11]

An approach to overcome this challenge is to utilize catalytic solid oxide membrane reactors where a dense (non-porous) perovskite membrane separates the methane from the oxygen feed. The membrane allows the selective conduction of O^{2-} (lattice oxygen) from the oxygen side of the membrane to the methane side where the reaction occurs.[10,12] In this system, the lattice oxygen species are delivered to the active sites in a distributed and controlled manner. Therefore, gas-phase oxygen concentration on the methane-side is considerably minimized which should limit the rates of CO_x product formation.[10] The membrane reactors offer additional benefits including better control of reactor temperature (due to reduced rates of exothermic over-oxidation reactions) and simultaneous separation of pure oxygen from other components in the air, thereby simplifying downstream separation and enabling process intensification.

Although solid oxide membrane reactors offer several advantages, there are relatively few experimental studies of these membrane reactors in OCM.[13–18] Moreover, studies on the long-term performance and phase stability of the membrane reactors in OCM are limited.[18] In this work, we fabricate $BaCe_{0.8}Gd_{0.2}O_{3-\delta}$ (BCG) tubular membranes via a combined slip-casting and solid-state reactive sintering (SSRS) method, using Cu as a sintering additive. The Cu-modified BCG (Cu-BCG) tubular membrane was studied in OCM to evaluate the impact of changing the mode of feeding oxygen (distributed versus co-fed) and the stability of the membrane reactor overtime on

stream. Our results show that significantly higher C_{2+} selectivity can be achieved from membrane reactor operation (distributed oxygen feed) compared to the co-fed operation of the Cu-BCG membrane, at similar methane conversions. Additionally, we show that the OCM performance of the membrane reactor declines slightly over time which we attribute to phase changes occurring on the membrane surface under operating conditions.

5.3 Experimental

5.3.1 Membrane fabrication

Dead-end BCG tubular membranes were fabricated by slip-casting and solid-state reactive sintering using Cu (4 mol %) as a sintering additive.[19,20] The materials used for fabrication include barium carbonate ($BaCO_3$, Alfa Aesar, 99.8%), cerium (IV) oxide (CeO_2, Alfa Aesar, 99.9%), gadolinium (III) oxide (Gd_2O_3, Alfa Aesar, 99.9%), copper (II) oxide (CuO, Sigma Aldrich, 98%), gum arabic (The Ceramic Shop), gypsum powder (Blick Art Materials), α-terpineol (Acros Organics, 97+%), ethyl cellulose (Sigma Aldrich, 48% ethoxyl), and graphite (Alfa Aesar, 75-micron size). The slip-casting process is illustrated in Figure 5.1.

The plaster mold was fabricated from a mixture of gypsum powder and water in a 1:1 weight ratio. The mixture was poured into a cylindrical container and degassed under vacuum for 5 minutes. After degassing, a glass test-tube was inserted in the center of the mixture avoiding contact with the bottom of the container. The test-tube was removed when the mixture was partially solidified leaving behind a hollow in the mold. After complete solidification, the mold was removed from the container and dried at 50°C.

To prepare the slurry for slip-casting, stoichiometric amounts of BCG precursors ($BaCO_3$, CeO_2 and Gd_2O_3) were ball milled in ethanol for 24 hours and then dried under stirring. A separate solution was prepared by dissolving gum arabic (as a binder) in deionized water. The ball-milled

BCG precursor and CuO (0.82 g per 100 g of BCG precursor) was added to the binder solution and stirred for ~10 minutes. The weight ratio of the binder: precursor powder: water used in the slurry was 1:9:45. The prepared slurry was poured into a dry plaster mold. Water in the slurry was absorbed by the mold leaving a solid layer of BCG precursor, CuO and binder. The slurry was poured in continuously maintaining a constant level at the top surface of the mold. After a total casting time of 5 minutes, the excess slurry was decanted. The solid layer (casted tube) shrank while drying and was carefully removed from the mold. The casted tube was sintered at 1450°C for 5 hours using ramp rates of 1°C/min. Figure 5.2 shows representative images of the slip-casted Cu-BCG precursor tubes (~14 mm ID, 16 mm OD and 10 cm in length) and the sintered Cu-BCG tubular membranes (~10 mm ID, 11 mm OD and 6 cm length) on the left and right, respectively. The linear shrinkage of the tubes upon sintering was ~ 40%.

The inner surface of some tubular membranes was coated with a catalyst slurry composed of BCG powder (sifted to < 75 μm size), ethanol, graphite, and binder (6wt% ethyl cellulose in terpineol). The BCG powder was prepared by solid-state reaction where a stoichiometric amount of $BaCO_3$, CeO_2 and Gd_2O_3 were ball milled in ethanol for 24 h, dried than calcined at 1350°C for 10 hours. The weight ratio of binder: graphite: BCG powder: ethanol in the slurry was 4:7:21:80. Prior to coating the inner surface, the outer surface of the tubular membrane was wrapped in Teflon tape to minimize contamination. The slurry was sonicated for 10 minutes to disperse the solids and then poured into the tubular membrane. After approximately 5 s, the slurry was decanted, and the tube was dried at 70°C for 10 minutes. The coating process was repeated 10 times to increase the thickness of the catalyst layer. The coated membrane was then dried and calcined at 900°C for 2 hours (ramp rate 1.5°C/min) to adhere the catalyst layer to the membrane. The final thickness of the coated catalyst layer was 25 – 50 μm as determined by SEM imaging.

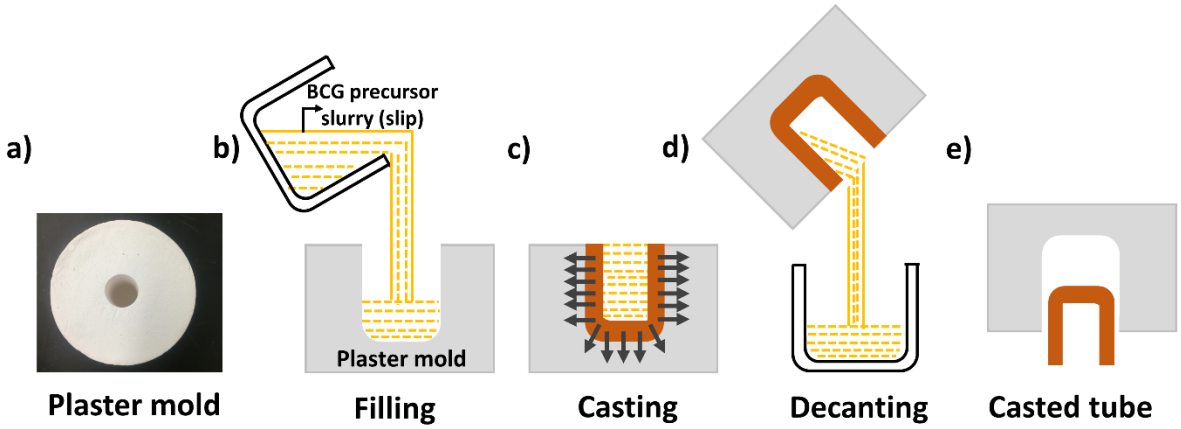

Figure 5.1. Five consecutive steps involved in slip casting: (a) a plaster mold is prepared from a mixture of gypsum plaster and water; (b) the dry mold is filled with slurry composed of chemical precursors and water; (c) the mold extracts water from the slurry forming a solid layer of precursor on the wall of the mold; (d) excess slip is decanted from the mold; (e) solid layer or casted tube is removed from mold after partial drying.

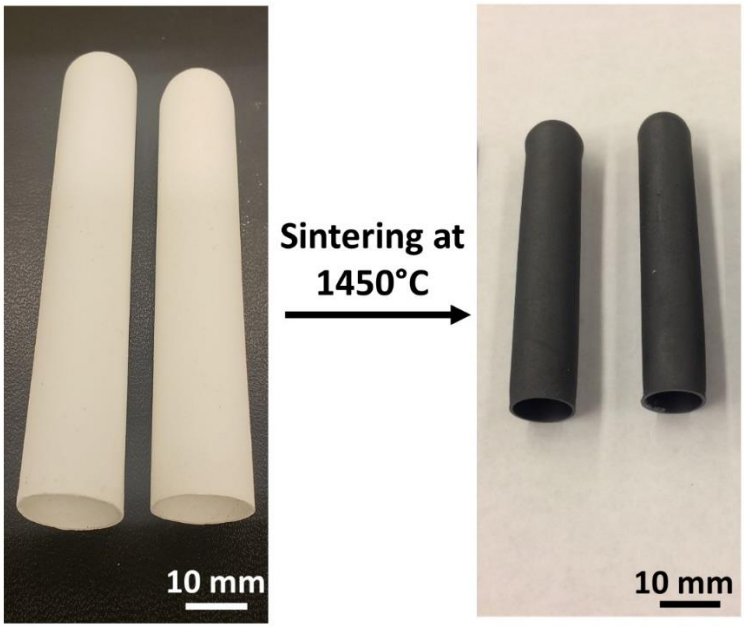

Figure 5.2. Representative pictures of the slip-casted Cu-BCG precursor tubes and the sintered Cu-BCG tubular membranes on the left and right, respectively

5.3.2 Membrane characterization

The tubular membranes were characterized by X-ray diffraction (XRD) to determine the crystalline phases present. The XRD measurements were obtained at room temperature with a Rigaku MiniFlex 600 spectrometer using a Cu Kα (λ =1.54059 Å) radiation source and operating at a tube voltage and current of 40kV and 15mA, respectively. The patterns were recorded at 2θ angles from 20 to 80 in a continuous scan mode at a speed of 2°(2Θ) per minute and a step width of 0.02°.

Scanning electron microscopy (SEM) was used to evaluate the morphology and thickness of the tubular membranes. The SEM micrographs were obtained using a Tescan MIRA3 FEG microscope. The membranes were fractured to obtain relatively flat pieces of samples that were attached to SEM sample stubs (using double-sided copper tape) for imaging. The samples were also sputter-coated with a thin layer of gold to minimize charging during imaging. Energy Dispersive X-ray Spectroscopy (EDS) analysis of the samples was achieved using an EDAX detector (with TEAM software) that was connected to the SEM microscope. EDS elemental maps were collected at an accelerating voltage of 12kV, a working distance of 15 mm, dwell time of 200 µs and a frame size of 256 x 200 pixels. Drift corrected mode was applied to minimize the effect of sample drift during mapping.

5.3.3 Membrane reactor set-up and testing

A diagram of the tubular membrane reactor is shown in Figure 5.3a. The open-end of the membrane was attached to the top of an alumina tube (12.7 mm OD and 9.5 mm ID) using a combination of glass and ceramic sealants. After drying the sealant, the alumina tube with the attached membrane was inserted into an insulated furnace and heated under helium flow to 880°C

at a ramp rate of 1°C/min. The inlet flow rate of the gases was controlled using mass flow controllers (Cole Parmer).

For oxygen permeation tests, 100 cm^3/min of O_2 and N_2 mixture was supplied from the top through a large quartz tube (19 mm OD and 17 mm ID) to one side of the membrane (referred to as the shell-side) and 40 cm^3/min of helium was fed on the opposite side through an inner quartz tube (6.35 mm OD and 4 mm ID) that extended towards the dead-end of the membrane (referred to as tube-side) as shown in Figure 5.3a. For the OCM experiments, 20 cm^3/min of methane (containing 5% helium) diluted with an additional 20 cm^3/min of helium were fed on the tube-side while 100 cm^3/min of O_2 and N_2 mixture was fed on the shell-side. This results in an inlet methane partial pressure (P_{CH4}) of ~ 0.5 bar. The methane stream flows down the annular region between the tubular membrane and the inner quartz tube where it can react with permeated oxygen. A thermocouple was placed near the membrane to monitor the reactor temperature. The effluent gases leaving the tube-side were analyzed with an Agilent 7890B GC gas chromatograph (GC) equipped with two thermal conductivity detectors (TCD) and a flame ionization detector (FID) . For comparison, co-fed reactor experiments were performed where methane, oxygen and helium were all fed to the tube-side while pure nitrogen was supplied to the shell-side of the membrane (Figure 5.3b). The flow rate of methane and helium into the co-fed reactor was the same as the membrane reactor i.e., 20 cm^3/min of methane (containing 5% helium) diluted with an additional 20 cm^3/min of helium. All flow rates reported here are given at standard conditions (STP).

The oxygen flux (J_{O_2}) through the membranes was calculated using Equation 5.1**,** where y_{O_2} is the concentration of permeated oxygen, F_{exit} is the total exit flow rate and A_{eff} is the effective permeation area of the tubular membrane**.** y_{O_2} was calculated by application of mole balance on oxygen and A_{eff} was estimated to be approximately 15 cm^2. In all tests, the amount of N_2 detected

in the effluent gas was low (< 0.2%). This indicates that the amount of oxygen that leaked into the system from the air-side is negligible and does not affect the performance evaluation.

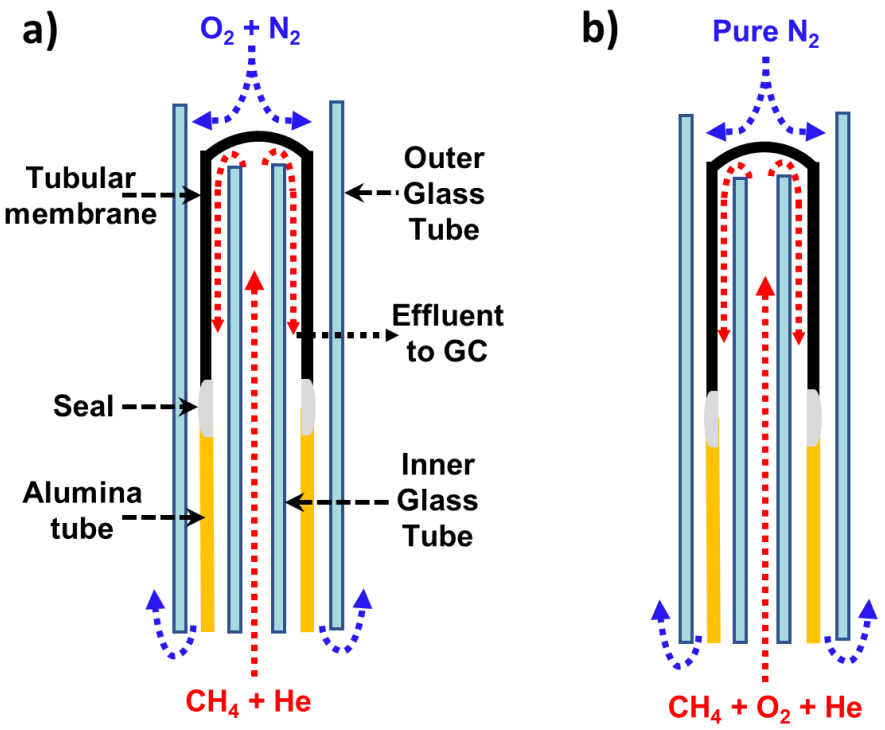

Figure 5.3. Reactor set-up (a) membrane reactor (b) co-fed reactor

$$J_{O_2}\ (\mu\text{mol}\ cm^{-2}min^{-1}) = \frac{y_{O_2} F_{exit}\ (\mu mol/min)}{A_{eff}\ (cm^2)} \tag{5.1}$$

CH_4 conversion (%), C_{2+} selectivity (%) and C_{2+} yield (%) were calculated using Equations 5.2, 5.3 and 5.4, respectively. In membrane reactor operation, the methane conversion was varied by changing the oxygen partial pressure on the shell-side of the membrane ($P_{O_{2,s}}$) from 0.21 to 1 bar while keeping the total flow rate constant at 100 cm^3/min. By varying $P_{O_{2,s}}$, the driving force for oxygen transport through the membrane (i.e., the oxygen partial pressure difference across the

membrane) is altered, which changes the oxygen flux. In the co-fed operation, methane conversion was varied by changing the flow rate of pure oxygen co-fed with methane from 0.6 – 1 cm^3/min.

$$X(\%) = \frac{moles\ of\ methane\ consumed}{moles\ of\ methane\ fed} \times 100 \tag{5.2}$$

$$S(\%) = \frac{[2(moles\ of\ C_2H_4 + C_2H_6\ ) + 3(moles\ of\ C_3H_6 + C_3H_8)]_{products}}{moles\ of\ methane\ consumed} \times 100 \tag{5.3}$$

$$Y(\%) = \frac{SX}{100} \tag{5.4}$$

5.3.4 Packed bed reactor set-up and testing

Cu modified BCG (Cu-BCG) powder was tested in a conventional packed bed reactor (PBR) to evaluate its performance in comparison to that of BCG. The Cu-BCG powder was prepared by crushing and sifting Cu-BCG tubular membranes to particles 125 – 350 μm in diameter. 0.1g of the sifted powder was loaded in the middle of a 6.35 mm ID quartz tube and supported on both ends with silica wool. The loaded quartz tube was placed horizontally in an insulated furnace equipped with a thermocouple and a temperature controller. The furnace was heated under 40 cm^3/min of Argon flow to 750°C at a ramp rate of 2°C/min. At 750°C, the Argon flow was discontinued and methane (containing 5% helium) and air were fed to the reactor at a total flow rate of 100 cm^3/min. The flow rate of the methane stream was varied between 25 – 95 cm^3/min, while the air flowrate was varied between 5 – 75 cm^3/ min. The effluent gases leaving the reactor were passed through a condenser to remove water vapor and then fed to an Agilent 7890B Gas Chromatograph (GC) equipped with two thermal conductivity detectors (TCD) and a flame ionization detector (FID) for analysis. CH_4 conversion (%), C_{2+} selectivity (%) and C_{2+} yield (%) were calculated using Equations 5.2 - 5.4.

5.4 Results and Discussion

5.4.1 Characterization of fresh membranes

Figure 5.4a shows the XRD pattern from a representative Cu modified BCG (Cu-BCG) tubular membrane as well as the standard patterns for $BaCeO_3$ perovskite and CuO. The pattern for the Cu-BCG membrane shows that it had the desired perovskite structure with no secondary impurity phases. No diffraction peaks corresponding to CuO were detected in the XRD pattern of the Cu-BCG membrane. This indicates that Cu was either incorporated into the lattice of BCG or was highly dispersed within the membrane at low concentrations (4 mol% Cu) that is not detectable by the XRD.

The Cu-BCG membranes were approximately 500 μm thick as shown in the cross-section SEM image in Figure 5.4b. The SEM image of the inner (Figure 5.4c) and the outer surface (Figure 5.4d) of the membranes also show that the membranes were highly dense (non-porous). The high density of the membranes is important as it enables the selective transfer of O^{2-} across the membrane at high temperature while preventing the transfer of other components (e.g., N_2).

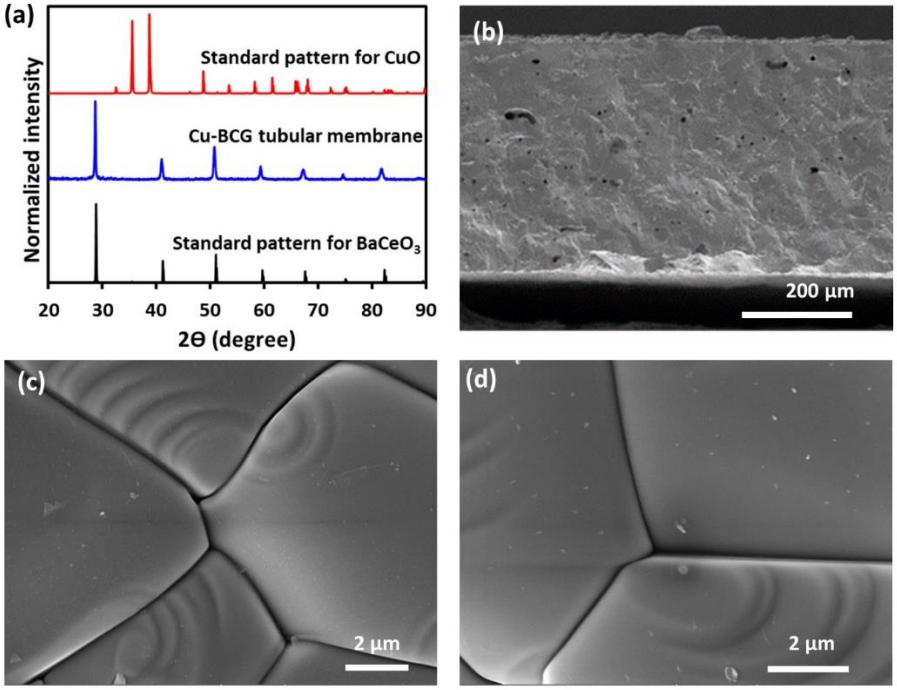

Figure 5.4. (a) XRD pattern from Cu-BCG tubular membrane and standard patterns for $BaCeO_3$ and CuO. SEM images of Cu-BCG tubular membrane showing (b) cross-section (c) inner surface and (d) outer surface

5.4.2 Membrane and co-fed reactor performance

The data in Figure 5.5a shows the C_{2+} selectivity as a function of methane conversion for the Cu-BCG membrane and co-fed reactor at 845°C. As shown in the figure, the C_{2+} selectivity from the membrane reactor was significantly higher than that from the co-fed reactor at comparable methane conversions. The membrane reactor achieves a C_{2+} selectivity of ~ 65 % at methane conversions of 5.6 – 6.5 %. On the other hand, the co-fed reactor achieves C_{2+} selectivity of 54 – 57 % at methane conversions of 5.0 – 7.0 %. The higher selectivity achieved in the membrane reactor is attributed to a decrease in the occurrence of unselective gas-phase reactions that promote the sequential conversion of the C_{2+} products to CO and CO_2 (CO_x). This result supports our overall hypothesis that improved C_{2+} selectivity is achieved in the membrane reactors compared

to the co-fed reactors due to the distributed oxygen feed resulting in lower gas-phase oxygen concentrations in the former.

The data in Figure 5.5b shows the oxygen conversion as a function of methane conversion from the membrane and co-fed reactor at 845°C. The figure shows that the oxygen conversion was ≥ 90% in both the membrane and co-fed reactor, however, oxygen conversion was lower in the membrane reactor. The apparent lower oxygen conversion in the membrane reactor is attributed to the presence of unreacted oxygen that permeated through the membrane near the reactor outlet. In other words, the oxygen that permeates near the membrane outlet has a lower probability of reacting with methane as it spends a relatively shorter amount of time in the reactor. On the other hand, the oxygen introduced in the co-fed reactor is rapidly consumed near the reactor inlet leading to nearly a 100% oxygen conversion.

Note that in the experiments described above, the Cu-BCG tubular membranes were tested in the absence of an additional catalyst layer i.e., the membrane serves a dual role as both membrane (transfers and supplies lattice oxygen) and catalyst (activates methane). To evaluate the catalytic activity of the Cu-BCG tubular membrane in the absence of an additional catalyst layer, we performed co-fed control experiments. The control experiments were performed in the absence of the Cu-BCG tubular membrane i.e., methane and oxygen were co-fed into a dead-end inert (quartz) tube instead of the tubular membrane. In these experiments, the methane feed inlet flow rate was fixed at 40 cm^3/min (P_{CH4} ~ 0.5 bar, balance helium) while the oxygen flow rate was varied between 0.6 – 1.2 cm^3/min. Figure 5.5c shows the methane conversion as a function of the oxygen concentration in the feed ($C_{O_{2,in}}$) for the co-fed reactor (i.e., with the Cu-BCG tubular membrane) and the control experiment (i.e., with the dead-end inert tube). As shown Figure 5.5c, the methane conversion from the control experiment was significantly lower than the co-fed

reactor at all $C_{O_{2,in}}$. Specifically, the methane conversion was ≤ 1.3% in the control experiment while it was ≥ 5.0% in the co-fed reactor. Figure 5.5d shows the oxygen conversion as a function of $C_{O_{2,in}}$. The data shows that the oxygen conversion was significantly lower in the control experiment compared to the co-fed reactor i.e., ≤ 22 % in the control experiment as opposed to nearly 100 % in the co-fed reactor. The minor methane and oxygen conversions obtained in the control experiment is attributed to homogenous reactions in the absence of a catalyst. The fact that the methane and oxygen conversion from the co-fed reactor is significantly higher than the control experiment confirms that the Cu-BCG membrane has considerable catalytic activity for OCM (i.e., it promotes the rates of CH_4 activation) in the absence of an additional catalyst layer.

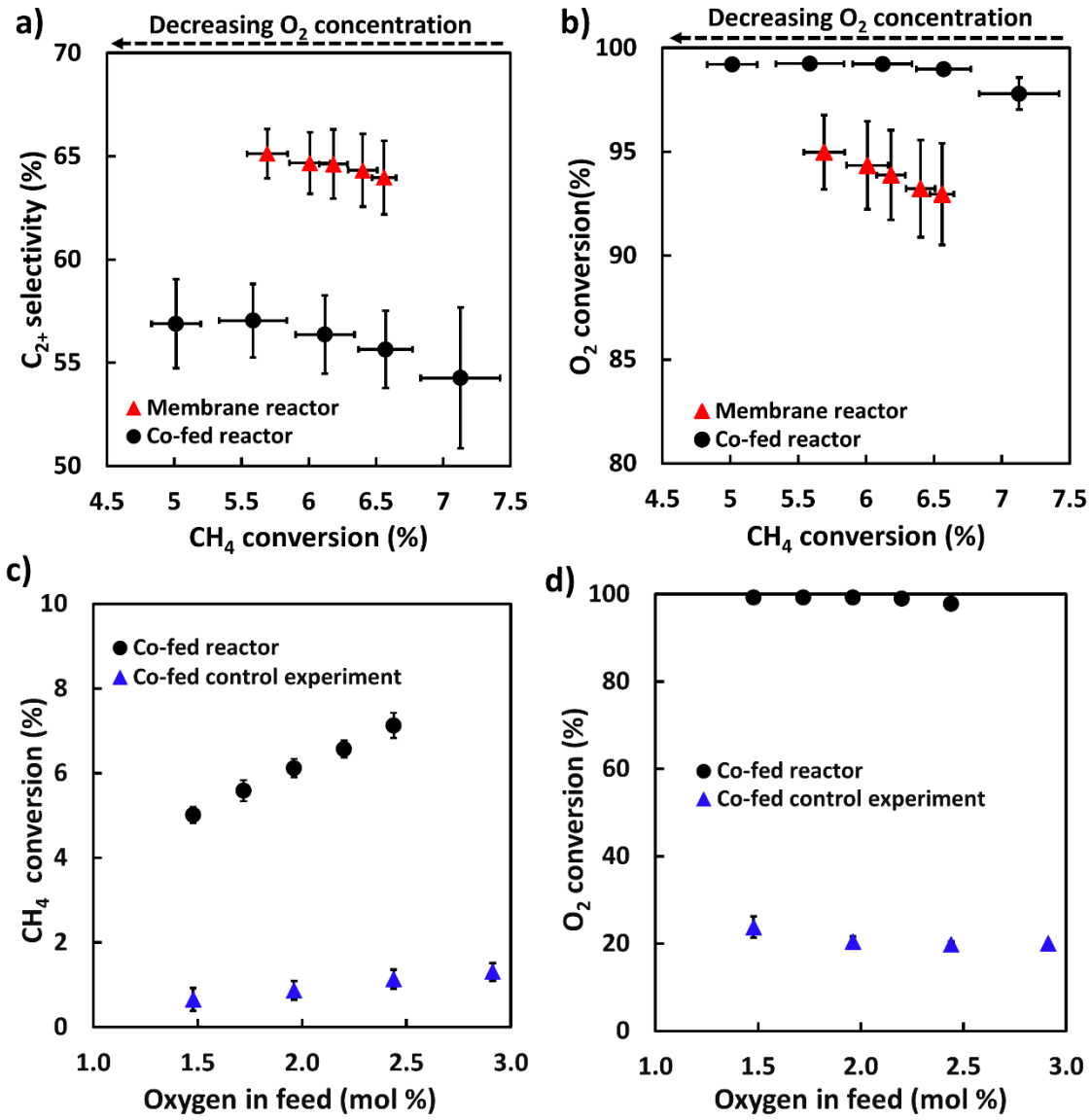

Figure 5.5. (a) C_{2+} selectivity as a function of methane conversion and (b) Oxygen conversion as a function of methane conversion from Cu-BCG membrane reactor and co-fed reactor. (c) Methane conversion as a function of the oxygen concentration in feed and (d) Oxygen conversion as a function of oxygen concentration in feed for co-fed reactor (with Cu-BCG membrane) and co-fed control experiment. The co-fed control experiments were performed using a dead-end quartz tube. All experiments were performed at 845°C.

5.4.3 Membrane stability under operating conditions

The data in Figure 5.6a show the oxygen flux from the Cu-BCG tubular membrane over 24 hours at 845°C. The data was obtained with 40 cm^3/min of helium on the tube-side and 100 cm^3/min of synthetic air (21% O_2 and 79% N_2) on the shell-side. Note that there was no methane introduced in this test. As shown in Figure 5.6a, the oxygen flux decreases from ~1.2 to 1.0 μmol. $cm^{-2}.min^{-1}$ over 24 hours on stream. This behavior is attributed to phase transformations occurring on the membrane surface at the operating condition, which will be illustrated using SEM and EDS analysis later in this section. The data in Figure 5.6b show the methane conversion and C_{2+} selectivity over time from the Cu-BCG tubular membrane when operated as a membrane reactor. This experiment was performed at 845°C with 40 cm^3/min of diluted methane feed (P_{CH4} ~ 0.5 bar, balance He) on the tube-side and 100 cm^3/min of synthetic air on shell-side of the membrane. As shown in Figure 5.6b, the methane conversion decreases from 6.1% to 5.5% over 20 hours. The decrease in methane conversion over time is attributed to a decline in the oxygen flux, which occurs even in the absence of methane as shown in Figure 5.6a. As the oxygen flux declines over time, the amount of lattice oxygen species available to activate methane also reduces, which decreases the methane conversion. The C_{2+} selectivity increases from 56% to 66% over 20 hours as shown in Figure 5.6b. The increase in C_{2+} selectivity over time is, at least in part, due to the conversion-selectivity interplay that is typical in OCM, where a decrease in the methane conversion is accompanied by an increase in the selectivity.

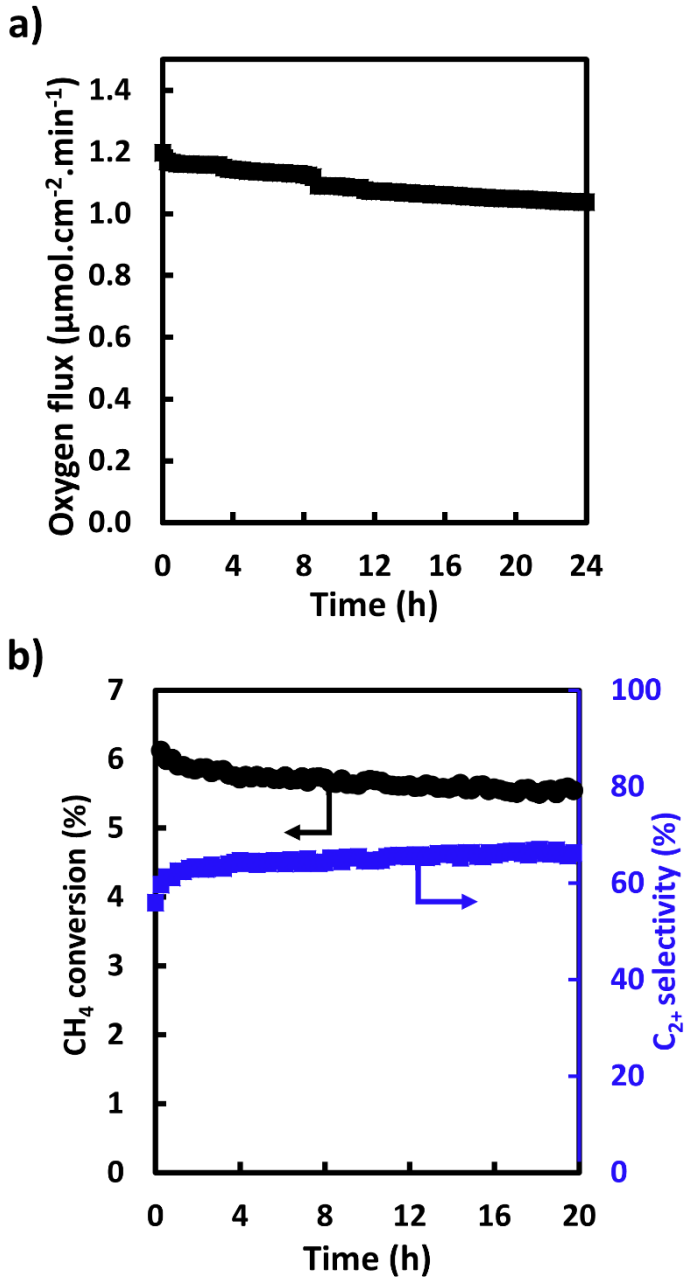

Figure 5.6. (a) Oxygen flux and (b) CH_4 conversion and C_{2+} selectivity as a function of time from Cu-BCG tubular membrane reactor. The oxygen flux measurements were obtained at 845°C using 40 cm^3/min of pure helium on the tube-side and 100 cm^3/min of synthetic air on the shell-side of the membrane. The OCM stability test was performed using 40 cm^3/min of diluted methane feed (P_{CH4} ~ 0.5 bar, balance helium) on the tube-side under the same reaction conditions.

SEM micrographs from the fresh and spent surface on the tube-side (methane-side) and shell-side (oxygen-side) of the membrane are shown in Figure 5.7. As shown in the figure, the fresh surfaces on both sides of the membrane were relatively smooth (Figure 5.7a and c). After the reaction, the surface morphology on both sides was significantly transformed as shown in Figure 5.7b and d. The spent surfaces appear to be covered with droplet-like features, which we attribute to new phases formed during the reaction. For example, new phases composed of carbonates and oxides may have been formed on the methane-side due to reaction between the BCG perovskite and CO_2.[21–23]

Figure 5.8 shows SEM images of the spent surfaces on the tube-side and shell-side of the membrane with corresponding EDS maps of barium, cerium, oxygen, and carbon. The EDS maps from the spent methane-side surface of the membrane (Figure 5.8b) show a relatively even distribution of elements despite the morphological changes in the SEM image. This indicates that there was either negligible elemental segregation or that the elemental composition of the tiny droplet-like regions was not adequately distinguished by EDS. On the contrary, the EDS maps from the spent oxygen-side surface (Figure 5.8d) show that the larger droplet-like regions in the SEM micrograph have significantly different composition compared to other regions of the membrane. The droplet-like regions appear to be mainly composed of oxygen (shown in blue). This result indicates that, at the operating conditions, the BCG perovskite phase segregated up a few μm below some regions of the membrane surface on the oxygen-side. The exact cause and composition of the new phases formed are unknown and of interest in future work. Note that similar phase transitions have been observed on the oxygen-side of state-of-the-art $Ba_{0.5}Sr_{0.5}Co_{0.8}Fe_{0.2}O_{3-\delta}$ (BSCF) perovskite membranes used in air separation leading to a steady decline in oxygen flux.[24–26]

Since the perovskite-type structure of BCG is necessary for its oxygen-ion conduction,[27] we attribute the decline in the oxygen flux from the membrane (Figure 5.6a) to phase changes that occurred over time on stream, particularly on the oxygen-side of the membrane. Note that the EDS maps from the spent membrane surface on the methane-side (Figure 5.8b) did not show any regions covered in carbon (shown in red), which suggests that there was no carbon residue on the surface after the reaction. Figure 5.9 shows the XRD pattern from the fresh and spent Cu-BCG tubular membrane. The figure shows that the spent membrane has the same XRD pattern as the fresh membrane, with no significant impurity phase. This result indicates that membranes retain the bulk perovskite structure, therefore the phase changes occurred only at the membrane surfaces under the reaction condition.

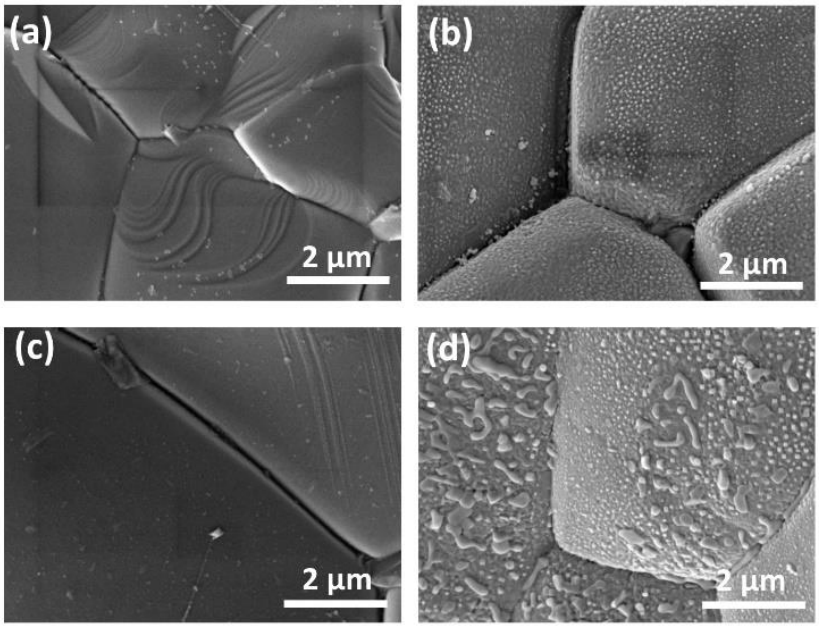

Figure 5.7. SEM images from Cu-BCG tubular membrane (a) fresh surface on tube-side (b) spent surface on tube-side (c) fresh surface on shell-side and (d) spent surface on shell-side. The tube-side was exposed to methane while the shell-side was exposed to oxygen during the OCM tests at 845 ^{o}C.

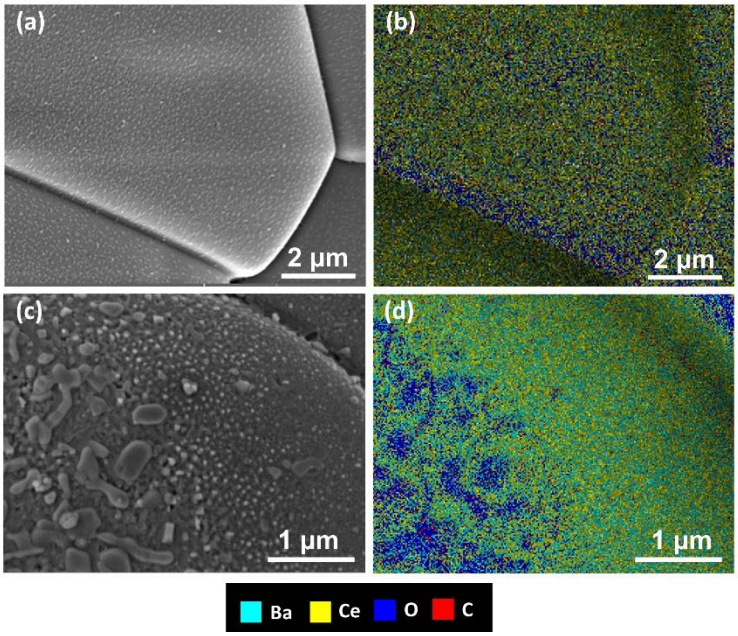

Figure 5.8. SEM images and corresponding EDS maps from spent surfaces on the tube-side (a,b) and shell-side (c,d) of the Cu-BCG tubular membrane. The tube-side was exposed to methane while the shell-side was exposed to oxygen during the OCM tests at 845 ^{o}C.

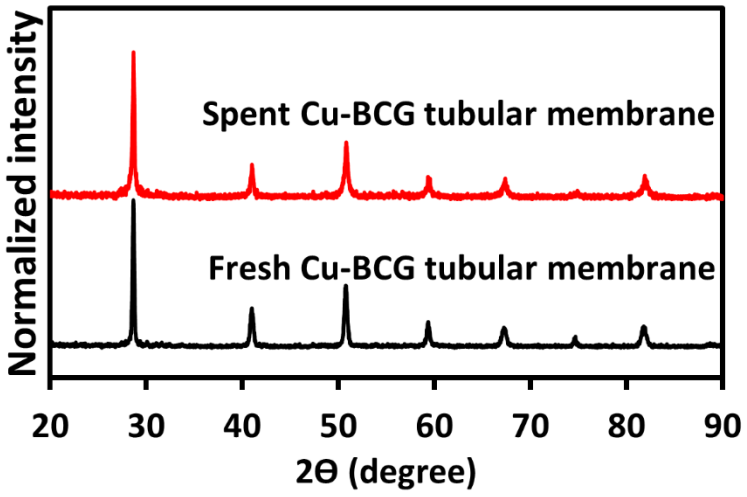

Figure 5.9. XRD patterns from fresh and spent Cu-BCG tubular membrane

5.4.4 Performance of Cu-BCG membrane powder in a packed-bed reactor

The data in **Figure 5.10** show the C_{2+} selectivity as a function of the methane conversion for the Cu-BCG powder in a packed-bed reactor at 750°C**.** The corresponding data for BCG catalyst powder tested under the same conditions is also shown in Figure 5.10.[22] Note that the oxygen partial pressure in the feed decreases from the right to the left of the figure as indicated by the arrow above the figure. The data show the typical conversion-selectivity interplay in OCM, where the C_{2+} selectivity drops as methane conversion increases due to an increase in the sequential reactions of the C_{2+} products to CO_x. The data also show that the Cu-BCG powder gives significantly lower methane conversion and C_{2+} selectivity compared to the BCG powder. Furthermore, the oxygen conversion from the Cu-BCG powder was relatively low (6 - 85%) while it was ≥ 97% from the BCG catalyst.[22] The lower methane and oxygen conversion from the Cu-BCG powder is attributed to its reduced catalytic activity caused by the presence of Cu and/or the application of a higher synthesis temperature. The Cu-BCG powder was synthesized at 1450°C (as opposed to 1000°C for BCG), therefore it is expected to have a lower surface area (due to particle sintering) and therefore lower OCM activity. The lower C_{2+} selectivity from the Cu-BCG is attributed to the presence of a transition metal (Cu) in the material. In general, oxides with transition metals give low selectivity in OCM as these metals tend to be selective for deeper oxidation of methane.[28] Note that at ~ 6% methane conversion, the C_{2+} selectivity from the Cu-BCG powder was ~ 53% as shown in Figure 5.10. These values are consistent with that obtained from the Cu-BCG tubular membrane in co-fed operation (Figure 5.5a).

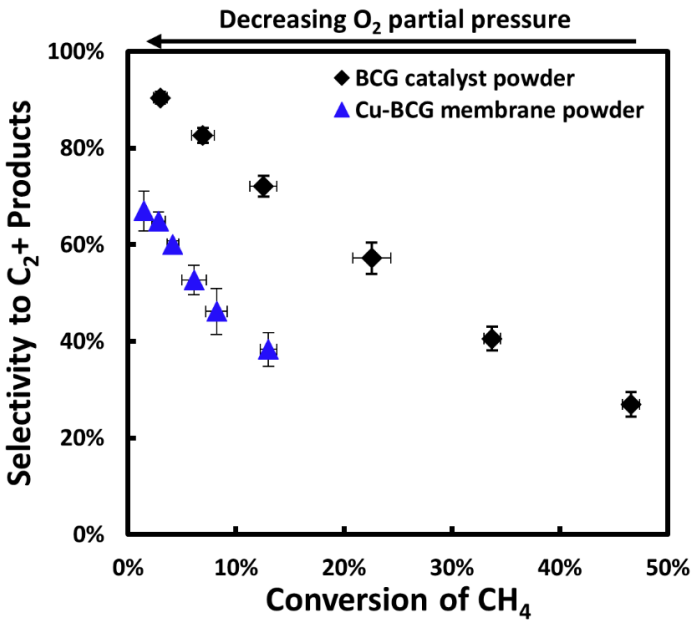

Figure 5.10. C_{2+} selectivity as a function of methane conversion from Cu-BCG membrane powder and BCG catalyst powder in a packed bed reactor at 750°C.

5.4.5 Effect of BCG catalyst coating on Cu-BCG membrane performance

As described above, the presence of Cu in the Cu-BCG membrane powder reduced its OCM performance compared to BCG. To improve the OCM performance of the Cu-BCG membrane reactor, the effect of adding a porous layer of the BCG catalyst to the inner surface (methane-side) of the membrane was investigated. The hypothesis was that the catalyst layer will provide a more active and selective surface for the OCM reaction and thereby improve the performance. Figure 5.11a-c show a cross-section SEM image and corresponding EDS elemental maps from a spent catalyst-coated Cu-BCG tubular membrane. As shown in the elemental maps**,** Cu (shown in pink) appears prominently in the BCG catalyst layer. On the other hand, the Cu in the membrane layer is well distributed and barely distinguishable from the other elements present. This data indicates that Cu migrated from the membrane to the catalyst layer presumably both during the calcination step (at 900°C) that was used to adhere the catalyst to the membrane and

during the OCM reaction (at 845°C). Figure 5.12 shows the XRD pattern from the spent BCG catalyst layer (which was carefully removed from the membrane) as well as the standard diffraction pattern for CuO. As shown in the figure, the spent catalyst layer had the desired BCG perovskite structure with no significant impurity phases. There was also no diffraction peak corresponding to CuO in the pattern from the catalyst layer which suggests that the concentration of Cu in the catalyst layer was below the detection limit of the XRD.

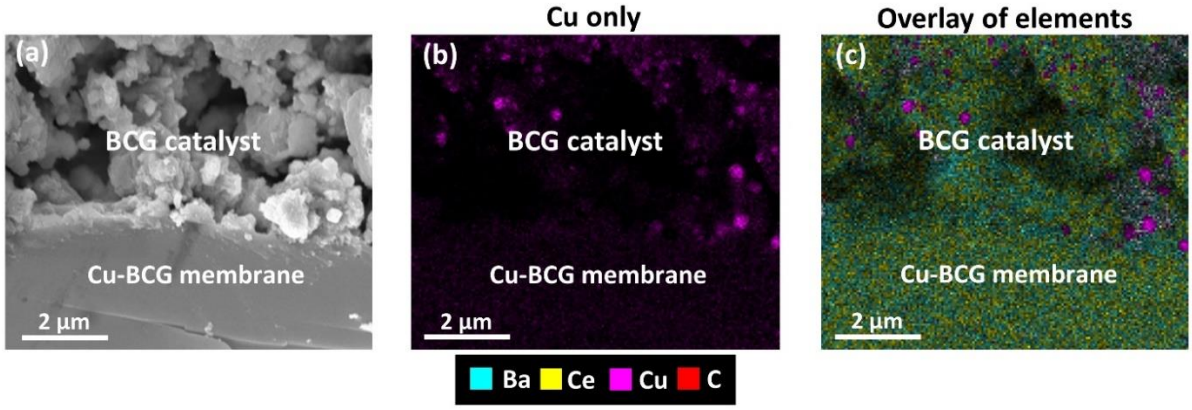

Figure 5.11. Cross-section SEM image and corresponding EDS elemental maps of spent Cu-BCG tubular membrane coated with BCG catalyst.

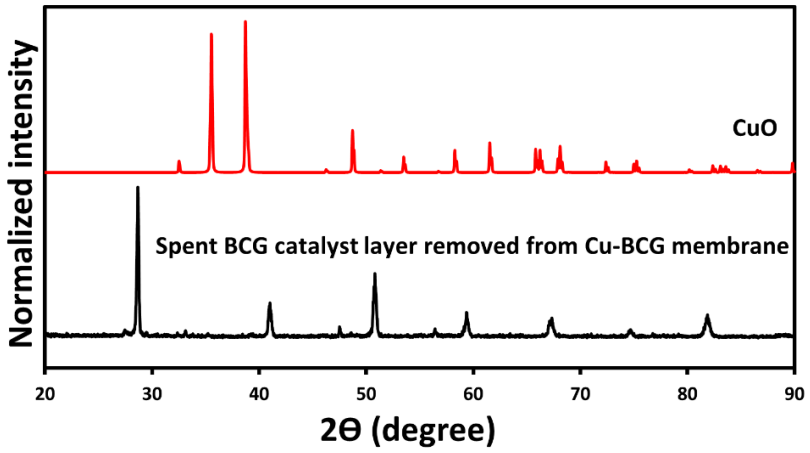

Figure 5.12. XRD pattern of the spent BCG catalyst layer that was recovered from the spent Cu-BCG membrane along with the standard diffraction pattern of CuO.

Data in Figure 5.13a show the oxygen flux from the uncoated and catalyst-coated tubular membranes. Note that this data was obtained with 40 cm^3/min of pure helium fed to the tube-side and 100 cm^3/min of synthetic air on the shell-side. The data shows that the oxygen flux from the catalyst-coated membrane was slightly lower than the uncoated membrane. We hypothesize that the catalyst layer on the coated membrane provides additional bulk-diffusion resistance to the transport of oxygen ions and thereby limits the oxygen flux. The data in Figure 5.13b show the methane conversion and C_{2+} selectivity from the uncoated and catalyst-coated membranes. The data was obtained with 40 cm^3/min of diluted methane (P_{CH4} ~ 0.5 bar, balance helium) fed to the tube-side and 100 cm^3/min of synthetic air on the shell-side As shown in the figure, the catalyst-coated membranes gave lower methane conversion and C_{2+} selectivity than the uncoated membranes. The reduced methane conversion from the catalyst-coated membrane is attributed to its lower oxygen flux as shown in Figure 5.13a. In other words, there is a lesser amount of lattice oxygen species available to activate methane in the catalyst-coated membrane reactor, which limits the methane conversion. The slightly lower C_{2+} selectivity from the catalyst-coated membrane (as shown in Figure 5.13b) may be caused by the agglomeration of Cu in some regions of the catalyst layer as can be observed in the EDS elemental maps shown in Figure 5.11b and c. The regions with Cu agglomerates have a higher Cu concentration that the uncoated membrane. Therefore, if the selectivity decreases with increasing Cu content, those regions with high Cu concentration will reduce the overall selectivity of the catalyst-coated membranes compared to the uncoated membranes.

The data in Figure 5.13b contradicts our initial hypothesis of improved OCM performance of the catalyst-coated membrane compared to the uncoated membrane. We believe that this is because the OCM performance of the tubular membrane is limited by bulk-diffusion of lattice

oxygen as opposed to surface kinetics on the methane-side. A better OCM performance could be achieved by decreasing the membrane thickness in order to reduce bulk oxygen diffusion limitations up to a point where the surface kinetics becomes rate limiting. Thereafter, a sufficiently thin porous catalyst layer can be added to the membrane to further improve the performance. To preserve the mechanical strength of the thinner membranes, they can be supported on porous substrates (known as asymmetric membranes).[29,30] Another way to improve the performance of the Cu-BCG tubular membranes will be to eliminate Cu from the system. In the fabrication method used in this study, the addition of Cu to BCG was necessary to reduce the sintering temperature and prevent the membranes from cracking during sintering. More sophisticated fabrication techniques will be required to achieve crack-free BCG tubular membranes without a sintering additive.

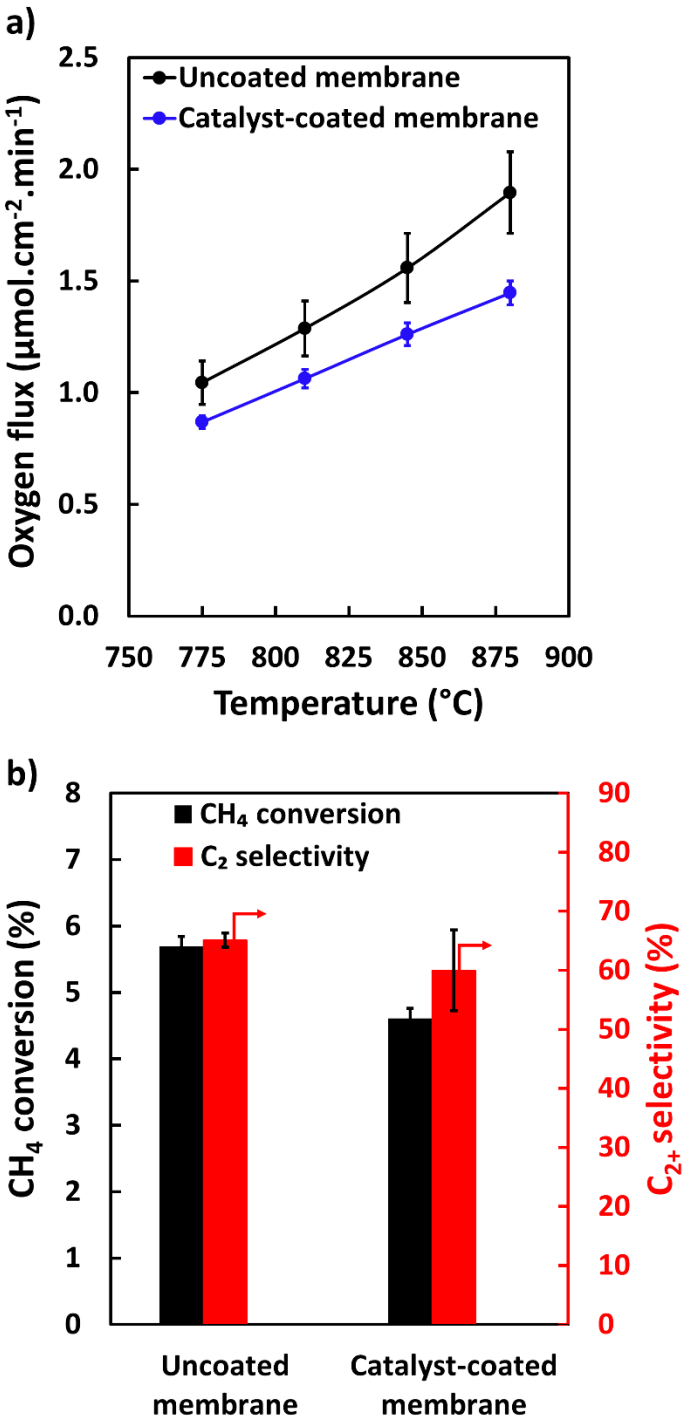

Figure 5.13. (a) Oxygen flux from uncoated and catalyst-coated Cu-BCG tubular membranes as a function of temperature (b) CH_4 conversion and C_{2+} selectivity from uncoated and catalyst-coated Cu-BCG tubular membranes at 845°C.

5.5 Conclusions

Catalytic BCG tubular membranes were fabricated by slip-casting and solid-state reactive sintering (using Cu as a sintering additive) and were studied for OCM. At 845°C, the Cu modified BCG (Cu-BCG) membrane reactor achieved a methane conversion of ~ 6% at a C_{2+} selectivity of ~ 65% using 40 cm^3/min of diluted methane feed (P_{CH4} ~ 0.5 bar, balance He). Significantly higher C_{2+} selectivity was achieved from membrane reactor operation (distributed oxygen feed) compared to co-fed operation of the Cu-BCG membrane, at similar methane conversions. The methane conversion from the Cu-BCG membrane reactor declined over time which was attributed to phase transformations occurring at the surface of the membrane at the operating condition. Unexpectedly, it was found that coating the Cu-BCG tubular membrane with a layer of BCG catalyst reduced the OCM performance. The lower OCM performance of the catalyst-coated membranes was attributed to the transfer of Cu from the membrane to the catalyst layer and additional bulk-diffusion resistance to oxygen transport introduced by the catalyst layer.

5.6 References

(1) National Academies of Sciences, Engineering, and Medicine. *The Changing Landscape of Hydrocarbon Feedstocks for Chemical Production: Implications for Catalysis: Proceedings of a Workshop*; National Academies Press, 2016.

(2) Horn, R.; Schlögl, R. Methane Activation by Heterogeneous Catalysis. *Catal. Lett.* **2015**, *145* (1), 23–39.

(3) Olivos-Suarez, A. I.; Szécsényi, À.; Hensen, E. J.; Ruiz-Martinez, J.; Pidko, E. A.; Gascon, J. Strategies for the Direct Catalytic Valorization of Methane Using Heterogeneous Catalysis: Challenges and Opportunities. *ACS Catal.* **2016**, *6* (5), 2965–2981.

(4) Lunsford, J. H. Catalytic Conversion of Methane to More Useful Chemicals and Fuels: A Challenge for the 21st Century. *Catal. Today* **2000**, *63* (2), 165–174.

(5) McFarland, E. Unconventional Chemistry for Unconventional Natural Gas. *Science* **2012**, *338* (6105), 340–342.

(6) Zavyalova, U.; Holena, M.; Schlögl, R.; Baerns, M. Statistical Analysis of Past Catalytic Data on Oxidative Methane Coupling for New Insights into the Composition of High-Performance Catalysts. *ChemCatChem* **2011**, *3* (12), 1935–1947.

(7) Schwach, P.; Pan, X.; Bao, X. Direct Conversion of Methane to Value-Added Chemicals over Heterogeneous Catalysts: Challenges and Prospects. *Chem. Rev.* **2017**, *117* (13), 8497–8520.

(8) Driscoll, D. J.; Martir, W.; Wang, J. X.; Lunsford, J. H. Formation of Gas-Phase Methyl Radicals over Magnesium Oxide. *J. Am. Chem. Soc.* **1985**, *107* (1), 58–63.

(9) Luo, L.; Tang, X.; Wang, W.; Wang, Y.; Sun, S.; Qi, F.; Huang, W. Methyl Radicals in Oxidative Coupling of Methane Directly Confirmed by Synchrotron VUV Photoionization Mass Spectroscopy. *Sci. Rep.* **2013**, *3*, 1625.

(10) Farrell, B. L.; Igenegbai, V. O.; Linic, S. A Viewpoint on Direct Methane Conversion to Ethane and Ethylene Using Oxidative Coupling on Solid Catalysts. *ACS Catal.* **2016**, *6* (7), 4340–4346.

(11) Luo, L.; You, R.; Liu, Y.; Yang, J.; Zhu, Y.; Wen, W.; Pan, Y.; Qi, F.; Huang, W. Gas-Phase Reaction Network of Li/MgO-Catalyzed Oxidative Coupling of Methane and Oxidative Dehydrogenation of Ethane. *ACS Catal.* **2019**, *9* (3), 2514–2520.

(12) Eng, D.; Stoukides, M. Catalytic and Electrocatalytic Methane Oxidation with Solid Oxide Membranes. *Catal. Rev.* **1991**, *33* (3–4), 375–412.

(13) Tan, X.; Pang, Z.; Gu, Z.; Liu, S. Catalytic Perovskite Hollow Fibre Membrane Reactors for Methane Oxidative Coupling. *J. Membr. Sci.* **2007**, *302* (1), 109–114.

(14) Tan, X.; Li, K. Oxidative Coupling of Methane in a Perovskite Hollow-Fiber Membrane Reactor. *Ind. Eng. Chem. Res.* **2006**, *45* (1), 142–149.

(15) Lu, Y.; Dixon, A. G.; Moser, W. R.; Ma, Y. H.; Balachandran, U. Oxygen-Permeable Dense Membrane Reactor for the Oxidative Coupling of Methane. *J. Membr. Sci.* **2000**, *170* (1), 27–34.

(16) Othman, N. H.; Wu, Z.; Li, K. A Micro-Structured $La_{0.6}Sr_{0.4}Co_{0.2}Fe_{0.8}O_{3-\delta}$ Hollow Fibre Membrane Reactor for Oxidative Coupling of Methane. *J. Membr. Sci.* **2014**, *468*, 31–41.

(17) Othman, N. H.; Wu, Z.; Li, K. An Oxygen Permeable Membrane Microreactor with an in-Situ Deposited $Bi_{1.5}Y_{0.3}Sm_{0.2}O_{3-\delta}$ Catalyst for Oxidative Coupling of Methane. *J. Membr. Sci.* **2015**, *488*, 182–193.

(18) Akin, F. T.; Lin, Y. S. Oxidative Coupling of Methane in Dense Ceramic Membrane Reactor with High Yields. *AIChE J.* **2002**, *48* (10), 2298–2306.

(19) Gorbova, E.; Maragou, V.; Medvedev, D.; Demin, A.; Tsiakaras, P. Influence of Cu on the Properties of Gadolinium-Doped Barium Cerate. *J. Power Sources* **2008**, *181* (2), 292–296.

(20) Gorbova, E.; Maragou, V.; Medvedev, D.; Demin, A.; Tsiakaras, P. Influence of Sintering Additives of Transition Metals on the Properties of Gadolinium-Doped Barium Cerate. *Solid State Ion.* **2008**, *179* (21), 887–890.

(21) Wang, S.; Luo, J.-L.; Sanger, A. R.; Chuang, K. T. Performance of Ethane/Oxygen Fuel Cells Using Yttrium-Doped Barium Cerate as Electrolyte at Intermediate Temperatures. *J. Phys. Chem. C* **2007**, *111* (13), 5069–5074.

(22) Igenegbai, V. O.; Meyer, R. J.; Linic, S. In Search of Membrane-Catalyst Materials for Oxidative Coupling of Methane: Performance and Phase Stability Studies of Gadolinium-Doped Barium Cerate and the Impact of Zr Doping. *Appl. Catal. B Environ.* **2018**, *230*, 29–35.

(23) Igenegbai, V. O.; Almallahi, R.; Meyer, R. J.; Linic, S. Oxidative Coupling of Methane over Hybrid Membrane/Catalyst Active Centers: Chemical Requirements for Prolonged Lifetime. *ACS Energy Lett.* **2019**, *4* (6), 1465–1470.

(24) Švarcová, S.; Wiik, K.; Tolchard, J.; Bouwmeester, H. J. M.; Grande, T. Structural Instability of Cubic Perovskite $Ba_xSr_{1-x}Co_{1-y}Fe_yO_{3-\delta}$. *Solid State Ion.* **2008**, *178* (35), 1787–1791.

(25) Efimov, K.; Xu, Q.; Feldhoff, A. Transmission Electron Microscopy Study of $Ba_{0.5}Sr_{0.5}Co_{0.8}Fe_{0.2}O_{3-\delta}$ Perovskite Decomposition at Intermediate Temperatures. *Chem. Mater.* **2010**, *22* (21), 5866–5875.

(26) Liang, F.; Jiang, H.; Luo, H.; Caro, J.; Feldhoff, A. Phase Stability and Permeation Behavior of a Dead-End $Ba_{0.5}Sr_{0.5}Co_{0.8}Fe_{0.2}O_{3-\delta}$ Tube Membrane in High-Purity Oxygen Production. *Chem. Mater.* **2011**, *23* (21), 4765–4772.

(27) Giannici, F.; Longo, A.; Balerna, A.; Martorana, A. Dopant−Host Oxide Interaction and Proton Mobility in Gd:$BaCeO_3$. *Chem. Mater.* **2009**, *21* (4), 597–603.

(28) Farrell, B. L.; Linic, S. Oxidative Coupling of Methane over Mixed Oxide Catalysts Designed for Solid Oxide Membrane Reactors. *Catal. Sci. Technol.* **2016**, *6*, 4370–4376.

(29) He, B.; Zhang, K.; Ling, Y.; Xu, J.; Zhao, L. A Surface Modified $La_{0.6}Sr_{0.4}Co_{0.2}Fe_{0.8}O_{3-\delta}$ Ultrathin Membrane for Highly Efficient Oxygen Separation. *J. Membr. Sci.* **2014**, *464*, 55–60.

(30) Zydorczak, B.; Wu, Z.; Li, K. Fabrication of Ultrathin $La_{0.6}Sr_{0.4}Co_{0.2}Fe_{0.8}O_{3-\delta}$ Hollow Fibre Membranes for Oxygen Permeation. *Chem. Eng. Sci.* **2009**, *64* (21), 4383–4388.

Chapter 6

Conclusions and Future Directions

6.1 Overall Conclusions

This dissertation research was focused on identifying selective catalysts and membranes for integration in solid oxide membrane reactors, fabricating the integrated systems and evaluating the performance of the systems in the oxidative coupling of methane (OCM) to C_2 hydrocarbons. The overall hypothesis of this research is that solid oxide membrane reactors can improve C_2 selectivity in OCM compared to conventional co-fed reactors. This improvement is attributed to lower gas-phase oxygen concentrations attained through the distributed and controlled delivery of lattice oxygen (O^{2-}) in the membrane reactor. In a background study, we developed reactor models for a membrane reactor and a co-fed reactor. The model results illustrate that membrane reactors should, in principle, give significantly higher C_2 selectivity and yield compared to co-fed reactors.[1]

In subsequent work, we identified, synthesized and studied an O^{2-} conductive gadolinium-doped barium cerate ($BaCe_{0.8}Gd_{0.2}O_{3-\delta}$ or BCG) perovskite material to evaluate its potential applicability both as a catalyst and membrane in solid oxide membrane reactors for OCM. From packed bed reactor (PBR) tests, we found that BCG is catalytically active and achieves high C_{2+} selectivity in OCM particularly at low oxygen concentrations which makes it a promising membrane-catalyst candidate. Unfortunately, under the reaction conditions, BCG segregates into carbonate and oxide phases which will impact its membrane (O^{2-} conductive) properties. This

study highlights a critical problem in the application of O^{2-} conducting membrane reactors in OCM; the contamination of membrane materials with carbonate due to reaction with CO_2. However, we demonstrated that the phase stability of BCG in OCM can be improved by partially doping the perovskite with Zr without significantly affecting the C_2 yields in a PBR.[2]

We proceeded to synthesize button-shaped membrane/catalyst systems and studied their OCM performance under membrane reactor conditions. This preliminary study aims to identify the most promising system to be used in a tubular membrane reactor. In this study, we demonstrated that carbon-induced catalyst deactivation deposition is a major issue in OCM solid oxide membrane reactors due to limited oxygen concentration (i.e., low O_2/CH_4 ratios). This is one of first studies in literature to address the issue of carbon deposition in OCM membrane reactors as previous studies were typically performed using heavily diluted methane feed streams which suppresses this issue. From this work, we identified key chemical requirements of the membrane/catalyst systems that lead to stable performance. Specifically, we showed that a BCG membrane/catalyst system can achieve excellent stability at low O_2/CH_4 ratios which would normally lead to solid carbon-induced catalyst deactivation. Our analysis of the BCG membrane/catalyst system suggests that its high carbon resistance is due to its relatively high oxygen storage/release capacity which suppresses carbon deposition in the system.[3] We also showed that, although Zr doping improves the phase stability of BCG in OCM as observed in our PBR tests, it had a negative effect of significantly reducing the oxygen permeation rate through the membrane.

The final part of this dissertation work was focused on synthesizing and testing tubular BCG membranes in OCM. We successfully developed a creative and cost-effective procedure for synthesizing BCG tubular membranes via a combined slip-casting and solid-state reactive sintering

(SSRS) technique using Cu as a sintering additive. This synthesis procedure is versatile and can be applied in fabricating tubular-shaped barium cerate/zirconate membranes for related applications e.g., solid oxide fuel cells. In OCM tests, we achieved significantly higher C_{2+} selectivity from membrane reactor operation (distributed oxygen feed) compared to co-fed operation of the Cu-modified BCG (Cu-BCG) membranes, at similar methane conversions. This result provides conclusive experimental evidence in support of our overall hypothesis that catalytic membrane reactors can perform better than conventional co-fed reactors in OCM. We also show that the methane conversion from the Cu-BCG membrane reactor declined over time which we attribute to phase transformations occurring at the surface of the membrane at the operating condition. This is one of the first studies on the long-term performance and phase stability of perovskite membrane reactors in OCM. We also found that coating the Cu-BCG tubular membrane with a layer of BCG catalyst reduced the OCM performance. Analysis of the uncoated and coated membrane suggests that a better OCM performance can be achieved by eliminating Cu from the membrane and by decreasing the membrane thickness to minimize bulk diffusion limitations.

6.2 Recommended Future directions

In this study, we have identified BCG as an O^{2-} conducting perovskite material that is catalytically active and shows high resistance to deactivation via solid carbon deposition, and as such is promising for application in OCM membrane reactors. Our overall hypothesis of the improved OCM performance of a membrane reactor over a co-fed reactor was supported by results from the Cu-BCG tubular membrane experiments. In the following sections we discuss future research directions that would improve the OCM performance of the BCG membrane reactors.

6.2.1 Synthesize and test BCG tubular membranes without Cu

As discussed on Chapter 5, the addition of Cu to BCG as a sintering additive negatively affected the C_2 selectivity. To avoid this issue and improve the selectivity, BCG tubular membranes without Cu should be synthesized and tested in OCM. To achieve adequate densification of the BCG membranes at lower temperatures (e.g., at 1450°C) without a sintering additive, BCG powder of very small particle size should be utilized and longer sintering times (> 10 hours) should be employed. The slip-casting method of tube fabrication requires large quantities of BCG powder that would normally be synthesized by solid state reaction (SSR), which yields powders of relatively large particle size compared to solution-based methods. The particle size of the synthesized BCG powder can be decreased by ball milling at high rotation speeds over long periods.[4] Note that the effectiveness of the slip-casting method is affected by the particle size of the BCG powder. For example, if the particle size of the powder in the slip (slurry) is smaller than the pores in the plaster mold, they can penetrate the pores of the mold such that it becomes difficult to separate the casted tube from the mold after drying. Therefore, the composition of the BCG slurry and/or the porosity of the plaster mold would need to be systematically optimized for different particle sizes. Alternative methods for tube fabrication (e.g., by extrusion) should also be explored.[4] Once an effective tube fabrication method is developed for smaller BCG particle size, the sintering time should be systematically tuned to determine if dense BCG tubular membranes can be achieved at lower temperature.

6.2.2 Increase oxygen flux by decreasing the thickness of the BCG membranes

Another approach to improve the performance of BCG membranes in OCM is to increase the oxygen flux through the membranes. The ~500 μm thick BCG membranes used in this dissertation work had relatively low oxygen flux which limits the overall methane conversion.

Consequently, in practical applications, large reactor sizes will be required to achieve high conversions, which will drive up reactor cost. One approach to improve the oxygen flux is to minimize bulk O^{2-} diffusion limitations by reducing the membrane thickness. To ensure that the thinner membranes have enough mechanical strength, they should be supported on porous substrates of the same perovskite material (referred to as asymmetric membranes). Asymmetric ceramic membranes can be fabricated using a number of techniques including dry pressing, slurry dropping, tape casting, dip coating, screen printing and electrophoretic deposition.[5,6] Using such techniques, membranes with different thicknesses can be synthesized and tested at varying oxygen partial pressures gradients to determine the characteristic thickness of the BCG membranes i.e., the thickness at which the kinetics is no longer limited by bulk O^{2-} transport but by surface reaction.[7]

6.2.3 Fabricate and test BCG hollow fiber membranes

BCG hollow fiber membranes should be fabricated and tested for OCM as they can provide higher surface area to volume ratio compared to conventional tubular membranes. Hollow fiber membranes have very narrow diameter (~ 0.5 – 3 mm ID),[6,8] which would allow the attainment of high packing densities when arranged in bundles, thus enabling higher oxygen supply per unit volume. Such a design is particularly advantageous for smaller-scale, modular applications (e.g., for the distributed upgrading of natural gas) where the overall size of the membrane reactor for a given C_2 production rate needs to be minimized. Asymmetric BCG hollow fiber membranes should also be fabricated to allow the simultaneous attainment of high surface area to volume ratio and improved oxygen flux due to lower membrane thickness. The BCG hollow fiber membranes can be synthesized by adapting a combined phase-inversion and sintering technique which has been reported in the literature for synthesizing other ceramic hollow fiber membranes.[9]

6.2.4 Develop models for membrane reactor optimization

In an optimum OCM membrane reactor design, the oxygen transport rates across the membrane should be comparable to the surface reaction rates. The oxygen flux and surface reaction rates can be matched by tuning certain parameters e.g., membrane thickness, temperature, flowrate, methane feed concentration and oxygen partial pressure difference. A mathematical model that captures transport and kinetic parameters should be developed and applied in system optimization. This model should sufficiently describe the rates of O^{2-} transport through the membranes as a function of the membrane thickness and reaction conditions. The model development would involve conducting OCM kinetic studies on the integrated catalyst and validating the kinetic model. Developing a comprehensive mathematical model that incorporates transport and kinetics should enable the identification of geometries and reaction conditions that maximize the membrane reactor performance.

6.3 References

(1) Farrell, B. L.; Igenegbai, V. O.; Linic, S. A Viewpoint on Direct Methane Conversion to Ethane and Ethylene Using Oxidative Coupling on Solid Catalysts. *ACS Catal.* **2016**, *6* (7), 4340–4346.

(2) Igenegbai, V. O.; Meyer, R. J.; Linic, S. In Search of Membrane-Catalyst Materials for Oxidative Coupling of Methane: Performance and Phase Stability Studies of Gadolinium-Doped Barium Cerate and the Impact of Zr Doping. *Appl. Catal. B Environ.* **2018**, *230*, 29–35.

(3) Igenegbai, V. O.; Almallahi, R.; Meyer, R. J.; Linic, S. Oxidative Coupling of Methane over Hybrid Membrane/Catalyst Active Centers: Chemical Requirements for Prolonged Lifetime. *ACS Energy Lett.* **2019**, *4* (6), 1465–1470.

(4) Athayde, D. D.; Souza, D. F.; Silva, A. M. A.; Vasconcelos, D.; Nunes, E. H. M.; Diniz da Costa, J. C.; Vasconcelos, W. L. Review of Perovskite Ceramic Synthesis and Membrane Preparation Methods. *Ceram. Int.* **2016**, *42* (6), 6555–6571.

(5) Ishii, K.; Matsunaga, C.; Kobayashi, K.; Stevenson, A. J.; Tardivat, C.; Uchikoshi, T. Fabrication of BSCF-Based Mixed Ionic-Electronic Conducting Membrane by Electrophoretic Deposition for Oxygen Separation Application. *J. Eur. Ceram. Soc.* **2019**, *39* (16), 5292–5297.

(6) Lemes-Rachadel, P.; Garcia, G. S.; Machado, R. A. F.; Hotza, D.; Costa, J. C. D. da. Current Developments of Mixed Conducting Membranes on Porous Substrates. *Mater. Res.* **2014**, *17* (1), 242–249.

(7) Chen, C. H.; Bouwmeester, H. J. M.; van Doorn, R. H. E.; Kruidhof, H.; Burggraaf, A. J. Oxygen Permeation of $La_{0.3}Sr_{0.7}CoO_{3-\delta}$. *Solid State Ion.* **1997**, *98* (1), 7–13.

(8) Schiestel, T.; Kilgus, M.; Peter, S.; Caspary, K. J.; Wang, H.; Caro, J. Hollow Fibre Perovskite Membranes for Oxygen Separation. *J. Membr. Sci.* **2005**, *258* (1), 1–4.

(9) Tan, X.; Liu, Y.; Li, K. Preparation of LSCF Ceramic Hollow-Fiber Membranes for Oxygen Production by a Phase-Inversion/Sintering Technique. *Ind. Eng. Chem. Res.* **2005**, *44* (1), 61–66.